NORTHWESTERN UNIVERSITY

X-ray Investigations of the Initial Growth of Si/Ge/Si Heterostructures Grown by Surfactant Mediated Epitaxy

A DISSERTATION
SUBMITTED TO THE GRADUATE SCHOOL
IN PARTIAL FULFILLMENT OF THE REQUIREMENTS

for the degree of
DOCTOR OF PHILOSOPHY

Field of Materials Science and Engineering

By

Bradley Paul Tinkham

EVANSTON, ILLINOIS
December 2002

ABSTRACT

X-ray Investigations of the Initial Growth of Si/Ge/Si Heterostructures Grown by Surfactant Mediated Epitaxy

Bradley Paul Tinkham

The understanding of the initial stages of epitaxial growth of Ge on Si surfaces is important both fundamentally and technologically. Strained Si and Ge layers have superior electronic properties to relaxed layers in many ways. Strained layer growth of Ge on Si occurs for 3-4 ML upon which the film begins to relax. The addition of a surfactant species (with a lower surface free energy), during growth can extend this thickness as well as improve interface quality between heterolayers.

Using Te as a surfactant we have grown, using MBE, a series of Si/Ge/Si(001) samples between 1-10 ML Ge coverage and determined the extend to which samples grown with Te are superior to those grown without Te. The interface roughness for samples grown with Te are between 1-3 angstroms. This is in contrast to samples grown without surfactant where above the critical thickness these films are 3D and give roughness values greater than nine angstroms as measured by x-ray reflectivity. For samples with Te, we find that it is possible to grow coherent, strained layers up to at least nine ML. As determined by XSW, Ge coherent fractions and coherent positions for samples grown with Te are consistent with predictions from elasticity theory.

The success of Te as a surfactant is strongly related to its structure on both Si(001) and Ge(001). This was a motivation for us to perform surface x-ray scattering experiments on the Te/Ge(001) surface. We have proposed a model for the Te coverage of ~0.8 ML and determined that Te adsorbs on bridge sites on Ge(001). Missing Te rows are present in this model in order to accommodate the larger Te atom on the Ge surface.

Finally we have investigated the MBE grown heterostructure of 1-2 bilayers of Ge buried in Si(111). We find that the Ge bilayer is expanded by an amount greater than suggested by elasticity theory. In addition we propose that Bi as a surfactant is successful in preventing intermixing between Si and Ge, however, it is not clear that Bi improves the overall quality of Ge epitaxial layers on Si(111).

ACKNOWLEDGEMENTS

I'd like to thank the many people who have supported me and contributed to my training during my graduate studies. First of all I thank my advisor Dr. Michael Bedzyk for his mentoring and for introducing me to the field of surface science and x-ray physics. His motivation and support was crucial to my training and guidance for my scientific career. I benefited greatly from the experience of other senior members of our group, including Osami Sakata, Paul Lyman, Chang-Yong Kim, Likwan Cheng, and Don Walko. Due to their extensive skill and knowledge, they provided me with valuable advice throughout my graduate school career. I would also like to acknowledge other graduate students that assisted my work including, William Rodrigues, Tien-Lin Lee, Duane Goodner, David Marasco, Anthony Escuadro, Zhan Zhang and Joe Libera. They participated and contributed to many of the experiments in this thesis. I also like to thank Dr. David Seidman, Dr. Paul Lyman, and Dr. Laurence Marks for participating in my thesis committee. I thank Joanna Fico for proofreading my thesis and finally my parents for their support throughout my college career. I dedicate my thesis to them.

This work was supported by the MRSEC NSF Contract No. DMR-0076097 and by NSF Contract No. DMR-9973436.

To my Parents

Robert and Beverly Tinkham

TABLE OF CONTENTS

LIST of TABLES

LIST OF FIGURES

Chapter 1 Introduction

The understanding of the initial stages of epitaxial thin film growth has become extremely important as engineering is now being performed on the atomic scale. Specifically, the initial growth of Ge on Si is important from a technological perspective as it relates to the development of commercial field effect transistors for high frequency applications. The fundamental knowledge obtained from the study of Ge/Si acts as a model for interpreting other more complicated heteroepitaxial systems. This thesis uses both conventional and synchrotron generated radiation to probe the evolution of strain and disorder in MBE grown Ge/Si heterostructures. Additionally, this thesis evaluates the effectiveness of Te as a surfactant in Ge/Si heteroepitaxy as well as investigates the surface structure of Te/Ge(001).

X-rays offer many advantages over other structural characterization techniques. For instance, in the limit of weak scattering, one can utilize the Born approximation to simplify the analysis significantly. X-ray diffraction is non-destructive and typically samples a large fraction of the sample area and therefore measures the average structure of the system and can easily be used to analyze buried structures. This is in contrast to other techniques (i.e. TEM, STM) where the experiment is sensitive to only very local structure or where sample preparation can introduce artifacts that could complicate the analysis.

The outline of this thesis is as follows: Chapter 2 provides relevant background information on Ge/Si heteroepitaxy as well as surfactant mediated epitaxy (SME). Applications for SiGe devices are discussed as well as basic principles for strained layer growth and transitions from two-dimensional to three-dimensional growth. Chapter 3 discusses the basic theory of both kinematical and dynamical diffraction theory for x-rays. This chapter provides the requisite background information to generate equations for the analysis of our data. Chapter 4 investigates the surface structure of ~0.8 ML of Te adsorbed on Ge(001) in ultra-high vacuum. This surface is important as it, along with Te/Si(001), provides the template for our SME growth of Ge/Si(001). Chapter 5 presents our study of Te as a surfactant in Si/Ge/Si(001) heteroepitaxy. In this chapter we evaluate the effectiveness of Te in promoting 2D growth of Si/Ge/Si(001) as well as the ability to create abrupt interfaces between layers. A number of x-ray techniques are used including specular reflectivity, crystal truncation rods, grazing incidence diffraction, and x-ray standing waves (XSW). Chapter 6 presents our study of Si/Ge/Si(111) heterostructures. XSW and EXAFS are used to determine the strain in the buried Ge bilayers and we compare our results to continuum elasticity theory. Chapter 7 provides a comprehensive conclusion of our investigations.

Chapter 2 Silicon-Germanium Heteroepitaxy

2.1 Introduction

In 1947, the first transfer resistor was demonstrated at Bell Technical Laboratories. [1] In this experiment, Germanium was made into a three terminal device and thus became the first semiconductor material to show promise in VLSI applications. In the early 1950's, interest in Silicon surpassed that of Germanium as Silicon displayed advantages such as material availability and superior native oxide interface. Subsequently, research on Ge became scarce until 1983 when Bean and coworkers [2, 3] conducted systematic studies on the material issues and outlined the parameter space in which high quality pseudomorphic SiGe thin films could be grown on Si substrates by ultra high vacuum (UHV) molecular beam epitaxy (MBE). Such improvement in material quality brought about a rapid expansion of the field. Electronic transport studies were followed [4] by an array of demonstrative devices ranging from field effect transistors (FETs)[5, 6] to photodetectors. [7] In the meantime, a systematic understanding of the energy band structure [8], fundamental electronic properties, [9] and material issues [10, 11] of SiGe/Si and Ge/Si has been developed.

2.2 Strained-layer device application

The strain present in a SiGe/Si heterostructure modifies the energy band structure resulting in changes in the band gap value, the curvature at the conduction and valence band minima, and the degeneracy. Changes in the curvature affect the carrier effective mass and changes in the degeneracy affect both carrier effective masses, mobility, and effective channel velocity. The change in the energy band gap is used in the heterojunction bipolar transistors to improve the performance and the change in carrier effective mass, channel mobilites and effective channel velocities are the reasons for using strained Si, Ge or SiGe for field effect transistor applications.

The strain in a Ge epitaxial film is uniaxial in the out-of-plane direction and biaxial in the 2D plane. The lattice in the in-plane direction is compressed by an amount equal to the lattice mismatch between the epitaxial film and substrate. Associated with the strain is the tetragonal distortion of the lattice in the epitaxial film and to a lesser extent, the substrate. The amount of distortion in each is inversely proportional to its thickness. Therefore, the epitaxial layer is the one that is distorted in reality, while the substrate exhibits negligible strain. The most noticeable consequence is that many electronic properties become anisotropic. From an electronic transport point of view, strain changes the energy band minima for both the valence as well as the conduction band. The amount of relative change depends on whether it is the valence or the conduction band, whether the 2D channel is in Si, Ge or SiGe, and whether the channel is under compressive or tensile strain. Electrons are confined in a strained Si layer and holes are confined in a strained Ge layer. Figure 2.1 demonstrates the strained induced splitting of the valence band degeneracy at the Γ-point in a Ge channel under compressive strain. The separation energy can be calculated to be around 80 meV under a 1% compressive strain and up to 300 meV for a 4% strain. The curvature of the lowest lying valence band deviates significantly from being parabolic, resulting in a 2D hole effective mass in Ge that approaches the value of the light hole mass of 0.044 m_o. This value is lighter than the electron mass in GaAs. It should be noted that for tensile strained Si layers grown on Ge, enhancement of charge carrier mobility occurs. However, in the case of strained Si, electron mobilities in the conduction band are increased. Figure 2.2 shows a typical structure of a field effect transistor (FET) that implements a strained Ge p-channel. [12-15] The advantage of such a device is its simplicity. The only difference from a conventional Si MOSFET is the SiGe channel. The channel can be made thermodynamically stable using a proper combination of layer thickness and Ge concentration. The strained channel is separated from the SiO_2/Si interface by a Si cap layer and has a lower effective mass. Both of these factors contribute to enhanced mobility.

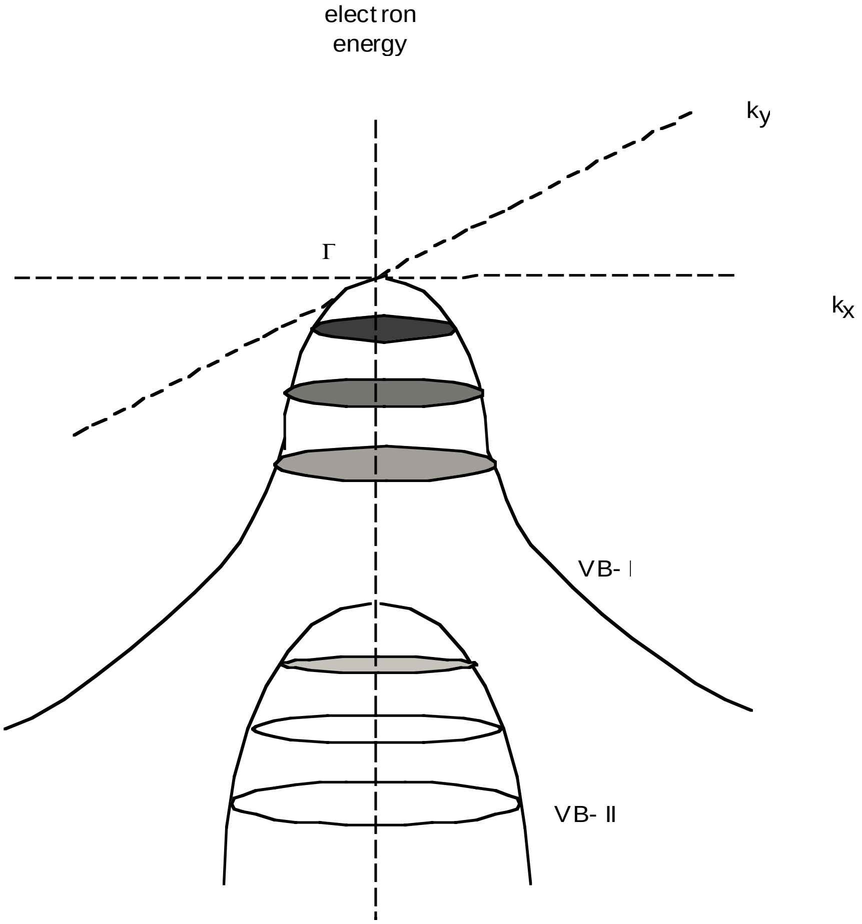

Figure. 2.1. Strain induced splitting of the valence band degeneracy near the Γ point. The shaded discs schematically represent hole population at room temperature.

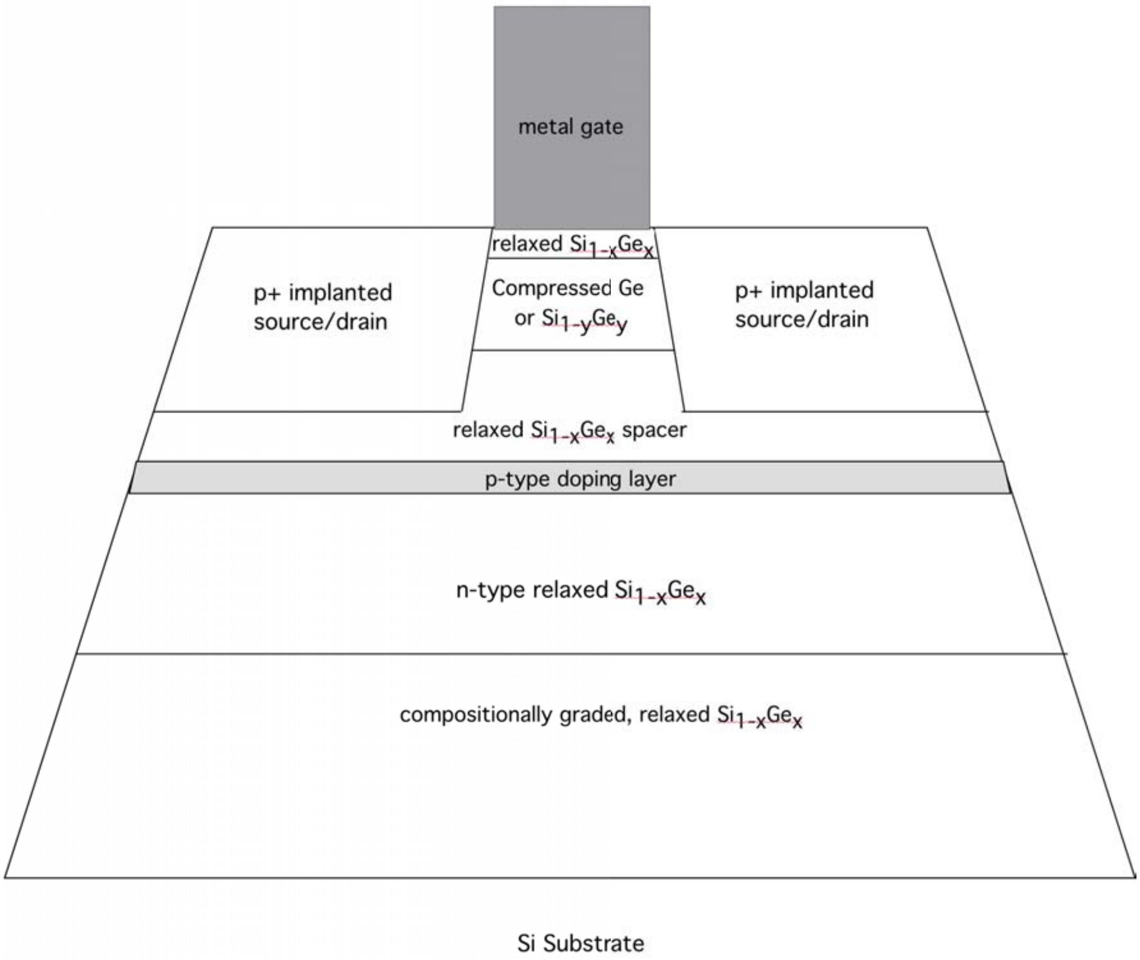

Figure. 2.2 Schematic drawing of a SiGe–channel MOSFET. It is a buried channel FET where the only layer that is under strain is the SiGe channel.

Unlike GaAs and other III-V compound materials, Si does not have other cubic semiconductor materials lattice matched to it. This is the major reason Si trails compound semiconductors in terms of various heterojunction devices. Ge is the only elemental semiconductor with a lattice constant close to that of Si with a lattice mismatch of about 4% (a_{Si}=5.43095 Å,a_{Ge}=5.64613 Å). While 4% does not seem to be a large mismatch, it is exceedingly large from the epitaxial growth point of view. This point can be appreciated by considering the following two materials issues: strain relaxation via dislocation and epitaxial growth in 3D growth mode.

2.3 Strain and relaxation and growth modes in heteroepitaxy

The word epitaxy comes from Greek terminology and means 'arrangement'. In epitaxial growth, atomic layers are arranged onto a substrate. Both the substrate and epitaxial layer are crystalline and a fixed relation exists between the crystal structure of the substrate and the epitaxial layer. If the substrate and epitaxial layer have different crystal structures, several different epitaxial relations often exist. For the case of Si and Ge, which will be considered in this thesis, Si and Ge both crystallize in the diamond structure and the epitaxial relation is just the continuation of the diamond structure of the substrate in the epitaxial film. In MBE of Ge/Si, Si or Ge are heated in evaporators until they reach a vapor pressure of ~ 10^{-6}-10^{-5} Torr whereby growth rates are suitable for layer by layer growth. The beam of Si or Ge atoms hits the surface and the atoms diffuse over the surface and finally bond at surface lattice sites. For the case of semiconductor epitaxy, the substrate has to be heated to a temperature of several hundred degrees Celsius. At lower temperatures, the mobility of the atoms is so low that an amorphous layer is formed.

Heteroepitaxial growth is the growth of material A on material B, where B is different from A. Parameters such as the surface energy and the elastic strain due to the different lattice constants are important. If only the different surface energies of the materials A and B are considered, two different cases can occur at the thermodynamic limit where the interface energy between A and B are neglected.[16] If the surface free energy of the substrate (B) is larger than the surface free energy of the growing film (A), the film wets the substrate and layer-by-layer growth occurs (Van der Merwe growth)[17]. If the surface energy of the substrate (B) is lower than that of the growing film, no wetting occurs and the film material arranges in such a way that only a small part of the substrate is covered. This results in the growth of three-dimensional islands (Volmer Weber growth).[18]

Besides the surface free energy, the growth mode also depends on the elastic strain in the film which, in turn, depends on the lattice mismatch $\varepsilon = (a_A - a_B)/a_B$ between the substrate (lattice constant a_B and the film (lattice constant a_A)). For the case of Ge growth on Si, the lattice constant of Ge is 4% larger than that of Si. Initially, for the first atomic layers, the lattice constant of the film adapts to the lattice constant of the infinitely thick substrate, resulting in an elastic strain in the film. The corresponding strain energy rises linearly with the film thickness. Above a critical thickness, the growth mode of initial layer-by-layer growth is followed by three-dimensional island growth in strained layer epitaxy is called Stranski-Krastanov growth. [19]

2.3.1 2D to 3D growth mode transition in Ge/Si heteroepitaxy

In the following section, the driving forces responsible for the transition from two-dimensional to three-dimensional growth in strained layer epitaxy will be discussed in more detail. A model will be considered for the energy difference between a flat two-dimensional film morphology and a film morphology consisting of three-dimensional islands. The two-dimensional film is arranged pseudomorphically on the substrate, i.e. the lateral lattice positions of the film are the same as in the substrate. The larger lattice constant in the film leads to a build up of elastic strain energy. The formation of three-dimensional islands allows a partial relaxation of the lattice planes in the three-dimensional islands towards the bulk lattice constant of the film material. This different film morphology reduces the elastic energy in the film compared to the case of flat two-dimensional growth. The three-dimensional island formation costs additional surface energy due to the larger surface area of the three dimensional morphology. This tradeoff between the additional surface energy and the gain of energy due to elastic relaxation is the driving force for the transition from the two-dimensional to three-dimensional film morphology.

In a simple model where the islands are just cubes with length x, the additional surface energy for the film in island morphology is proportional to the square of the island size (x^2). The gained elastic relaxation energy compared to that of a flat film is in the simple assumption proportional to the volume of the island (x^3). For the same total volume in the film, the energy difference between the three-dimensional island morphology and the flat morphology is:

$$\Delta E = E_{surf} - E_{relax} = C\gamma x^2 - C'\varepsilon^2 x^3 \tag{2.1}$$

γ is the surface energy, and C and C’ are constants. The contributions of E_{surf} and E_{relax} and the total energy difference between the three-dimensional island morphology and a flat film are shown in Figure 2.3 as a function of the island size x. For small sizes of the three-dimensional islands, the three-dimensional island morphology is unfavorable until the point where the absolute value of the gained elastic relaxation energy ($\sim x^3$) becomes larger than the cost of surface energy ($\sim x^2$). As shown in Figure 2.3, for islands larger than a critical island size x_{crit}, the formation of three-dimensional islands is energetically preferred over the two-dimensional film morphology. While this simple model shows the basic driving forces for the two-dimensional to three-dimensional transition, it contains several simplifications, which will be addressed later in this chapter. As an example, in this simple model, the island morphology is assumed as cubes, which does not correspond to the experimentally observed island shapes. Further, the simple model contains only energetic considerations of two final states. Kinetic effects, such as material transport necessary during the two-dimensional/three-dimensional transition, are not considered.

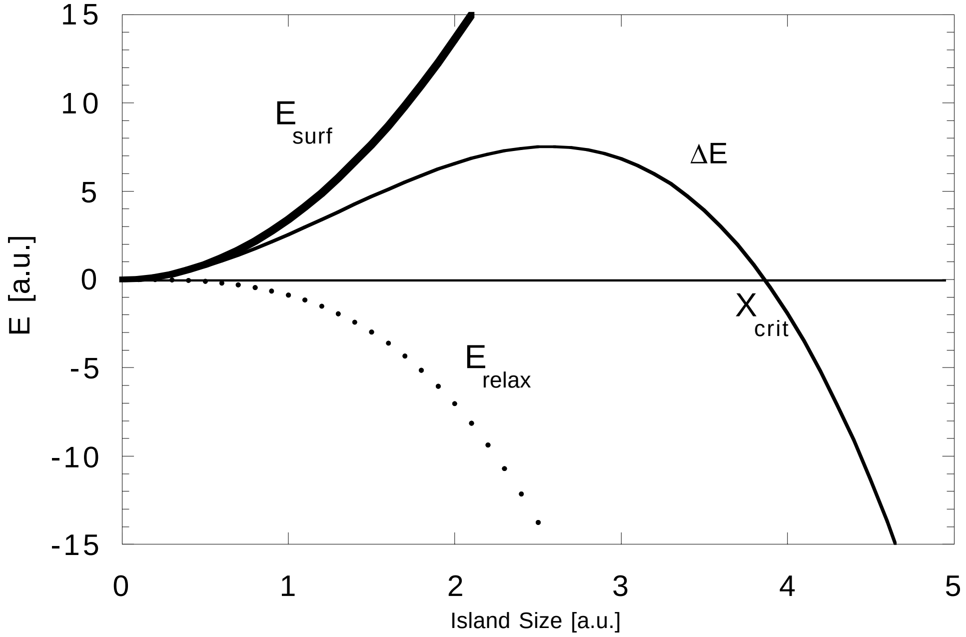

Figure 2.3 Energy difference between a film of flat 2D morphology and a film morphology consisting of 3D islands. Plotted are the surface energy contribution, relaxation energy contribution, and the total energy difference.

Apart from the formation of three-dimensional islands, there exist additional methods of relieving strain in two-dimensional films; one of these is the introduction of misfit dislocations. The strain relief by formation of three-dimensional islands and by the introduction of misfit dislocations are two competing mechanisms for strain relaxation in strained layers. It has been shown that the barrier for three-dimensional island formation scales with the misfit ε as ε^{-4}, while the barrier for nucleation of dislocations scales with the misfit as ε^{-1}. [20] For low misfit, the introduction of misfit dislocations dominates, while for larger misfit, the formation of three-dimensional islands is the dominant process.

2.3.2 Ge/Si(111)

Initial growth of Ge on Si(111) begins with the formation of a two-dimensional wetting layer. The wetting layer, which is 2 atomic bilayers thick, grows in a layer-by layer growth mode. [21-23] A (5x5) reconstruction, which is very similar to the (7x7) reconstruction on the Si(111) substrate, is found on the surface. [21, 24] After completion of the wetting layer, nucleation of one type of three-dimensional islands is observed. These islands consist of {113} facets and a flat top {(111)} facet. For larger islands, a transition from coherent to dislocated islands is observed, while the shape of the islands stays the same.[23, 25] Figure 2.4 shows a series of images [26] of Ge epitaxy on Si(111) up to the critical thickness of about two layers of germanium (1 BL = 1 bilayer = 1.56×10^{15} atoms/cm^2). Ge grows in the island-nucleation growth mode, where Ge nucleates in two-dimensional islands of triangular form (1-3 BL) high, which coalesce with increasing coverage (Figure 2.4 (a)-(c)). Larger islands in the second layer have an irregular form and coalesce to eventually form a flat, two-dimensional Stranski-Krastanov, before three-dimensional islanding occurs. From these figures it can be seen that at 1 BL total coverage, the partial coverage in the first layer is ~80%,

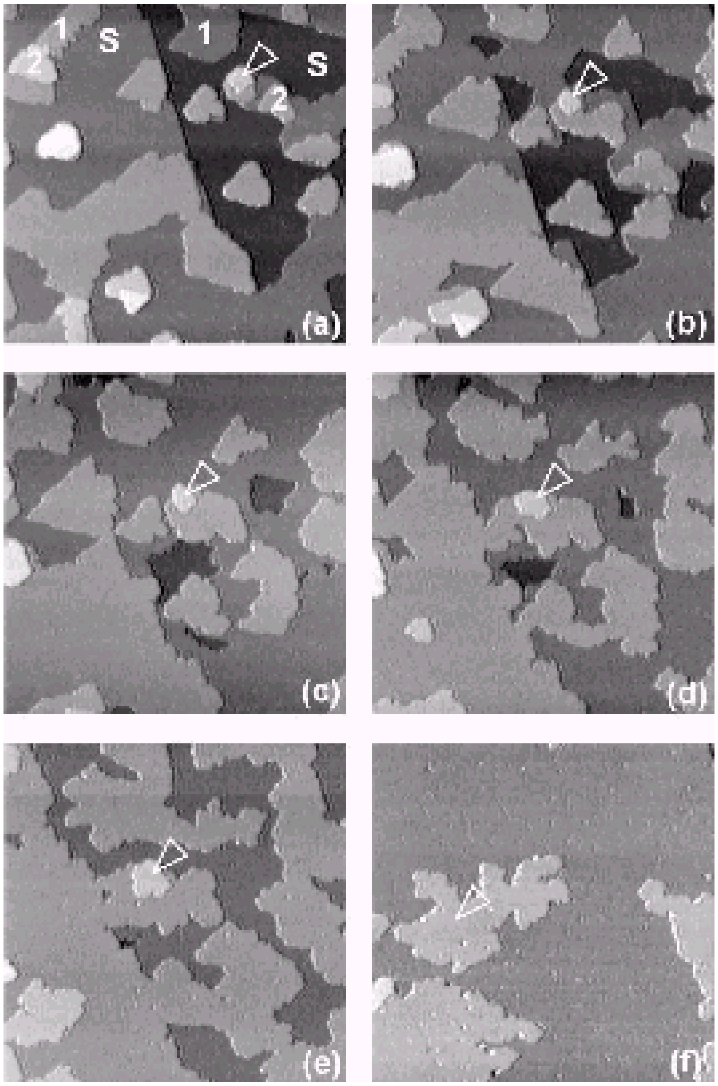

Figure 2.4 (a-f) STM images from *Voigtlaender et al.* [26] (290nm x 290 nm) of the growth of Ge on Si(111) at 773 K. Images were recorded at 0.6, 0.9, 1.2, 1.3, 1.5, and 2.1 BL Ge coverage, respectively. In (a), the substrate (s), and the first and second Ge layers, are indicated. The same 3 BL island (indicated by white arrow) is seen in all six images.

in the second layer ~20% and even a few percent of Ge have nucleated in the third layer. This initial multilayer growth changes with deposition to a mode very close to layer-by-layer growth. At a coverage of 2 BL the second BL is almost closed with only about 3% of the third layer filled. The two-dimensional growth continues slightly beyond the coverage of 2 BL.[27]

2.3.3 Ge/Si(001)

In the case of Ge epitaxy on Si(001), a (2xN) reconstruction is observed on the two-dimensional strained layer (wetting layer). [28-30] This reconstruction consists of a periodic array of missing dimers of the (2x1) reconstruction. Every Nth dimer of the (2x1) reconstruction is missing. Figure 2.5 displays the evolution of structure observed for a Ge terminated Si(001) surface at a 375 ^{0}C as a function of Ge coverage. The growth rate in this case is 0.05 ML/min (1 ML = $6.78\mathrm{x}10^{14}$ atoms/cm^2). The growth mode during the formation of the Ge wetting layer is initially step-flow growth, i.e. steps are observed to move and no formation of two-dimensional islands is observed. Starting at a coverage of about 0.3 ML, missing dimers begin to align in the form of rows, forming trenches. For coverages higher than 0.7 ML the trenches form a regular array with a regular spacing between the trenches. With increasing coverage, the distance between the trenches is observed to decrease. As can be seen in Figure 2.5, the formation of the (2xN) reconstruction is observed with the same spacing at all locations on the surface, even for submonolayer Ge coverage. This is not what would

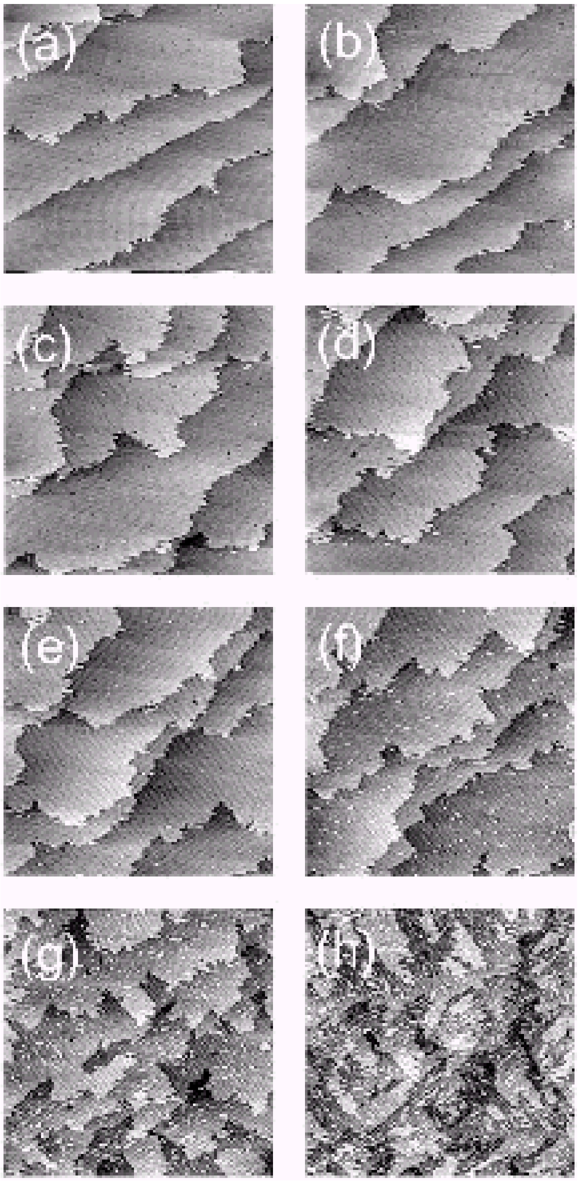

Figure 2.5 STM images from *Voigtlaender et al*. [31] Images showing the wetting layer growth of Ge on Si(001) and the evolution of the (2xN) surface reconstruction. Image area: 160 x 160 nm, and T = 575 K. Ge coverages: 0, 0.33, 0.62, 0.92, 1.26, 1.58, 1.82, and 2.11 ML in (a)-(h) respectively.

be expected for step-flow growth of Ge. In this case, one would expect to observe domains of (2 x N) reconstruction near the pre-existing step edges (where the Ge would be expected to be incorporated) and no (2 x N) structure in the areas which are not covered by Ge. Instead, the deposited Ge atoms diffuse over the growth surface and exchange places with Si atoms on terraces. [32, 33] Due to this displacive incorporation of Ge, the strain is shared between the Si and Ge at submonolayer coverages. The strain energy, which is quadratic in strain, is substantially lower in the case of a mixed Si/Ge layer compared to separate coexisting domains of Si and Ge . The (2 x N) periodicity N rapidly decreases from 17 at 0.8 ML to N = 10 at 1.2 ML Ge coverage. For higher coverages, the decrease is slower approaching N = 8-9 at 2 ML coverage.

The transition from layer-by-layer growth to multilayer growth of Ge on Si(001) is more complicated than for Ge on Si(111), since several different types of three-dimensional islands are observed and there are various relaxation mechanisms in the wetting layer. The start of nucleation of three-dimensional islands is accompanied by the appearance of streaks in the RHEED patterns [34], which are assigned to electrons scattering at {105} planes. These islands are called “hut” clusters (10-20 nm in size) [35] due to their shape. As the average film thickness increases, Reflection High Energy Electron Diffraction (RHEED) patterns start showing {113} and {102} planes along with {105}. This stage is referred to as the formation of multi-faceted “dome” clusters (50-100 nm is size). On passing from “hut” clusters, the relaxation level of mechanical stress increases. It has been suggested that the material is elastically relaxed by 20% in "hut" clusters and by more than 50% in dome islands because of their higher aspect ratio. [36] In the latter case, the islands maintain coherency with the substrate. [37] The final stage of morphological and structural evolution of Ge islands on Si(001) and Si(111) is the formation and rapid growth of plastically deformed, three-dimensional islands with misfit dislocations at the island-substrate interface, i.e. "super-dome" islands. [38]

2.4 Surfactant Mediated Epitaxy

Recently, the use of additional surface species (surfactants) which modify the epitaxial growth has attracted a lot of interest. [39, 40] In surfactant mediated epitaxy a monolayer of surfactant material floats at the growth front and influences the epitaxial growth. The use of a suitable surfactant can suppress the three-dimensional islanding of Ge on Si (Stranski-Krastanov growth) as well as prevent intermixing between Si/Ge epitaxial layers. This property allows the potential for the creation of improved quality structures for device application such as strained Si/Ge superlattices. [41, 42] Additionally, flat relaxed Ge layers on Si substrates which can be grown with surfactant-mediated epitaxy could be used to improve the quality of Ge buffer layers, which are often used in GaAs epitaxy on Si. While surfactants are already used to improve the quality of Ge layers on Si, the question why certain surfactants suppress

3D islanding in Ge/Si heteroepitaxy while others do not is not yet answered. There are a number of prerequisites for the surfactant to be effective.

1. The surfactant must always cover the top layer on which newly deposited atoms arrive. This is necessary for passivation of the surface and implies efficient segregation of the surfactant atoms.
2. Due to passivation of the surface by the surfactant, the newly deposited atoms weakly interact with the top-most adsorbate layer and can therefore move freely on the surface, i.e. the activation energy for surface diffusion is small.
3. There must exist pathways by which the newly deposited atoms exchange positions with surfactant atoms and thereby become embedded below the adsorbates.
4. The atoms that have been embedded below the adsorbate layer diffuse very slowly because bulk diffusion has a activation energy much larger than surface.

Elements from groups III[43], IV[44], V [37, 39, 45-47], and VI [48, 49] have been studied as surfactants for both homoepitaxial and heteroepitaxial applications. Although the heteroepitaxy of materials is the main application for surfactants, surfactant mediated homoepitaxy is a useful comparison as it can elucidate some of the properties of surfactants that make them effective or not effective. In homoepitaxy there is a driving force for the formation of 3D clusters, however, there is no strain energy to contend with, which leads to slightly different prerequisites for a surfactant to be effective. For instance, Indium tends to enhance the diffusivity of Si, while Sb and As are shown to drastically reduce the surface diffusivity. [50] This characteristic can be carried over to the application of Ge/Si where the reduction of the Ge diffusion length in surfactant mediated epitaxy is shown to be a mechanism for the suppression of three-dimensional islanding in Ge/Si heteroepitaxy. Therefore, it is expected for As and Sb to be effective surfactants. Table 2.1 summarizes the results of eight elements and their properties as surfactants in homoepitaxy and heteroepitaxy.

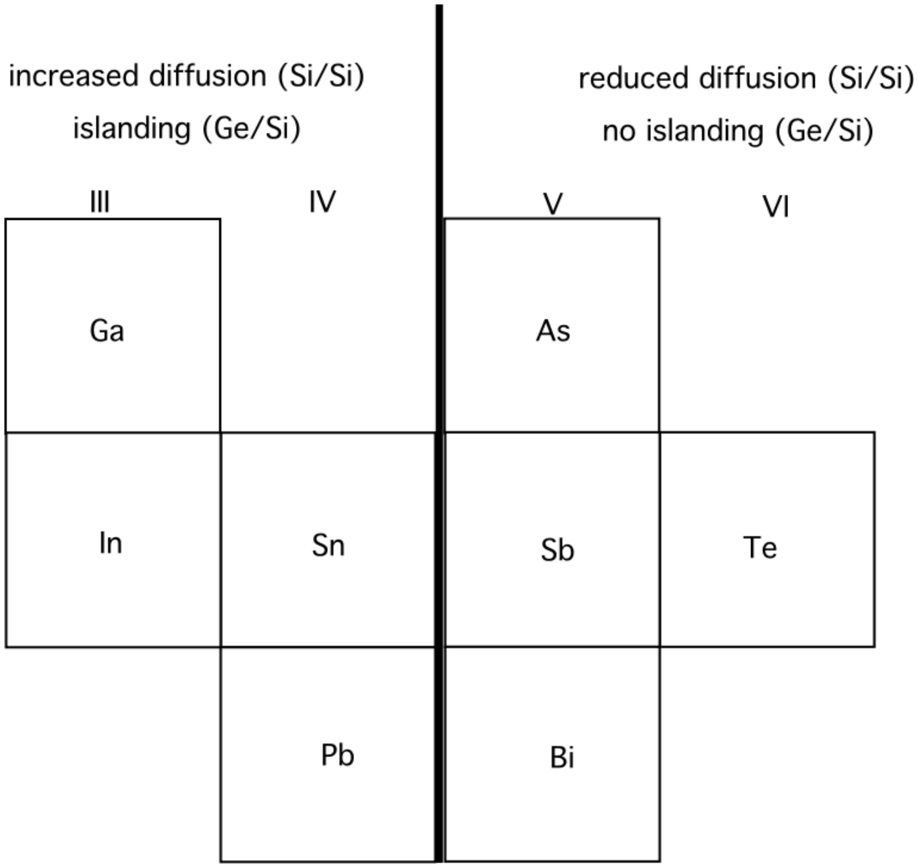

increased diffusion (Si/Si) islanding (Ge/Si)		reduced diffusion (Si/Si) no islanding (Ge/Si)	
III	IV	V	VI
Ga		As	
In	Sn	Sb	Te
	Pb	Bi	

Table 2.1 Section of the periodic table indicating surfactant properties for the selected elements.

Another relevant property of surfactants is their surface passivation behavior. The fact that surfactants are able to passivate surfaces sets up a driving force for oncoming adatoms to site exchange with the surfactant and enable adatoms to incorporate into the underlying epitaxial layer. It is apparent that the effectiveness of a surfactant is strongly related to is structure on Si and Ge. The probability for site exchange is related to the rate at which the event occurs:

$$\Gamma = \nu e^{-E_{ac}/k_B T_g} \tag{2.2}$$

where T_g is the growth temperature and ν and E_{ac} are the site exchange attempt frequency and activation energy, respectively. Ko *et al.* [51] performed first principles calculations comparing the activation energy for surfactants (Ga, As, and Sb) to incorporate Ge into the epitaxial layer for Ge/Si(111). It was concluded that As and Sb have much lower exchange barriers than Ga, and that As has a larger recovery-exchange probability. These properties suggest that Sb is the most suitable choice for a surfactant in this system. Obviously other surfactants have been used in Ge/Si epitaxy, but, they have not received attention from a theoretical perspective and can only be compared from the point of view of experimental performance.

2.4.1 Strain relief mechanisms for relaxation for SME Ge/Si

Surfactants are able to extend the limit of x_{crit} by kinetically inhibiting the clustering of adatoms, however, the films that are created are in a metastable state. At some point the strain energy accumulates to a level where defects are created in order to relieve strain. For SME Ge/Si(001), defects are introduced into the film at different thicknesses for this purpose. TEM studies on As mediated Ge/Si(001) SME films [52] show that films grown up to eight monolayers are completely strained and pseudomorphic, i.e. no defects and/or islands are formed (Figure 2.6). At a thickness of twelve monolayers, strain induced defects from throughout the film. Initially, the defect consist of several {111} planes tilted perpendicular to the direction of maximum strain which form a V-shaped defect which can be seen in Figure 2.7. This markes the onset of strain relaxation as far as cross-sectional TEM can detect, however, it is not clear at what point exactly these defects are initiated (between 8-12 ML). At approximately 50 ML of Ge, the V-shaped defects begin to act as nucleation sites for edge dislocations that climb down into the Si substrate and then glide through the rest of the sample. The strain relief is shared by the original defects in the Ge layer and dislocations located in the silicon substrate. After several hundred monolayers of Ge, extended defects such as stacking faults are generated from the existing defects. The creation of these defects minimizes the interfacial energy between the existing defects and the rest of the film.

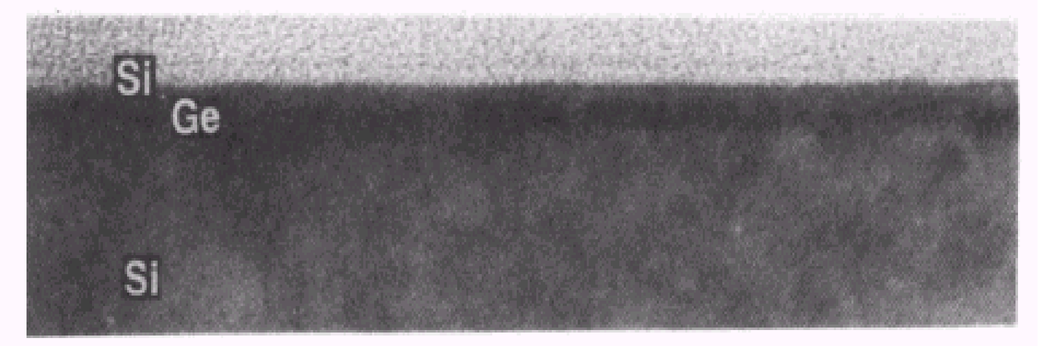

Figure 2.6 Cross-sectional views of 12 ML Ge/Si(001) with As as a surfactant. From *LeGoues et al.*[52]

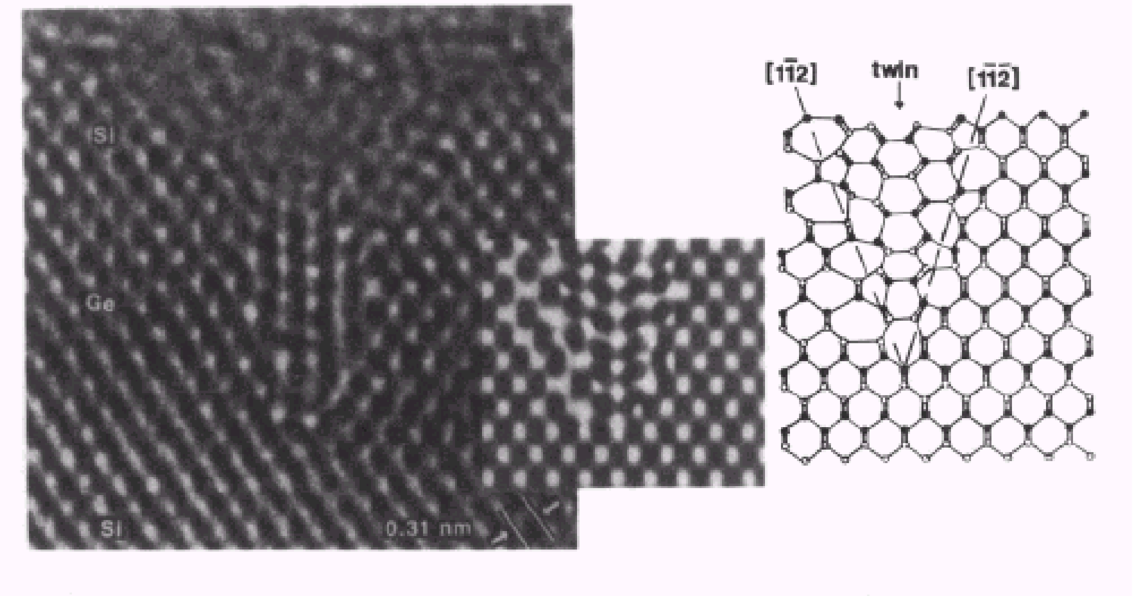

Figure 2.7 Cross-sectional view of one defect in the 12 ML film, atomic model, and corresponding image simulation. From *LeGoues et al.* [52]

The method of strain relief in Ge/Si(111) is slightly different. Surfactants such as Sb have proved to increase the critical thickness from 3-4 ML to 8 ML. Unlike the case of Ge on Si(001), Shockley partial dislocations [53] are introduced both with and without the Sb surfactant. However, the dislocation nucleation and motion is quite different for the case of films grown with or without surfactant. In the island growth case (no surfactant), dislocations glide from the edges of the islands along or near the interface. The edges of the islands provide sites for nucleation of Shockley partial dislocations resulting in threading stacking faults when the islands finally coalesce. During layer-by-layer growth (the case when a surfactant is used), the Shockley partial dislocation can only be introduced at the surface. The defects can thread through the film and glide along the interface. Subsequent Shockley partials are nucleated and self-annihilate. This allows for the creation of a relaxed, defect-free Ge film with all of the strain relieving defects located in the plane of the interface and no detectable threading defects. This is illustrated in Figure 2.8 (50 ML of Ge on Si(111) with Sb as a surfactant). It is clear that the Ge layer is atomically flat. Two lines are drawn to illustrate the difference between faulted and unfaulted (coherent) regions.

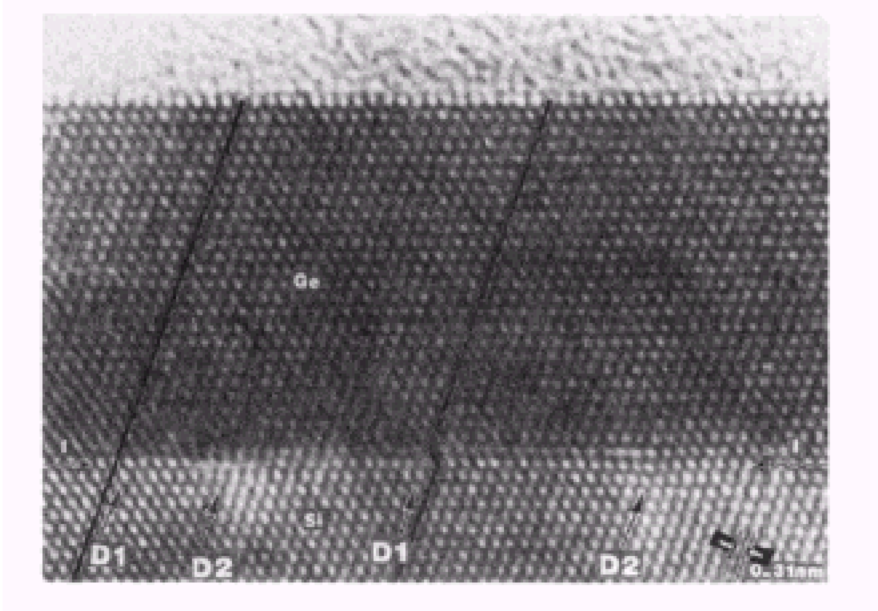

Figure 2.8 High resolution micrograph of 50 ML of Ge deposited on Si with Sb as a surfactant. Shockley partial dislocations are marked D1 and D2. The alteration of the faulted and unfaulted regions has been highlighted. From *Legoues et al.* [53]

Chapter 3 X-ray Diffraction

3.1 Introduction

X-rays are electromagnetic radiation with a wavelength near 1 Å. This makes x-rays an excellent probe of the structure of matter in its variety of forms. The reason being is that the spacings between atoms are also on the order of the wavelength of x-rays. X-rays also have the advantage over charged particle beams of having a high penetrating power which allows for *in-situ*, non-destructive investigation of buried interfaces. Therefore, diffraction by these electromagnetic waves has become an important tool for determining the structure of materials. Here I will present a brief outline of x-ray scattering and diffraction leading to a discussion of surface x-ray diffraction. Further detail on this subject can be found elsewhere. [54]

3.2 Kinematical theory for x-ray scattering

The elastic x-ray scattering amplitude from a single electron by an incident wave with amplitude, A_0, given by the Thompson scattering equation:

$$A = A_0 \frac{r_e}{R} \quad . \tag{3.1}$$

This is for the scattering of x-rays polarized perpendicular to the plane of scattering (σ polarization case), $r_e = 2.818 \times 10^{-5}$ Å is the classical electron radius, and R is the distance from the electron. For the π polarization there is an additional cos 2θ, factor.

The detected quantity is the intensity, which is the time averaged squared magnitude of the wave-field amplitude, which gives:

$$I = I_o\left(\frac{r_e}{R}\right)^2 \qquad (3.2)$$

for the Thompson scattering intensity from one electron and σ polarization case.

For a solid, which has many electrons within it, the total x-ray scattering is the super-position of all the waves scattered by each electron. The interference between these waves is determined by the position and/or arrangement of the electrons, which is related by the phase of each wave. The equation for the scattered amplitude is then:

$$A = \sum_n A_0\left(\frac{r_e}{R}\right)e^{i\vec{q}\bullet\vec{r}_n} \quad , \qquad (3.3)$$

where $\vec{q} = \vec{k}_f - \vec{k}_i$ defines the momentum transfer between the final scattered and incident wavevectors. This sum over all electrons is then broken down into the periodic and repeating units of the solid. First, there are all the electrons within each atom. Second, each atom within the unit cell volume is added. The unit cell can be defined as having the minimum number of independent atoms (in the solid) and is repeated in all three dimensions of space to fill the volume taken by the solid. A solid with this specific periodic structure of a unit cell is defined as a crystal. The position for each electron can then be written:

$$\vec{r}_n = \vec{r}_Z + \vec{r}_i + \vec{R}_j \quad . \qquad (3.4)$$

This summation can also be broken into parts the scattering amplitude becomes:

$$A_T = A_o\left(\frac{r_e}{R}\right)\sum_j\sum_i\sum_z e^{i\vec{q}\bullet(\vec{r}_z+\vec{r}_i+\vec{R}_j)} \quad , \tag{3.5}$$

where the first sum is over the Z electrons in an atom, the next sum, j, is over the atoms in the unit cell, and the final summation is over all space. The first sum, Z, can be grouped together to give what is called the atomic scattering factor

$$f(q) = \sum_Z e^{i\vec{q}\bullet\vec{r}_z} \quad . \tag{3.6}$$

Here the classical approach can no longer be used, but the quantum mechanical scattering is used to calculated resulting atomic scattering factors. The quantum mechanical scattering is covered in Sakurai [55], while the conventional analytic formulae for the scattering factors are found in Ref. [56]. Next in the Equation 3.5 is the sum over the atoms within the unit cell, which can be grouped as

$$F(\vec{q}) = \sum_i f_i(\vec{q})e^{i\vec{q}\bullet\vec{r}_i} \quad . \tag{3.7}$$

Here f_i is the atomic scattering factor for the i^{th} atom at position $\vec{r}_i$. This result for the unit cell is called the structure factor. The structure factor function is the Fourier transformation of the electron density within the unit cell. The new equation for the scattering amplitude is then:

$$A_T = A_o\left(\frac{r_e}{R}\right)F(\vec{q})\sum_j e^{i\vec{q}\bullet\vec{R}_j} \quad . \tag{3.8}$$

where the summation over full volume of the crystal is in units of direction given by the bases vectors of the unit cell, $\bar{a}_1$, $\bar{a}_2$, and $\bar{a}_3$, giving:

$$\vec{R}_j = n_1^j\vec{a}_1 + n_2^j\vec{a}_2 + n_3^j\vec{a}_3 \quad . \tag{3.9}$$

The n_i's are integers from 0 to N_i, where N_i is the size of the crystal in the corresponding basis direction. The summation is then distributed in the three directions to give:

$$\sum_j e^{i\bar{q}\cdot\bar{R}_j} = \sum_{n_1,n_2,n_3} e^{i\bar{q}\cdot(n_1\bar{a}_1+n_2\bar{a}_2+n_3\bar{a}_3)} = S_{N_1}(\bar{q}\cdot a_1)S_{N_2}(\bar{q}\cdot a_2)S_{N_3}(\bar{q}\cdot a_3) \quad , \tag{3.10}$$

where :

$$S_N(x) = \sum_{n=0}^{N-1} e^{ixn} = \frac{\sin\left(\frac{1}{2}Nx\right)}{\sin\left(\frac{1}{2}x\right)} e^{i\frac{(N-1)}{2}x} \quad . \tag{3.11}$$

$| S_N (x)|^2$ is the N-slit interference function with diffraction peaks at $x = 2\pi m$ where m is an integer. The peak intensity is $| S_N (2\pi m)|^2 = N^2$. Therefore, the 3D crystal $|A_T|^2$ has diffraction peaks when satisfying the Laue conditions:

$$\begin{aligned} \vec{q}\cdot\vec{a}_1 &= 2\pi h \\ \vec{q}\cdot\vec{a}_2 &= 2\pi k \\ \vec{q}\cdot\vec{a}_3 &= 2\pi l \end{aligned} \quad . \tag{3.12}$$

More details of reciprocal space and its relationship to the physical periodic space of real crystals is covered elsewhere. [54, 57] The variables *h*,*k*,*l* at integer positions correspond to the Miller indices, which describe the vectors normal to planes of atoms within the crystal. These planes and their separation d_{hkl}, are the same used in the alternative derivation of x-ray diffraction to give Bragg's Law, $2d_{hkl}\sin\theta = \lambda$. $\left|S_N(x)\right|^2$ is a δ-like function. The x-ray scattered intensity from a 3D crystal becomes:

$$I = I_o\left(\frac{r_e}{R}\right)^2 \left|F(\bar{q})\right|^2 \left|S_{N_1}(\bar{q}\cdot\bar{a}_1)\right|^2 \left|S_{N_2}(\bar{q}\cdot\bar{a}_2)\right|^2 \left|S_{N_3}(\bar{q}\cdot\bar{a}_3)\right|^2 \quad , \qquad (3.13)$$

which for N_1, N_2, and N_3 very large gives the result that the diffraction is concentrated at points in reciprocal space where the Laue condition is satisfied. The intensity result above can be also viewed as the modulus of the Fourier transformation for the whole crystal. The crystal's well defined periodicity results in sharply defined peaks in reciprocal space. The structure factor, $F(\bar{q})$, is the Fourier transform of the electron density within one unit cell. By measuring the strength of the Bragg peaks and quantifying the structure factor from a material of interest, its atomic structure within the unit cell can be determined. Typical diffraction experiments measure an integrated intensity, which is the angular and volume integration in reciprocal space. This results in the following equation:

$$I_{int} = I_o {r_e}^2 \frac{\lambda^3 V}{\omega \nu_a^2 \sin 2\theta} \left|F(h,k,l)\right|^2 \quad . \qquad (3.14)$$

The experimental parameters are V, the crystal volume, ω, the angular stepping speed of integration, ν_a, the unit cell volume, and $\sin 2\theta$, the Lorenz factor.

One final detail is that once the moduli of the structure factors are measured, the inverse transformation to the atomic structure is not directly possible because one lacks the complex structure factors' phases. This is called the phase problem and is usually solved by the indirect method of least squares refinement to a proposed model.

The atoms and/or their positions are then parameters to calculate model structure factors, which are then compared to the measured structure factor by the χ^2 distribution function:

$$\chi^2 = \frac{1}{N-p}\sum_{i=1}^{N}\frac{\left|F_i - F_i^{\mathrm{model}}\right|^2}{\sigma^2} \quad . \tag{3.15}$$

The measurement uncertainties, σ, and the number of parameters, p, are normalization factors of the refinement to the N data points.

3.2.1 Surface x-ray diffraction

In the study of structure of surfaces, scientists have typically used electron based techniques, such as LEED, due to their strong interaction with matter and thus small penetration depth. X-rays interact much more weakly with matter and until twenty years ago were not well suited for surface science. The advancement of high brightness synchrotron x-ray radiation sources has led to the creation of powerful x-ray based surface science techniques. Perhaps the most comprehensive technique for solving surface structure is surface x-ray diffraction (SXRD). [58, 59] In this experiment, as shown in Figure 3.1, x-rays are directed towards the sample at an angle, α, and exit the sample at an angle, β. Typically one of these angles is kept just above the critical angle for total external reflection so as to increase the surface sensitivity. The discussion in the previous section can be extended to the measurement of 2D structures, namely surfaces. A surface can be viewed as a defect of a crystal where the periodicity is stopped, or “truncated”, in one direction. This boundary, or sharp discontinuity, will cause the Fourier transformation to give a continuous distribution of diffraction intensity. The distribution, in reciprocal space, is perpendicular to the surface, i.e. in the truncated direction of periodicity. Another example is an ideal 2D crystal where there is no periodicity in the third direction.

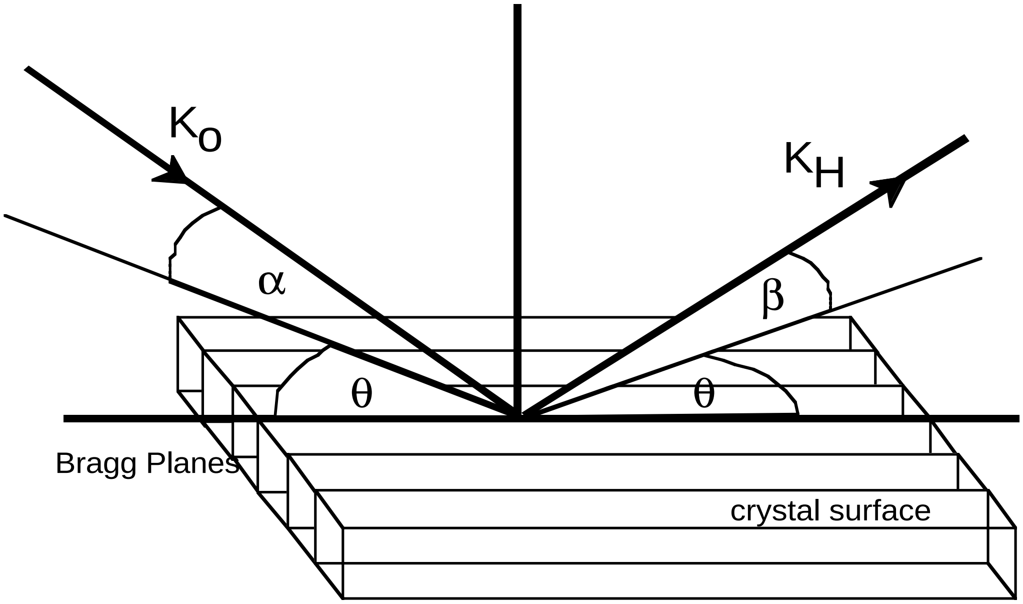

Figure 3.1 Surface x-ray diffraction geometry.

A similar unit cell can be defined for the 2D crystal, but it will now have only two basis vectors. The summation over all space will be distributed in only two directions so that the summation in reciprocal space will result in a third real space direction that is freely defined perpendicular to the 2D plane. The reciprocal space basis directions are then $\bar{a}_1$, $\bar{a}_2$, in the 2D plane. $\bar{a}_3$ is perpendicular, out-of-plane. The intensity result is:

$$I(\bar{q}) = I_o\left(\frac{r_e}{R}\right)^2 |F(\bar{q})|^2 \left|S_{N_1}(\bar{q}\cdot\bar{a}_1)\right|^2 \left|S_{N_2}(\bar{q}\cdot\bar{a}_2)\right|^2, \qquad (3.16)$$

which does not have a Laue condition in $\bar{a}_3$. With respect to this direction, the only dependence is in the structure factor function, which is a continuous function because it is defined for a single unit cell. In the other two directions, the *h* and *k* Laue conditions still apply because of the 2D periodicity. The resulting intensity pattern is in the form of rods, periodic with δ-functions at integer position in variables *h* and *k*, but continuous in *l*.

Returning to a real crystal surface, one way to derive the diffraction result is to use the 2D result above to build a crystal in one half-space. The perpendicular summation for $N_3 \to \infty$ can then be written as :

$$S\copyright = \sum_{n_3=0}^{-\infty} e^{i(\bar{q}\cdot\bar{a}_3)n_3} = \frac{1}{1-e^{-i(\bar{q}\cdot\bar{a}_3)}} \qquad , \qquad (3.17)$$

which modulus squared for intensity becomes:

$$I_{CTR} = I_o\left(\frac{r_e}{R}\right)^2 |F(hkl)|^2 \left|S_{N_1}(\bar{q}\cdot\bar{a}_1)\right|^2 \left|S_{N_2}(\bar{q}\cdot\bar{a}_2)\right|^2 \frac{1}{2\sin^2\left(\frac{1}{2}\bar{q}\cdot\bar{a}_3\right)} \qquad (3.18)$$

except at $\bar{q}\cdot\bar{a}_3 = 2\pi l$. The 1/sin^2 function still gives a continuous line of diffraction intensity, but now the function is peaked again at integer values of *l*. This result gives what are called crystal truncation rods (CTR) which are rods of intensity that decay as

$1/q^2$ away from the Bragg peaks in the direction perpendicular to the surface. This result is for the simplest ideally terminated crystal, but in general the distribution of intensity along the CTR is determined by the surface structure. Details such as roughness, vacuum relaxations, adsorption, desorption, and electro-chemical reactions and/or changes at the surface will affect the CTR distribution. And consequently, CTR can be used to determine these changes in surface structure. [60]

Crystal truncation rods are useful in the analysis of thin films as well as surfaces. A thin film has two surfaces which can give complex distributions along rods from the interference of scattered waves. As will be demonstrated in Chapter 5, the summation similar to the ones above in a direction perpendicular to the film interface results in a function which oscillates in intensity. This oscillation is then related to the length scale or thickness of the thin films.

The kinematical theory presented in this section illustrates why x-ray diffraction is such a powerful tool for determining the atomic structure of materials, surfaces, and thin films. The weak Thompson scattering from electrons makes calculation and interpretation of x–ray diffraction patterns easier than most other diffraction techniques. In addition to the kinematical process, another advantage is that the x-ray diffraction measurements are an average over sample volume or surface. Very dilute and random defects or structures in samples will scatter weakly and not affect the accumulative average microscopic picture of the atomic structure.

3.3 Dynamical theory of x-ray diffraction

For most applications in x-ray diffraction, kinematical theory is sufficient for simulating diffracted intensity from materials. For much of this thesis this will be the case, however, for the studies discussed in Chapter 5, a more rigorous treatment of diffraction is necessary. [61] Consider the case of a crystal that is entirely irradiated by the incident beam and is non- absorbing (for simplification). According to Kinematical theory in equation 3.14, the diffracted x-ray integrated intensity is the ratio of the total energy received by the detector, while the crystal is rotated, divided by the intensity of the incident beam. This expression shows that the integrated intensity diffracted by a small crystal entirely bathed in the incident radiation is proportional to its volume. Kinematical theory takes the amplitudes diffracted by each scattering center and adds them by only taking into account the interferences due to the differences in optical path. It does not consider multiple scattering. This works quite well for thin crystals due to the weak interaction between x-rays and matter, however, this treatment falls short for ideal crystals that approach a thickness of Λ, which is called the extinction length. For a semi-infinite and perfectly periodic crystal, the reflection domain would be reduced to a Dirac $\delta-$function distribution and would be represented by a single point in reciprocal space (neglecting thermal agitation and local disorder).

As in the previous section we will be interested in obtaining an expression for normalized reflectivity from perfect crystals. Furthermore, for our purposes, we are interested in expressions for the amplitude and phase relationship between incident and reflected waves.

Consider a medium with a continuous distribution of charges. Under the influence of a propagating electromagnetic wave, the local electric charges oscillate and the medium becomes polarized. The polarization of the medium (P(**r**)) is related to the electric field (E(**r**)):

$$\varepsilon_o E(\mathbf{r}) + P(\mathbf{r}) = \varepsilon_o (1 + \chi_r) E(\mathbf{r}) \quad . \tag{3.19}$$

In this equation, χ_r is the dielectric susceptibility or polarizability. For X-rays with energy far from an absorption edge, the polarizability can be written as:

$$\chi = \chi_n + \chi_a + i\chi_i \quad , \tag{3.20}$$

where χ_a and χ_i are the anomalous dispersion corrections due to the presence of absorption edges. Far away from these points, the corrections are usually small, therefore the polarizability can be written:

$$\chi_n(\mathbf{r}) = \frac{-\rho(r) r_e \lambda^2}{\pi} \quad , \tag{3.21}$$

where r_e is the classical electron radius. Equation (3.21) shows that the polarizability of matter for x-rays is very small, negative, and proportional to the electron density $\rho(\mathbf{r})$, therefore varying with the space coordinates.

A graphical representation of diffraction in reciprocal space can be developed with the use of the Ewald sphere. [62] The Laue condition, $\bar{q} = h\bar{b}_1 + k\bar{b}_2 + l\bar{b}_3$, defines the Laue point, which is situated on the intersection of two spheres centered at the reciprocal lattice nodes O and H and with radii k=1/λ (Figure 3.2). Notice that the previously defined Laue condition is equivalent to the vector equation $\overline{K}_H - \overline{K}_o = \vec{H}$. If an incident wave such as OM does not satisfy Bragg's condition rigorously, there would be no reflected wave according to the kinematical theory. As described by the previous discussion, the waves propagating in a medium interact with matter. The index of refraction is related to the polarizability through $n \approx (1 + \chi_o / 2)$.

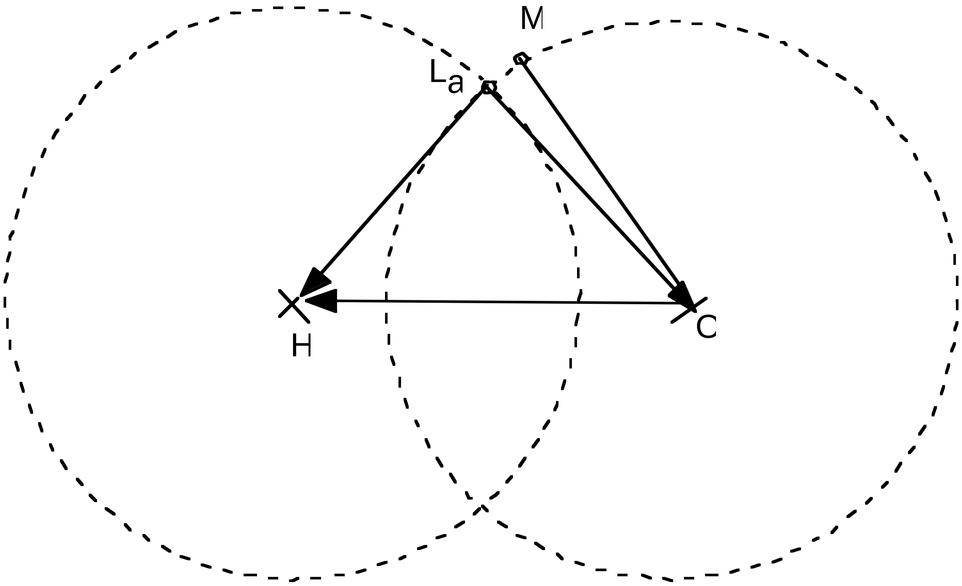

Figure 3.2 Diffraction according to kinematical theory in reciprocal space. **OH =** $\vec{\mathbf{H}}$: reciprocal lattice vector; L_a: Laue point; $\mathbf{L_a}$**,O** incident wave vector ($\overline{\mathbf{L_a O}} = \overline{k}$) and $\mathbf{HL_a}$, reflected wave vector ($\overline{\mathbf{L_a H}} = \overline{k}$) satisfy Bragg's condition; **MO**: incident wave vector which does not satisfy Bragg's condition.

The wave vector moduli satisfying the diffraction condition are therefore nk (Figure 3.3) and the point representing the reflection domain in reciprocal space is on the intersection of two spheres with the same centers, but with nk as radius. This point has been called the Lorentz point by Ewald. The wave propagating in the incident direction is called the refracted wave. Since the index of refraction is smaller than one for X-rays, these two spheres lie inside the spheres with radius k. In this thesis I will only consider the two-beam case where there are two reciprocal lattice points simultaneously on the Ewald sphere, O and H. When the crystal is rocked through the reflection condition, it is not possible that the reflected beam occurs for one angular position only of the crystal as it does in kinematical theory. For every position of the crystal within the reflection domain, there is a refracted wave of wavevector $\mathbf{K_o} = \mathbf{PO}$ and a reflected wave $\mathbf{K_H} = \mathbf{PH}$**.** For reasons of symmetry, P cannot lie on either of the two spheres, and therefore must lie on a connecting surface between the two spheres (Figure 3.4). When the point P lies on the connecting surface, there are two waves and both their wave numbers differ slightly from nk. This surface, which has two sheets, is called the dispersion surface. The angular width of the reflection domain is represented in reciprocal space by the size of this connection surface between the two spheres.

The Fourier coefficients of the polarizability are of the order of 10^{-5} to 10^{-6}. The size of the dispersion surface is therefore very small with respect to the radius of the Ewald sphere, and the internal wave vectors K_o and K_H are very close to one another and to k. The common extremity, P, of the two wavevectors has been called a tiepoint to stress that the two waves are closely linked together to form a wavefield.

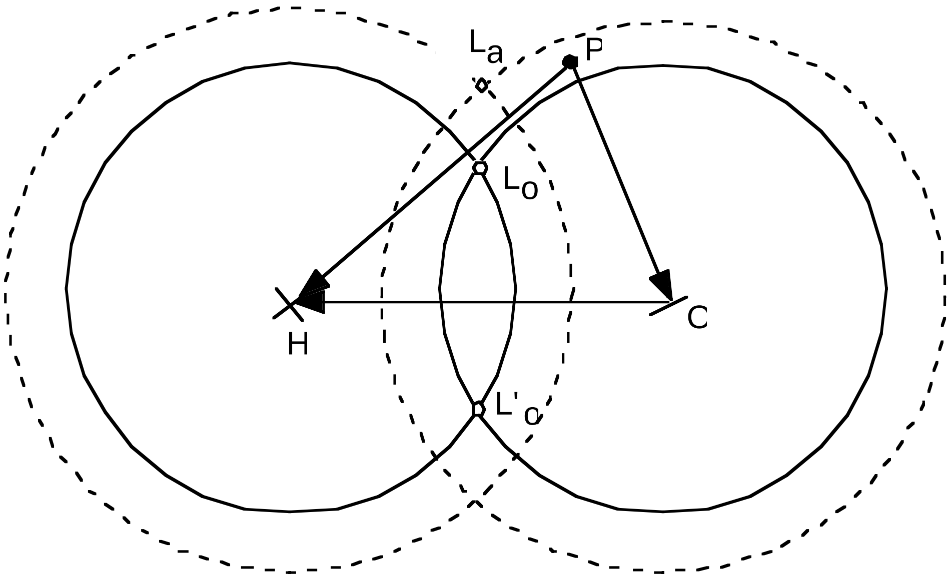

Figure 3.3 Influence of the index of refraction. L_o Lorentz point; $\overline{OL_o} = \overline{HL_o} = nk$, where n is the index of refraction; **PO**: refracted wave vector; **PH**; reflected wave; $L_o^{\copyright}$: Lorentz point associated with the reciprocal lattice vector **OH** = $\overline{\mathbf{H}}$.

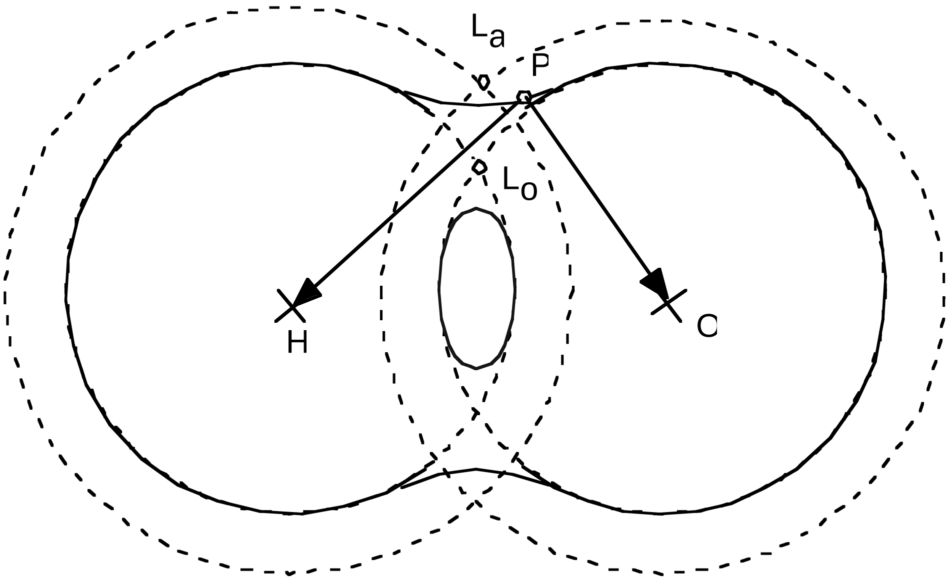

Figure 3.4 Interaction of the refracted (**PO**) and reflected (**PH**) wave vectors. Solid curve: dispersion surface; P: tiepoint.

The solutions to Maxwell's equations for electromagnetic waves [61] propagating in periodic medium are similar to those for electrons. [57] In the case of electrons, one looks for the possible energies of electrons as a function of their wavenumber where as with x-rays the energy is fixed and one looks for the possible positions of the wavevectors in reciprocal space. Consider a crystalline medium where $\rho(r)$ is a triply periodic function of the space coordinates as well as χ. The polarizability can therefore be expanded in a Fourier series:

$$\chi = \sum_{H} \chi_H \exp(2\pi i \mathbf{H} \cdot \mathbf{r}) \tag{3.22}$$

where there exist similar equations for χ_r and $\chi_{i.,}$. χ_H are related to the structure factor by $\chi_H = -\Gamma F_H$ where $\Gamma = \frac{r_e\lambda^2}{\pi V_{u.c.}}$. If for a moment one only considers one direction of polarization, electromagnetic waves can be treated as scalar waves (as electron waves are treated). This simplifies the algebra significantly and solutions for electromagnetic waves propagating in such a medium satisfy the following equation:

$$\Delta\Psi + 4\pi^2 k^2[1+\chi(\mathbf{r})]\Psi = 0\,. \tag{3.23}$$

where the wavefunctions, ψ, are of the following form:

$$\Psi(\mathrm{r}) = \exp(-2\pi i\mathbf{K_o}\cdot\mathbf{r})\sum_{\mathbf{H}}\Psi_H\exp(-2\pi i\mathbf{H}\cdot\mathbf{r})\,. \tag{3.24}$$

This wavefunction is commonly known as a Bloch wave. It clearly shows that solutions of the wave equation for a periodic potential are the product of a plane wave times a function with the periodicity of the crystal lattice. By substituting equations (3.22) and (3.24) into equation (3.23) and defining $\mathbf{K_h} = \mathbf{K_o} - \mathbf{H}$, one can obtain a set of solutions for wavefunctions for electromagnetic waves.

$$\Psi_H = \frac{k^2}{K_H^2 - k^2}\sum_{H©}\chi_{H-H©}\Psi_{H©}\ . \tag{3.25}$$

This equation is used to generate solutions for n-beams that happen to have nodes lying on the Ewald sphere simultaneously. In our experiments we are interested in the two beam case where only the 0th and Hth term are non-zero and the equation (3.25) becomes:

$$\Psi_o = \frac{k^2}{K_o^2 - k^2}[\chi_o \Psi_o + \chi_{\bar{H}} \Psi_H], \tag{3.26}$$

$$\Psi_H = \frac{k^2}{K_H^2 - k^2}[\chi_H \Psi_o + \chi_o \Psi_H],$$

where $\chi_{\bar{H}}$ is the Fourier coefficient of the polarizability corresponding to the $\bar{h}, \bar{k}, \bar{l}$ reflection. For non-trivial solutions of these linear, homogeneous equations to exist, the determinant should be equal to zero. The equations can be rearranged in the following way:

$$\left[\frac{K_o^2 - k^2}{2k} - \frac{k\chi_o}{2}\right]\Psi_o - \frac{k\chi_{\bar{H}}}{2}\Psi_H = 0 \tag{3.27}$$

$$-\frac{k\chi_H}{2}\Psi_o + \left[\frac{K_H^2 - k^2}{2k} - \frac{k\chi_o}{2}\right]\Psi_H = 0 \quad .$$

At this time it is helpful to define the following quantities to simplify the algebra:

$$X_o = \frac{K_o^2 - k^2}{2k} - \frac{k\chi_o}{2} \tag{3.28}$$

$$X_H = \frac{K_H^2 - k^2}{2k} - \frac{k\chi_o}{2}.$$

X_o and X_H are referred to as the dispersion parameters. The determinant of equations 3.27 using the above substitutions gives the secular equation, which is the equation of the dispersion surface:

$$X_o X_H = k^2 \chi_H \chi_{\bar{H}} / 4 \quad . \tag{3.29}$$

It shows that the product of the distances of P from the two spheres passing through the Lorentz point is constant and that the dispersion surface is a surface of revolution around axis OH. Close to the Lorentz point, these two spheres can be replaced by their tangential planes and their intersections by the diffraction plane can be replaced by two straight lines (unless the reflection is highly asymmetric). In addition to describing the directional and absorptive properties of a wave, the tie points on the dispersion surface also characterize the ratio of the field amplitudes. From equations (3.26) and (3.28) we obtain:

$$\begin{gathered} \xi = \frac{\Psi_H}{\Psi_o} \\ \xi^2 = \frac{\chi_H}{\chi_{\bar{H}}} \frac{X_o}{X_H} \end{gathered} \quad . \tag{3.30}$$

Notice that the ratio, ξ, is negative for the α branch and positive for the β branch. It is also important to note that for the non-absorbing case, the phase of the β branch is equal to φ which is the phase of the structure factor. This branch is π out of phase with respect to the α branch.

The equation for the dispersion surface (Figure 3.5) is the equation of the hyperbola whose asymptotes are the lines, T_o and T_H. The Poynting Vector (**S**) is a vector describing the direction of propagation of energy of the particular wavefield. The expression for the Poynting vector is:

$$S \propto \Psi_o^2 \left[\mathbf{s_o} + |\xi|^2 \mathbf{s_H} \right] \tag{3.31}$$

and its angle, γ, with respect to the direction of the reflecting planes is given by:

$$\tan\gamma = \frac{1-|\xi|^2}{1+|\xi|^2}\tan\theta_B \quad . \tag{3.32}$$

Figure 3.5 shows the Poynting vector associated with tiepoint P. Its orientation varies from that of the refracted wave vector, **PO**, to that of the reflected wave vector, **PH**. On one side of the reflection domain, its orientation is that of **PO** for the α branch with $\xi = 0$, while it is that of **PH** for the β branch with $\xi \to \infty$. On the other side of the reflection domain, the situation is the other way around. In the middle of the reflection domain, when the tiepoint is in A_{01} or A_{o2}, the propagation direction is parallel to the lattice planes.

Going back to Equation 3.26 and using terms defined in this section, we can generate an expression for two Bloch waves that are coherently coupled. These waves add together and result in a traveling wave moving along the bisector of the angle between K_o and K_H and a standing wave at right angles to this direction. The addition of these waves can be written as follows:

$$\Psi(\mathrm{r}) = \Psi_o \exp(-2\pi i\mathbf{K_o}\cdot\mathbf{r})\left[1+\xi\exp(2\pi i\mathbf{H}\cdot\mathbf{r})\right] \quad , \tag{3.33}$$

where the intensity is:

$$|\Psi(\mathrm{r})|^2 = |\Psi_o|^2\left[1+|\xi|^2+2|\xi|\cos\{2\pi(\mathbf{H}\cdot\mathbf{r})-\phi\}\right] \quad . \tag{3.34}$$

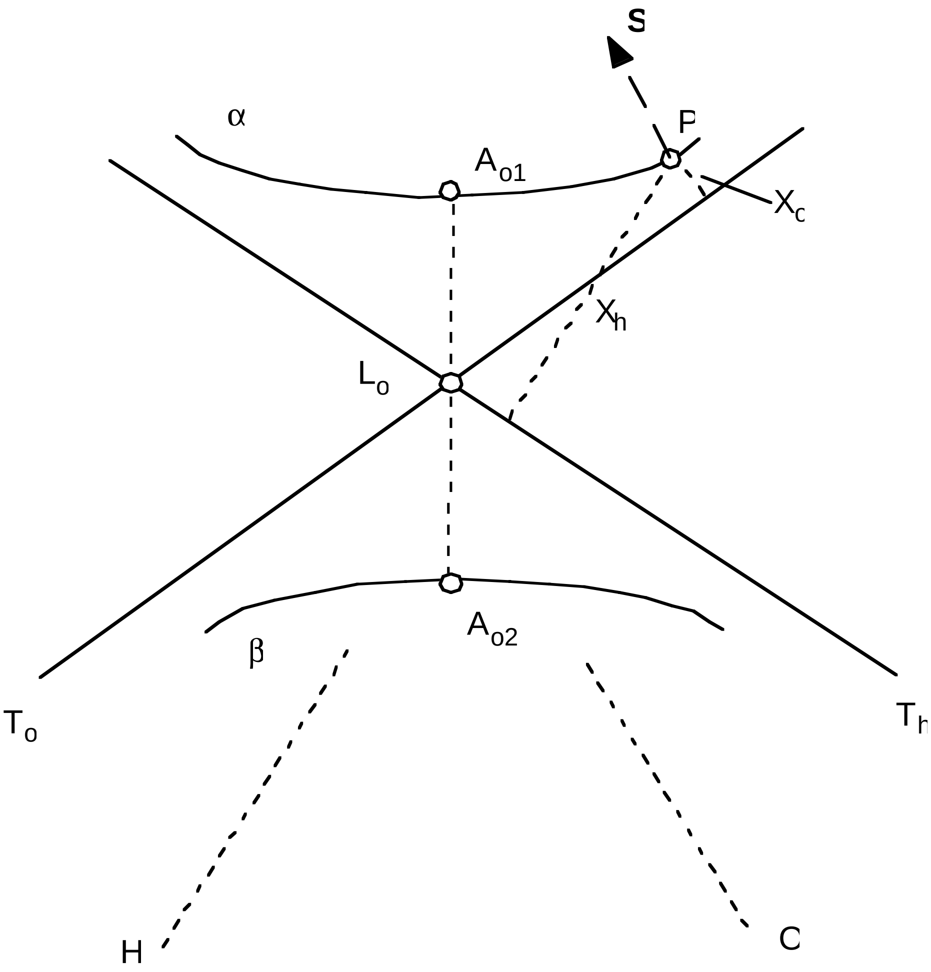

Figure 3.5 Dispersion surface. P: tiepoint of wavefield; S: Poynting vector of that wavefield; X_o and X_H coordinates of the tiepoint; A_{01}, A_{02}: vertices of the dispersion surface.

We can see from this equation that the planes of constant intensity, i.e. the standing wave pattern, occur when **H•r** is a constant, and hence, are parallel to the diffraction planes and spaced $|\mathbf{H}|^{-1} = d_{hkl}$ apart.

In the Bragg reflection geometry, the incident and reflected waves enter and exit on the same face of the crystal. For the case of a symmetrical reflection (angles of incident and outgoing waves are equal), the ratio of the complex amplitudes Ψ_o and Ψ_H of the incident and reflected waves, respectively, is given by:

$$\frac{\Psi_H}{\Psi_o} = \left(\frac{\chi_H}{\chi_{\overline{H}}}\right)^{1/2}\left[\eta \pm \left(\eta^2 - 1\right)^{1/2}\right]. \tag{3.35}$$

This is the case for σ polarized x-rays, where the E-field vectors of the incident and outgoing waves are collinear and normal to **H.** The complex variable, η, is a function of the angle via:

$$\eta = \frac{\left(\theta_B - \theta\right)\sin(2\theta_B) - \chi_o}{(\chi_H \chi_{\overline{H}})^{1/2}} \quad , \tag{3.36}$$

and is typically called the deviation parameter.

3.3.1 X-ray standing waves

When two coherently coupled waves overlap, they interfere, generating a set of standing waves (Figure 3.6). For example, when the second wave is due to the Bragg reflection, a standing wave field exists both above and below the crystal surface where reflection takes place. If either an impurity or host atom is located at an antinode of the electric field, secondary emission of fluorescence radiation is excited. By moving the position of the nodes and antinodes in a known way while monitoring x-ray fluorescence from atoms in the crystal, it is possible to find where the atom is located with respect to the set of standing waves and therefore, with respect to the crystal lattice. One can thus determine the registry of the adsorbed atoms with respect to the underlying bulk lattice.

Ignoring the extinction effect, the normalized intensity of the standing wavefield at a position $z = \mathbf{H} \cdot \mathbf{r}$ in the unit cell is given by (3.36)

$$I_{SW} = 1 + |\xi|^2 + 2|\xi|\cos(\phi - 2\pi\mathbf{H}\cdot\mathbf{r}) \quad , \tag{3.37}$$

where ϕ is the phase of ξ. It is important to note that z is a numerical coordinate representing the position of a point in the unit cell as a fraction of the reflecting-plane spacing, d_{hkl}. In the dipole approximation of the photoeffect, the probability of x-ray fluorescence is proportional to the intensity of the standing wavefield at the center of the atom. Earlier studies [63, 64] have shown the fluorescence yield normalized to the yield far from the reflection domain is:

$$Y(\Delta\theta) = c\int_{u.c.} I_{SW}((\Delta\theta, z))\rho_u(z)dz \quad . \tag{3.38}$$

In this equation, c is a normalization constant and ρ_u is the atom distribution within the unit cell.

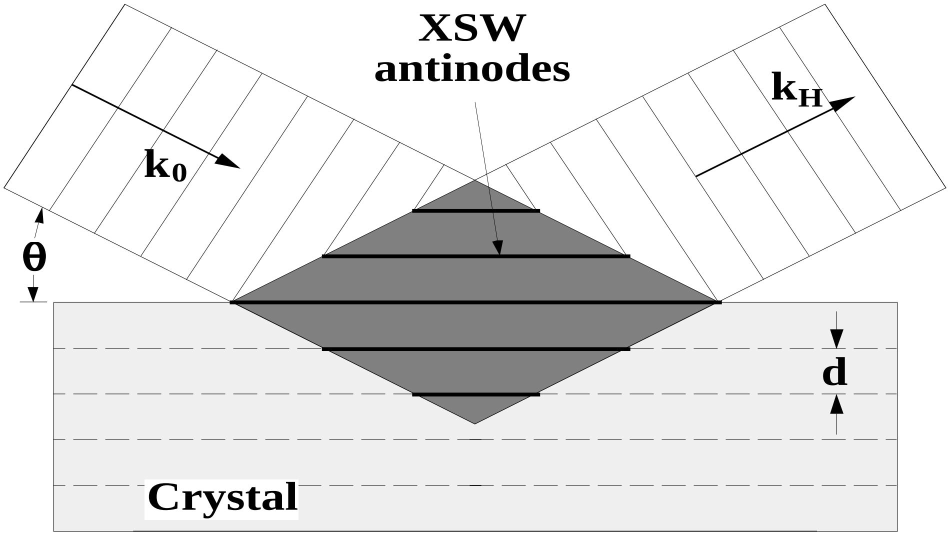

Figure 3.6 Standing wave field generated from interference of incident, K_o, and Bragg diffracted, K_H, waves.

Assuming that the dipole approximation for the photoeffect comes from the center of the atom, one can write:

$$\rho_u(z) = \sum_{j=1}^{N} \delta(z - z_j) \quad , \tag{3.39}$$

where N is the number of atoms per unit cell.

In order to analyze the experimental results, it is typical to express the normalized yield (Y(Δθ)/Nc) in the following way:

$$\frac{Y(\Delta\theta)}{Nc} = 1 + R^2 + 2\sqrt{R} f_H \cos(\phi - 2\pi P_H) \quad , \tag{3.40}$$

where the reflectivity, R = $|\xi|^2$, and f_H and P_H are two adjustable parameters to fit the experimental curve by comparison with the theoretical curves; f_H is called the coherent fraction, and P_H is the coherent position. It has been shown that the standing wavefield

Fourier components ($\mathcal{F}_H$) should include a Debye-Waller factor as does the usual scattering structure factor:

$$\mathcal{F}_h = \frac{1}{N}\sum_{j=1}^{N} \exp(-M_j)\exp(2\pi i\mathbf{H}\cdot\mathbf{r_j}) \qquad (3.41)$$

where:

$$\mathrm{M_j} = \frac{1}{2}\left\langle 2\pi\mathbf{H}\cdot\mathbf{u_j}\right\rangle^2 \qquad (3.42)$$

and $\left\langle \mathrm{u_j}\right\rangle^2$ is the squared time averaged displacement of atom j due to the thermal vibrations. A careful analysis of the thermal vibrations requires the measurement of several Fourier coefficients of the atomic density distribution and in particular, of higher order coefficients. The rocking curve widths of the high-order reflections are very narrow, which makes the standing wave measurements very difficult.

We can now relate our Fourier components ($\mathcal{F}_H$) to our experimentally measured f_H and P_H values as follows:

$$\mathrm{f_H} = \left|\mathcal{F}_\mathrm{H}\right| \qquad (3.43)$$

$$\mathrm{P_H} = \frac{1}{2\pi}\arg(\mathcal{F}_H) \quad . \qquad (3.44)$$

These equations will be used in a less general form in Chapters 5 and 6 as they are applied to specific experimental cases.

Chapter 4 Te/Ge(001)

4.1 Si (001) and Ge (001)

Atomic scale structural properties of Si and Ge surfaces have received much of attention in the past 20 years; in particular, the Si(001) and Ge(001) surfaces, as they are the surfaces on which electronic devices are manufactured. At room temperature, a bulk truncated semiconductor crystal is unstable and will under go “reconstruction” on the surface. There are several principles that govern the equilibrium structure of elemental semiconductor surfaces. In general, chemical bonding and charge neutrality are the major driving forces.

Si and Ge are tetrahedrally coordinated semiconductors possessing strong, hybridized, directional covalent chemical bonds. In the bulk, each bond contains two spin-paired electrons. When a surface is formed, some of these bonds will be broken leading to surface charge densities which contain only one unpaired electron. These “dangling bonds” are unstable, hence, the atoms in the surface region relax from their bulk positions in order to reduce the surface free energy by forming new bonds. The atomic structure of the room temperature Si(001) clean surface results in a 2 x 1, two domain LEED pattern. This result is explained easily by 2 x 1 and 1 x 2 Si surface unit cells making up the two domains which are separated by single atomic steps. [65] The two neighboring surface atoms are pulled together to form a dimer along the [110] direction so as to reduce the number of dangling bonds. As seen in Figure 4.1(b), the dimers are not symmetric, rather they are “buckled” as was first seen using STM [66] and verified by diffraction.[67] While a surface by definitions is 2D, surface reconstructions are actually 3D in nature as the near surface atoms undergo vertical atomic relaxations. An example of this is the tilting of the dimers on Si (001) and Ge (001). If the dimers were untilted, the occupied and unoccupied π bands associated with the surface dimers would overlap and the chains of dimers along the surface would form a semi-metal (semimetals are unstable in 1D [68]). Obviously, local coordination chemistry considerations alone are inadequate in accounting for all surface structures. Another important point is that the surface structure observed will be the lowest free-energy structure kinetically accessible under the preparation conditions. A clear example of this is the fact that low temperature cleavage of Si(111) produces a (2x1) reconstruction, whereas annealing to high temperatures produces the well known Si(111) 7x7 which is stable upon subsequent cooling. [69]

4.2 Adsorbate induced reconstructions

The driving forces for adsorbate induced reconstructions on Ge and Si are similar to those for the native surfaces. Atomic size and electron valencey become important issues to consider for adatoms on Si and Ge. Technologically, Si(001) and Ge(001) surfaces with Group III and V adsorbates are of importance for many reasons.

Recently there is a tremendous effort to develop alternative systems such as III-V semiconductors (*e.g*. GaAs, InP) since III-V semiconductors are intrinsically high speed material and have direct band-gap which promises many electro-optical applications. However, technical difficulties in processing and manufacturing III-V materials hinders the development. The alternative method is to grow III-V heteroepitaxial thin films on Si and therefore combine the advantageous properties of III-V semiconductors with the mature Si manufacturing technologies. Investigations of Group III or V metals adsorbed on Si(001) surfaces has and will continue to provide the necessary information for understanding the initial growth stage of III-V semiconductors on Si(001). This may aid in eventually solving the technical difficulties associated with the III-V / Si heteroepitaxy such as the anti-phase domain problem.[70] The investigation of Group V terminated Si(001) surfaces is also motivated by another important technological issue --- surfactant-mediated epitaxy (SME). Much effort has been put into the development of growing heteroepitaxial Ge thin films on Si. Evidenced from discussion in Chapter 2, it has been found that preadsorption of a monolayer of certain foreign adsorbate (surfactant) species can, to a certain extent, change the growth mode of the Ge layer on Si from 3D growth to layer-by layer. Group V and VI elements (As, Sb, Bi, Te) have been found to be the most effective surfactants for the growth of Ge on Si (001). Studying the submonolayer adsorption of the elements on Si (001) and Ge(001) may help in obtaining useful knowledge to fully understand the initial stage of SME growth of Ge on Si(001).

The literature on Group III and V elements adsorbed on Ge and Si is quite extensive as compared with other elements. In the case of Group V elements such as As[71], Sb[72], and Bi[73] adsorbed on Si(001), dangling bonds are typically filled at Si dimer atoms, thus forming a symmetric dimer on top of an underlying unreconstructed Si (001) surface (Figure. 4.1 (c)). The adsorption saturates at slightly less than 1 ML and the saturated surface is highly ordered. In the case of Group III atoms (Al, In, and Ga) on Si (001), the structure is quite different. These elements only form an ordered structure at coverages at or below 0.5 ML. At these coverages, Group III adatoms tend to form dimers on top of and parallel to a dimerized Si(001) surface [74, 75]. After comparing the surface structure of Group V and Group III elements adsorbed on Si, it can be understood why Group V elements form a passivated surface and Group III elements do not [76].

The Group VI elements have received substantially less attention than Group III or V elements. Since Group VI elements are hexavalent, they have the property that ~1 ML of adsorbate can satisfy all dangling bonds without forming surface dimers and thus produce a surface displaying 1 x 1 symmetry (Figure 4.1d). LEED and XPS work for S deposited on Ge(001) has verified this restoration of symmetry and has predicted the S to adsorb on a bridge site. [77] Te [78, 79] and Se[80] are also predicted to occupy bridge sites on Si(001) and Ge(001) at high coverages, however, little is known about the low coverage reconstructions of these systems.

The bulk of this thesis is focused on the surfactant mediated growth of Ge on Si using Te. In order to understand the mechanisms for surfactant action in this system, a detailed understanding of parameters such as adsorption site, surface relaxations, and bondlengths for Te/Si(001) and Te/Ge(001) are important. Te on Si(001) has been studied by a number of surface science techniques, however, a number of questions still exist concerning the long range structure and surface relaxation of the high coverage structure. Moreover, the lower coverage surface reconstructions of this system have received very little attention at all. The low coverage structures of Te/Si(001) are particularly interesting due to the fact that surfactant action has been observed with Te coverages as low as 0.1 ML. [81] A recent systematic LEED study [82, 83] of Te/Si(001) reported three distinct diffraction patterns. Initially after depositing Te on Si(001) and annealing at 350^0, the structure LEED pattern was 1 x 1 (slightly streaked). Further heating resulted in a 2x1 pattern at 600^0C and a 1 x 3 pattern at 680^0C. At 800^0C the Te atoms desorbed completely and the clean surface Si 2x1 pattern returned. SEXAFS [84], XSW [84] and XPS [85] studies of the 1 x 1 structure have proposed that Te atoms adsorbs at bridge sites. This result has also been verified by using first principals total energy calculations. [86] STM experiments reported Te atoms adsorbing along dimer rows at low coverage, while at high coverage the Te atoms lined up perpendicular to the dimer rows. The high coverage (~5/6 ML) also displayed semi-periodic missing rows which later on were used to explain the streaks in some of the LEED patterns.[87] The adsorption sites for the lower coverage

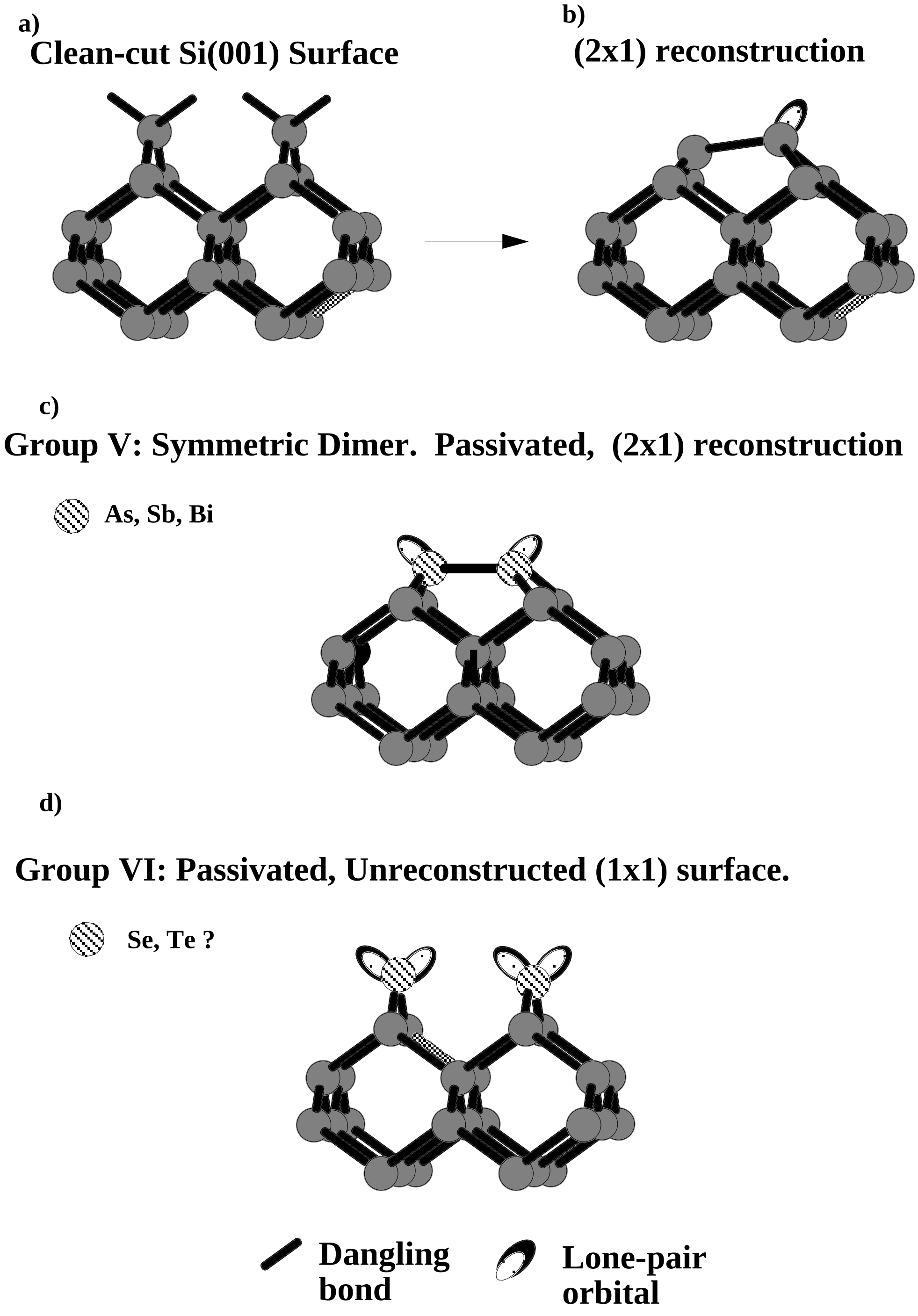

Figure 4.1 Surface structure of (a) bulk terminated, (b) reconstructed, (c) Group V terminated, and, (d) Group VI terminated Si (001) or Ge (001) surface.

reconstructions, (2x1) and (3x1), have only been studied by LEED and these LEED patterns display sharp superstructure peaks.

4.3 SXRD of Te/Ge(001) saturated surface structure

The Te/Ge(001) system has been even less studied than Te/Si(001). During the growth of Ge on Te terminated Si(001), a "streaky" 1 x 1 LEED pattern was reported up to a Ge thickness of ~11 ML, when a 2 x 2 pattern was then observed. [49] Based on LEED, XSW, and crystal truncation rod (CTR) studies, our group has proposed structures for both the high coverage "streaky" 1x1 (~0.8 ML) and low coverage c(2x2)(~0.5 ML) structures of Te/Ge(001). [79, 88] The proposed high coverage structure consists of Te atoms adsorbing on bridge sites that run perpendicular to the original Ge dimer rows. The streaks suggest a weak 2x1 periodicity that is currently under investigation. Upon annealing this structure at 420^0C for ten minutes a c(2x2) LEED pattern appears. Lyman *et al.* [79] have proposed a heterodimer model whereby Ge and Te form dimers on the surface, thereby satisfying all surface dangling bonds with only a coverage of 0.5 ML. This model is consistent with Te-Ge bondlengths as determined by their in-plane (022) XSW measurements and it suggests why Te is such an effective surfactant at low coverage.

The study focused on in this chapter is the determination of the high coverage Ge:Te structure mentioned above. For the unreconstructed Ge(001) surface there exist four high symmetry Te adsorption sites (see Figure 4.2). Our first goal was to determine the adsorption site by using surface x-ray diffraction (SXRD). Furthermore, we intended to develop a more refined model of the surface based on the adsorption site and by incorporating atomic scale displacements in the surface region. The experiment was performed using our (UHV) surface diffractometer at the 5ID-C station on the DND undulator beamline at the Advanced Photon Source (APS). [89] This system is multi-purpose and has capabilities such as ion sputtering cleaning, annealing, and solid source MBE; and surface analysis via LEED, Auger electron spectroscopy, x-ray standing waves and surface x-ray scattering. A UHV introduction chamber has also been installed for the purpose of storing prepared samples for more efficient x-ray measurements during the allotted brief undulator beam time.

The Te/Ge(001) high coverage structure was the first UHV experiment for this facility. The sample was prepared by a similar method as previously reported for Ge (001): Te 1 x 1. [14] We outgassed the substrate for ten minutes at 970 K via indirect heating and sputtered it for 1 hour at 720 K using 1 keV Ar + ions with a differentially pumped phi model ion gun. The substrate was then annealed for ten minutes at 960 K followed by a slow cooling of about 2 ^{o}/ s. This cycle was repeated three times, resulting in a sharp two domain (2x1) LEED pattern as measured by our Omicron model LEED system. Te was deposited from an effusion cell operated at ~ 570 K onto the Ge(001) substrate at 540K. The sample was held at ~ 540 K for 10 min after the Te-shutter was closed and the Knudsen cell power turned off.

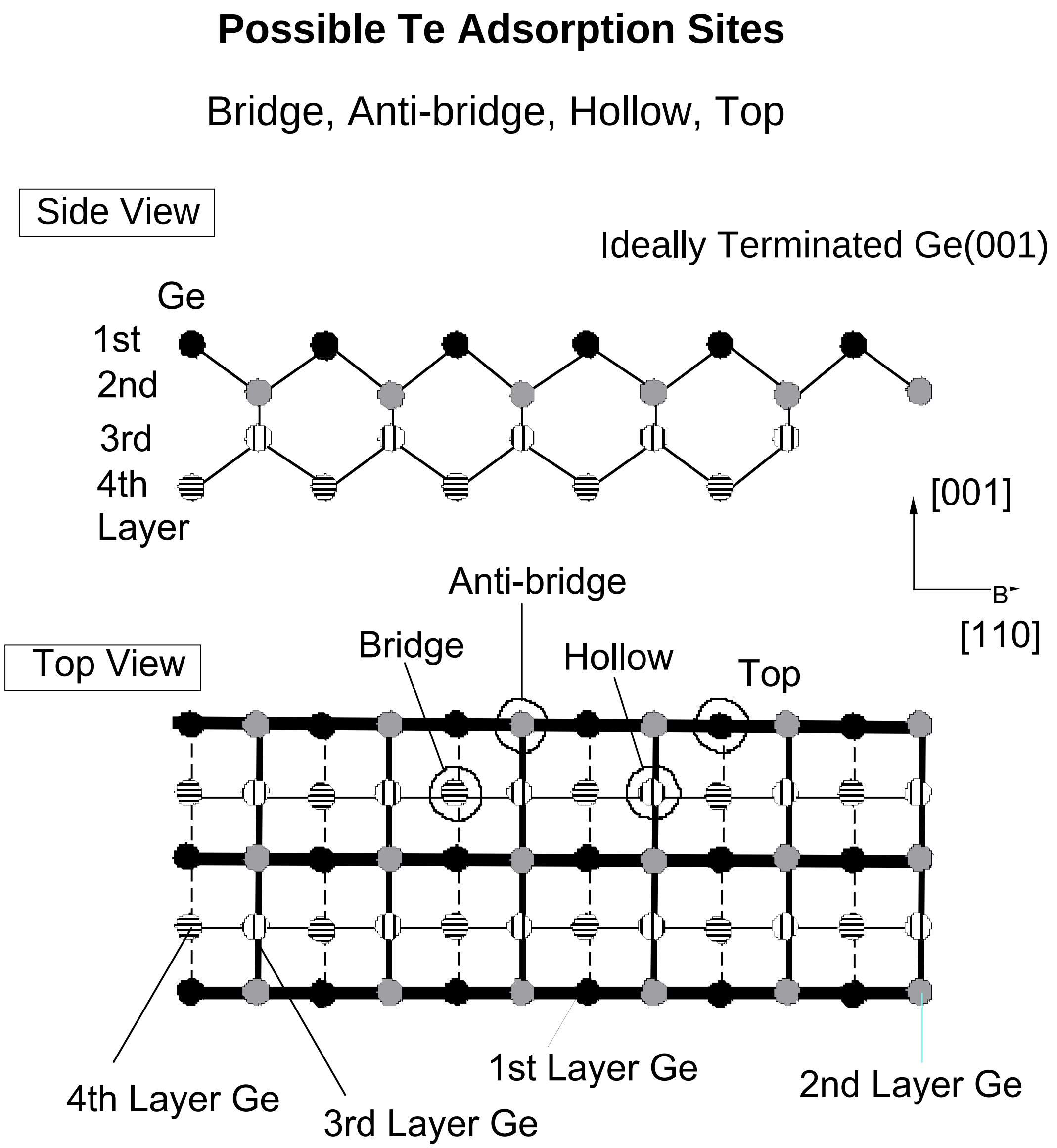

Figure 4.2 High symmetry adsorption sites for Te/Ge(001). Bridge site, Anti-bridge site, Hollow site, and Top Site.

We observed a 1 x 1 LEED pattern with streaks between the 00 and 01 spots. To remove any loosely bound Te on the surface, we heated the sample for twenty minutes at 690 K. This process produced a lower LEED background intensity but the pattern still had strong streaks (Figure 4.3), which indicates that the surface had 1x1 long-range order but locally disordered.

The CTR experiment was carried out using 18 keV undulator third harmonic x-rays passing through a double crystal high heat load Si (111) monochromator. Horizontal focusing mirrors were also used to focus the beam and reject higher order harmonics from the Si(111) monochromator. The incident beam was 1.2 mm in the vertical and 0.6 mm in the horizontal direction. Two slits were placed on the scattering detector arm with apertures of 1 mm in the vertical and 2 mm in the horizontal resulting in an angular resolution of 1.7 mrad and 0.85 mrad respectively in the vertical and horizontal directions. Three CTR scans were recorded normal to the surface at a fixed grazing incidence angle of 0.5^o. The critical angle for 18 keV x-rays reflecting from a Ge mirror surface is $\alpha_c = 0.05^0$. The data were collected by taking rocking scans at each point along the truncation rods. For each scan the background was subtracted and the intensity was fit to a Lorentzian. The integrated intensity was then corrected for the Lorentz-polarization factor, and geometrical factor [58] to arrive at $| F_{obs}|$ which is the measured modulus of the structure factor.

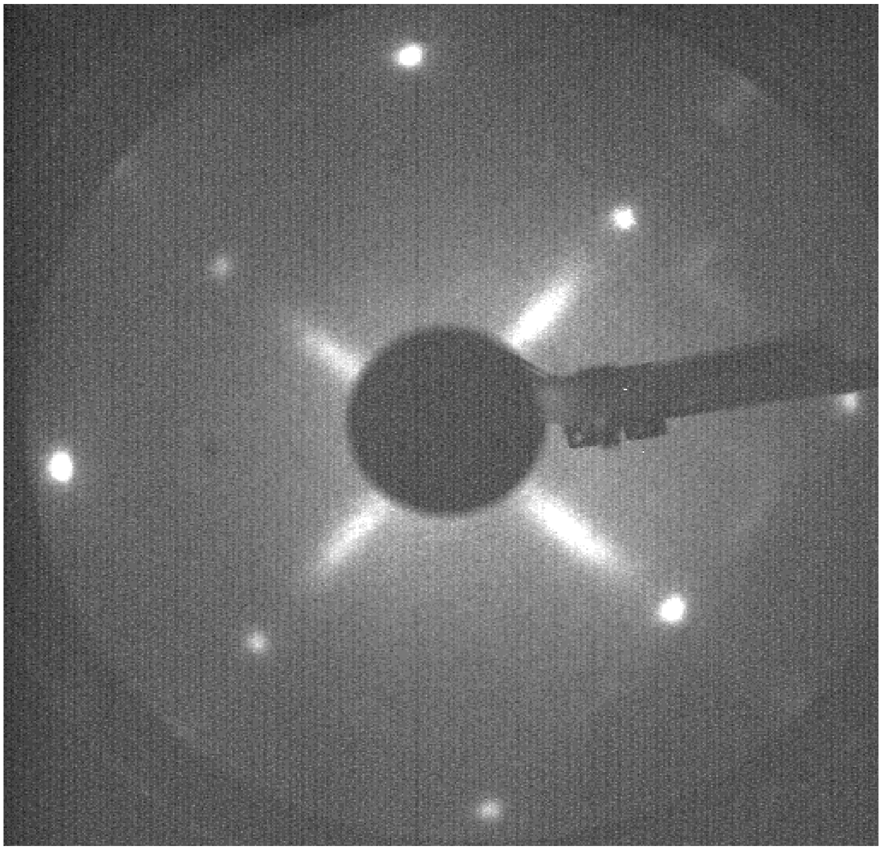

Figure 4.3 LEED pattern (35eV) observed from the Te-terminated Ge (001) surface

For an ideally terminated Ge(001) surface, it is conventional to use a tetragonal surface until cell which is related in direct space to the conventional cubic unit cell (denoted with subscript c) of the bulk; a = [100] = 1/2[110]$_c$, b = [010] = 1/2[-110]$_c$, c = [001] = [001]$_c$. The cubic coordinates are in units of the germanium lattice constant (5.658 Å). For the ideally terminated Ge(001) surface, there are two surface domains (terraces) separated by a height difference of one atomic layer; the two Ge dangling bonds are directed along the [101] and [-1 0 1] on surface domain A and along the [011] and [0-11] on surface domain B. The Te adsorption site is located in different positions with respect to the bulk lattice for the two different surface domains. The difference in coordinates will affect the phases of the scattered waves which was taken into account in the simulations. Figure 4.2 displays the different adsorption sites considered in this study.

The analysis of the data was done in two steps. The first goal was to identify the adsorption site of the Te adatoms from comparing the measured structure factor $|F_{obs}|$. to model-based calculated structure factors $|F_{cal}|$. The only physical variable at this stage of the analysis is a roughness contribution, F_r [90]which is expressed as:

$$F_r = (1-\beta)/[1+\beta^2 - 2\cos\{2\pi(L-N_B)/N_L\}]^{1/2} \tag{4.1}$$

where ß is expressed in terms of the rms roughness σ_r as :

$$\beta = [-c/n + \{(c/n)^2 + 4\sigma_r^2\}^{1/2}]^2 / 4\sigma_r^2 \quad , \tag{4.2}$$

and n (=4) is the number of Ge atomic layers in the unit cell. For the 1 0 *L*, 1 1 *L*, and 3 0 *L*, values of N_B are set to 1, 2, and 1 and those of N_L are 2, 4 , and 2 respectively. c in this equation is the out-of-plane lattice constant of the Ge substrate. At this stage in the analysis the Te vertical position was fixed at the position obtained from the XSW measurement. Other fixed parameters included Te coverage (0.74 ML) as determined by Rutherford backscattering spectroscopy (RBS) and rms vibrational amplitudes of Te and Ge. The thermal vibrational amplitudes were approximated as being isotropic and set at $\left(\left\langle u^2 \right\rangle_{Ge}\right)^{1/2}$ = 0.10 Å. which is the value for bulk Ge, and $\left(\left\langle u^2 \right\rangle_{Te}\right)^{1/2}$ = 0.13 Å from Ref. [79]. A scale factor and roughness were varied and forced to be equivalent for all three CTR fits of a given model to the data. The best fit for each adsorption site was determined by calculating χ^2 which was defined in chapter three as:

$$\chi^2 = \frac{1}{N-P}\sum_{hk}\left(\frac{\left|Fhk^{calc}\right|^2 - \left|Fhk^{exp}\right|^2}{\sigma hk}\right)^2 \quad . \tag{4.3}$$

N is the number of the data points and *P* is the number of the fitting parameters. σ is the standard deviation for the square root of the observed integrated intensity. The χ^2 was calculated to be 2.34, 3.26, 7.05, and 11.1 for the Te bridge, hollow, top, anti-bridge site models, respectively. Thus the bridge site model (with σ_r = 2.1) was found to be the most favorable model. Figure 4.4 displays the CTR data ($|F_{obs}|$) along with the simulated $|F_{cal}|$ for each adsorption site. Following the adsorption site determination from the CTR

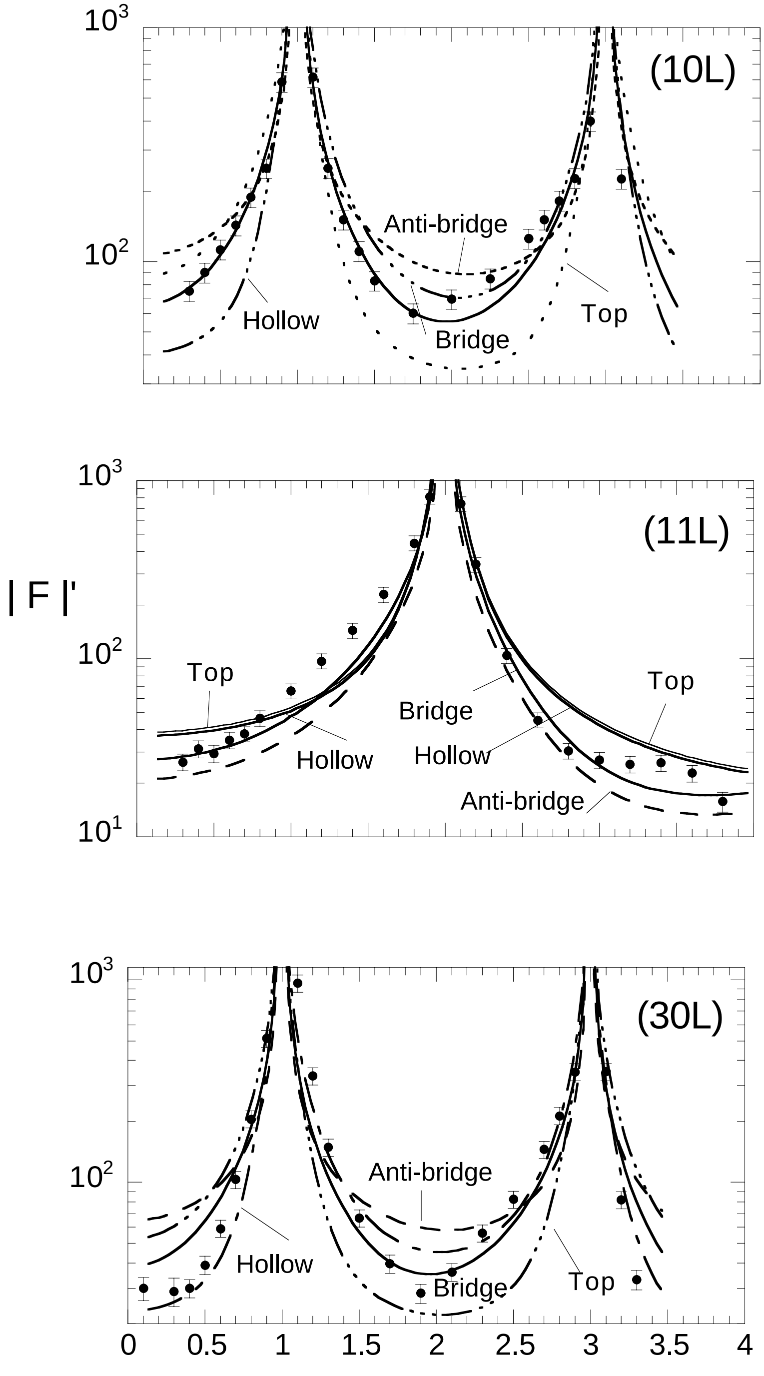

Figure 4.4 Comparison of the experimental structure factors and the calculated structure factors (relative values including roughness) based on the bridge, top, and anti-bridge site models.

measurement, it is possible to suggest qualitative models from the LEED pattern analysis. The LEED pattern in Figure 4.3 has been termed a "streaky" 1x1. The streaks are along the {1,0} direction while the transverse direction is sharp. This indicates that for this surface, the direction of long range order is perpendicular to the direction of short range order. If the structure was truly 1x1, one could argue that each Te atom adsorbs on sites directly above Ge atoms. Due to the atomic size difference between Te and Ge, the saturated Te coverage should be less than 1 ML and most likely between 0.75 ML and 0.8 ML based on Te/Si(001) STM. [87] The existence of occasional missing Te rows can account for the size difference between Te and Ge. Assuming that the rows extend to lengths that are greater than the coherence length of the electron beam, this model can also account for the long and short range order implied by the LEED pattern. The aforementioned STM experiments on the ~0.75 ML Te/Si(001) system support the model for missing Te rows. They report that the missing rows have a periodicity between 5 and 8 and that the Te atoms expand into the missing row trenches which are occupied by Si dimers. The peaking of the LEED intensity in Figure 4.3 at the half-order position supports the model with Ge dimers in the trenches. Using first-principles total energy calculations, Takeuchi proposed a model for the optimum surface structure of the same surface that we measured with both XSW and XRD. [78] The anti-bridge site and hollow sites were found not to be stable and it was shown that adsorption on bridge positions is more favorable than on

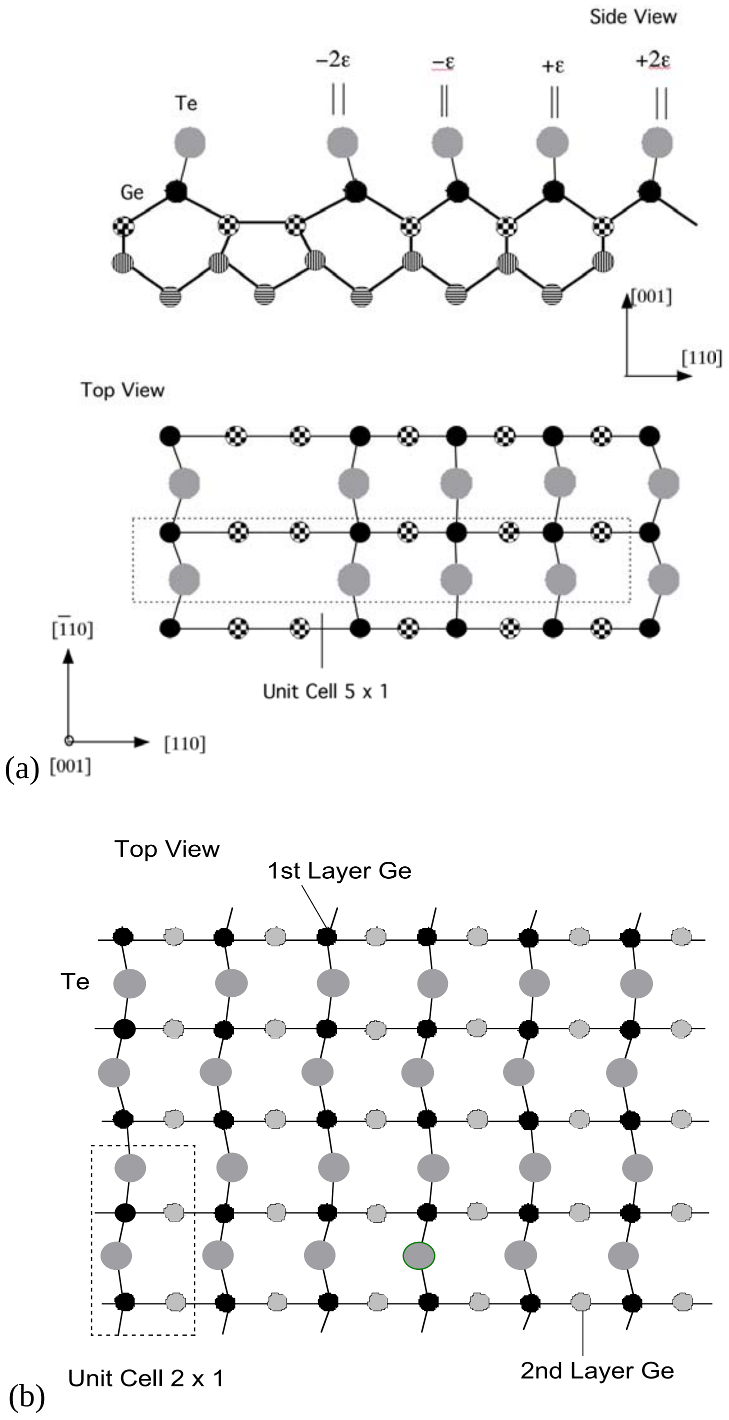

Figure 4.5 Te missing row model (a) and Te zigzag model (b).

top sites by ~1.0 eV per (1x1) unit cell. Bridge site absorption can also be rationalized from simple chemical considerations. The electronic configuration of tellurium is $(5s)^2$ $(5p)^4$. On bridge sites, each tellurium atom bonds with two surface Ge atoms and the electronic configuration of its outer shell is closed. Takeuchi further considers both a "zigzag" model and a "missing row" model as modified bridge site models. Takeuchi's missing row model has a 5 x 2 unit cell consisting of a Te layer with eight Te atoms and 5 Ge layers with Ge atoms per layer in the unit cell. The 2 x 1 zigzag model (Figure 4.5(b)) is composed of a Te layer with two Te atoms and six Ge layers with two Ge atoms per layer. Figure 4.6 shows the fitted curves based on these two models together with the experimental structure factors. As before, the free parameters used in the χ^2 fits are the surface roughness and the scale factor. The χ^2 values attained are 1.94 and 2.66 for the Te missing row and zigzag models, respectively. The CTR results favor the missing row model. Next we compared both Takeuchi's missing row model to our missing row model shown in Figure 4.5(a). The basic difference between the two models is the structure of the Ge dimer in the trench of the missing rows. In Takeuchi's model the Ge dimers that form along the missing row originate from the first Ge layer instead of the second layer. Consequently, the Ge dimer bond for this model is perpendicular to the direction of the Te displacements and the model is p(5x2). In order to refine the models, we allowed for vertical relaxations in both the Te layer and in the four topmost Ge layers. We also allowed for significant lateral displacement in the Te layer, the amount of which is predicted from Ref. [79]

and is inserted into our model as ε and 2ε where $\varepsilon = 0.058a$. The best fit CTR χ^2 is reduced to 1.49 and 1.25 for Takeuchi's and our model, respectively. Our model's fitted curves are shown in Figure. 4.6 as solid lines. In this model the displacement of the Te atomic layer along the Z direction from the bulk Ge position is +0.105 Å, where the + sign stands for atoms shifted outwards. The first through fourth Ge atomic layers are shifted vertically by 0.022, -0.025, -0.042, and – 0.014 Å, respectively from the bulk Ge positions. The Te-Ge bond length is 2.54 and 2.51 Å for the 2ε displacement and the ε displacement which are comparable to the sum (2.54 Å) of Pauling tetrahedral atomic radii. The Te positions agree to within 0.006 Å of the XSW measurement.

In summary, we have arrived at a model for the ~3/4 ML Te/Ge(001) surface. We were able to overcome the fact that our data set was minimal by using a systematic approach to eliminate competing models proceeded by a refinement of our final model. Our group's proposed missing row model is similar to a model proposed by using total energy calculations [78] and is consistent with the initial XSW study conducted earlier by our group. [79]

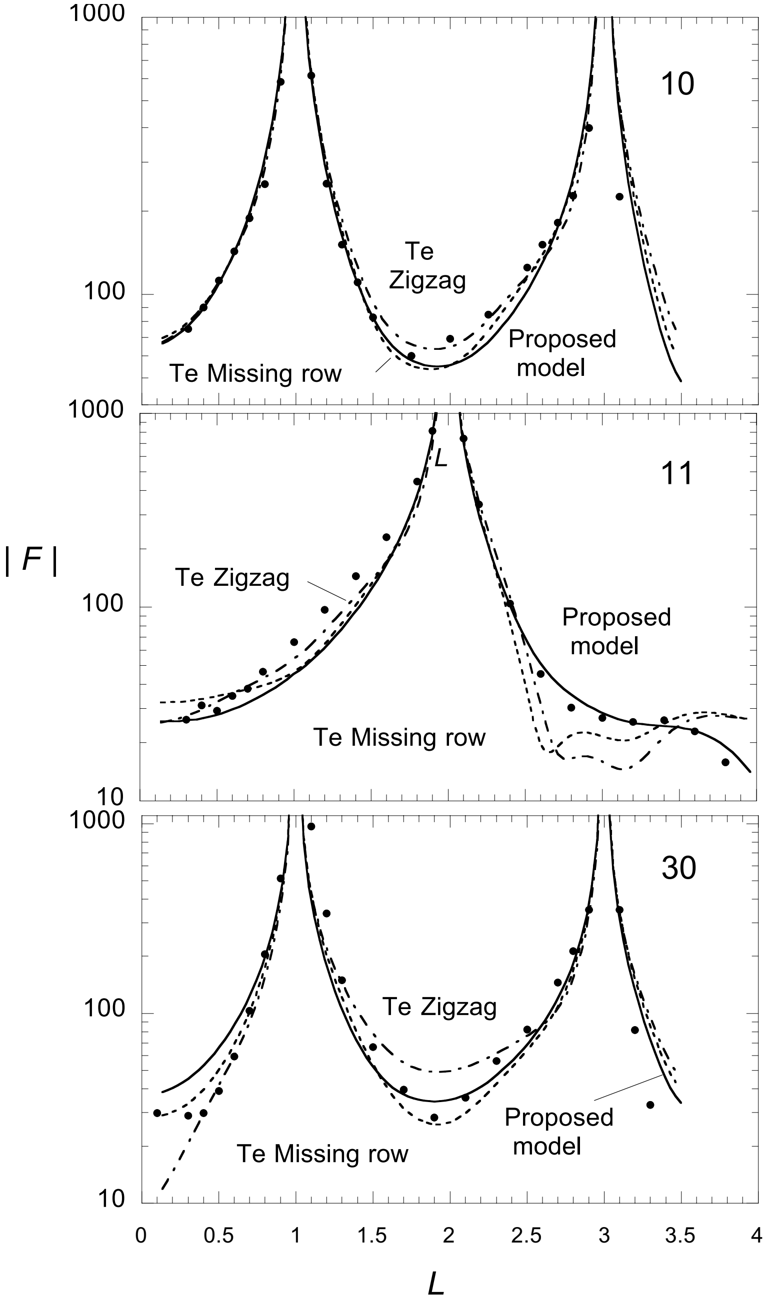

Figure 4.6 Experimental (filled circles) and calculated (line) structure factors (relative values including roughness) for the Te missing-row model (dashed line) and Te zigzag model (dot-dashed line). The refined missing-row model (solid line) includes surface relaxations for the Te and Ge atom layers.

Chapter 5 Si/Ge/Si(001) with Te as a Surfactant

5.1 Introduction

Si/Ge heterostructures continue to develop a greater presence in high frequency field effect transistors (FETs). [91] Therefore, the ability to grow thicker and higher quality epitaxial Ge films on Si(001) continues to be a motivation for engineers and scientists. Surfactant mediated epitaxy (SME) has proven to be effective for improving Ge epitaxial quality by increasing the critical thickness of Ge grown on Si and thus allowing the fabrication of abrupt interfaces in Si/Ge/Si heterostructures. Surfactants act to improve epitaxial growth by decreasing the adatom (in our case Ge) surface mobility and thereby, promote 2D epitaxial growth. A prerequisite for a surfactant in this case is to lower the surface free energy, thus, providing a driving force for the surfactant atom to site exchange with Ge adatoms as Ge is deposited. In addition to this, it is advantageous for the surfactant to have a low solubility in both Si and Ge. Most SME Ge/Si work has focused on Group V elements (As[39, 52, 92], Sb[45, 50, 93], and Bi[46, 47]), however Group IV[44, 94] and VI[49, 81] elements have also been investigated. In this work we have chosen Te to be used as the surfactant and have studied Ge films between 1 and 10 ML grown with and without a surfactant.

The growth of Ge on Si(001) proceeds layer-by-layer for the initial 2 to 3 ML. Subsequent growth results in growth front roughening, or islanding, as a means of relieving the strain set up by the 4% lattice mismatch between Si and Ge. [40, 45] By incorporating a surfactant in the growth process, one is able to grow coherently strained films well beyond 3 ML. These films have been reported to grow defect free up to ~10 ML, where upon V-shaped defects consisting of (111) planes tilted perpendicular to the direction of maximum strain begin to form.[49, 52] Supposedly, these defects relieve the misfit progressively and thus relieve strain in the film as it is grown. After ~ 50 ML, dislocations appear in the structure originating at the V-shaped defect sites. Higuchi *et al.* studied Te mediated Ge/Si(001) epitaxy with RHEED and TEM. [49, 81] They report that 550 Å thick Ge films grown with Te exhibit RHEED patterns that consist of well developed streaks. This indicates 2D layer-by-layer growth and thus, the suppression of islanding. Additionally, cross-sectional TEM [49] of these same samples show the presence of stacking faults and two-phase diffraction patterns (Si and Ge) which suggest a variation of lattice parameter throughout the Ge film.

5.2 Sample preparation

The Te/Si(001) 1x1 surface was used as the template for Ge deposition. Te, a hexavalent Group VI element, can saturate all available surface dangling bonds of the Group IV Si or Ge surface. This restores a passivated 1x1 terminated structure, rendering it suitable for surfactant behavior. The Te/Si(001) structures consists of a saturation coverage (~0.8 -1 ML) of Te atoms residing on bridge sites. [87] The ~0.8 ML Te/Ge(001) system has a similar structure. [79, 88] Occasional missing Te rows are present in both of these systems in order to accommodate the surface stress induced from the adsorption of the larger Te atom. The tendency for Te to passivate the Si and Ge (001) surfaces provides a driving force for Te to migrate to the growth surface during Ge/Si(001) heteroepitaxy. This is also confirmed by consideration of binary phase diagrams[95] where the binding energy is estimated to be stronger in Si-Ge or Ge-Ge than in Si-Te or Ge-Te. In contrast to other surfactants such as arsenic, tellurium's solubility in both Si and Ge is very low, reducing the likelihood of any background doping in Si or Ge. Additionally, Te completely desorbs from Ge(001) at a moderate temperature (450^{0}C), making it relatively easy to remove the surfactant after growth.

The set of Si/Ge/Si(001) heterolayer structures were grown by molecular beam epitaxy in a UHV system with a base pressure lower than 1x10^{-10} Torr. The Si substrates, which were 10 mm x 10 mm in area and 3 mm thick, were cleaned by the Shiraki method [96] and out-gassed for at least twelve hours at 650^{o}C. The samples were then flash annealed several times via indirect heating to 850^{o}C until a sharp 2-domain 2x1 LEED pattern was observed. Sample cleanliness was confirmed by Auger electron spectroscopy (AES) to ensure that the carbon and oxygen contamination was less than 0.01 ML. For the samples with Te, Te was deposited first onto a substrate held at 300^{o}C and then annealed to 400^{o}C for ten minutes until a 1x1 LEED pattern formed. Additionally, a Te overpressure of 10^{-6} Torr was maintained during both Ge and Si growth in order to compensate for possible Te desorption. Ge was evaporated from a Knudsen cell at a rate of 0.1ML/min with the substrate held at 410^{o}C. Continuing at 410 ^{o}C, the Si cap was deposited from an e-beam evaporator operating at

110 W with a corresponding growth rate of 1 ML/min. The Ge coverage of each sample, which ranged from 1 to 10 ML was verified by comparing its x-ray fluorescence signal to that of an ion-implanted standard. The Si cap thickness and interface roughness were determined by low-angle x-ray reflectivity. LEED and AES measurements were taken after each step in the sample preparation process. Figure 5.1 is an AES scan of Te/ Ge/ Si(001) after 7.4 ML of Ge deposited on Si(001) with Te. Figure 5.2 is a series of LEED patterns for the growth surface as different steps in the process. Figure 5.2 (a) is the clean Si(001), two-domain, 2x1 reconstruction and 5.2 (b) is a 1 ML Ge/ Si(001) 2 x n pattern. Figures 5.2 (c) and (d) are LEED patterns of the same 7.4 ML Ge sample, (c) after Ge deposition and (d) after Si cap deposition. The 1x1 patterns for figure 5.2(c) and 5.2(d) are fairly sharp with a low background. This indicates that the sample surface is 2D in nature and of high crystalline quality.

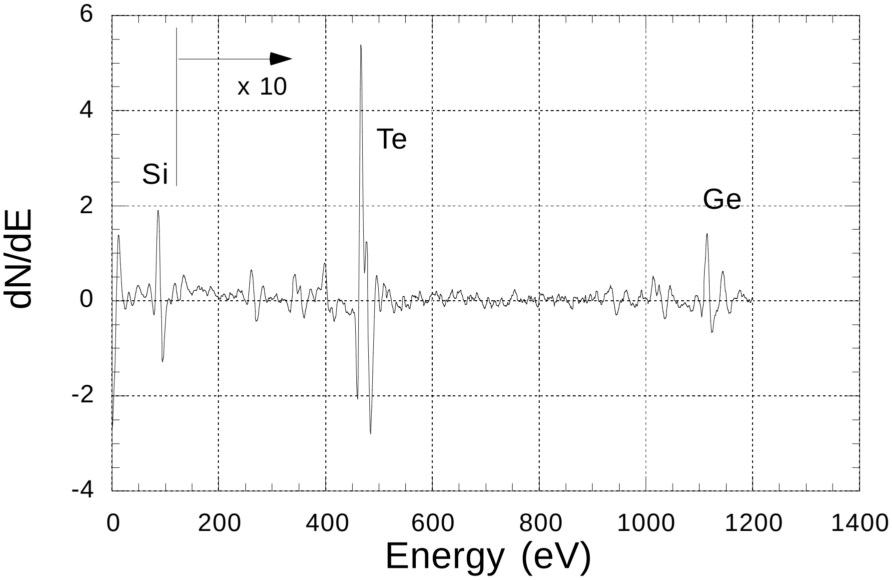

Figure 5.1 Auger electron spectroscopy scan of 1 ML Te / 7.4 ML Ge / Si(001) surface.

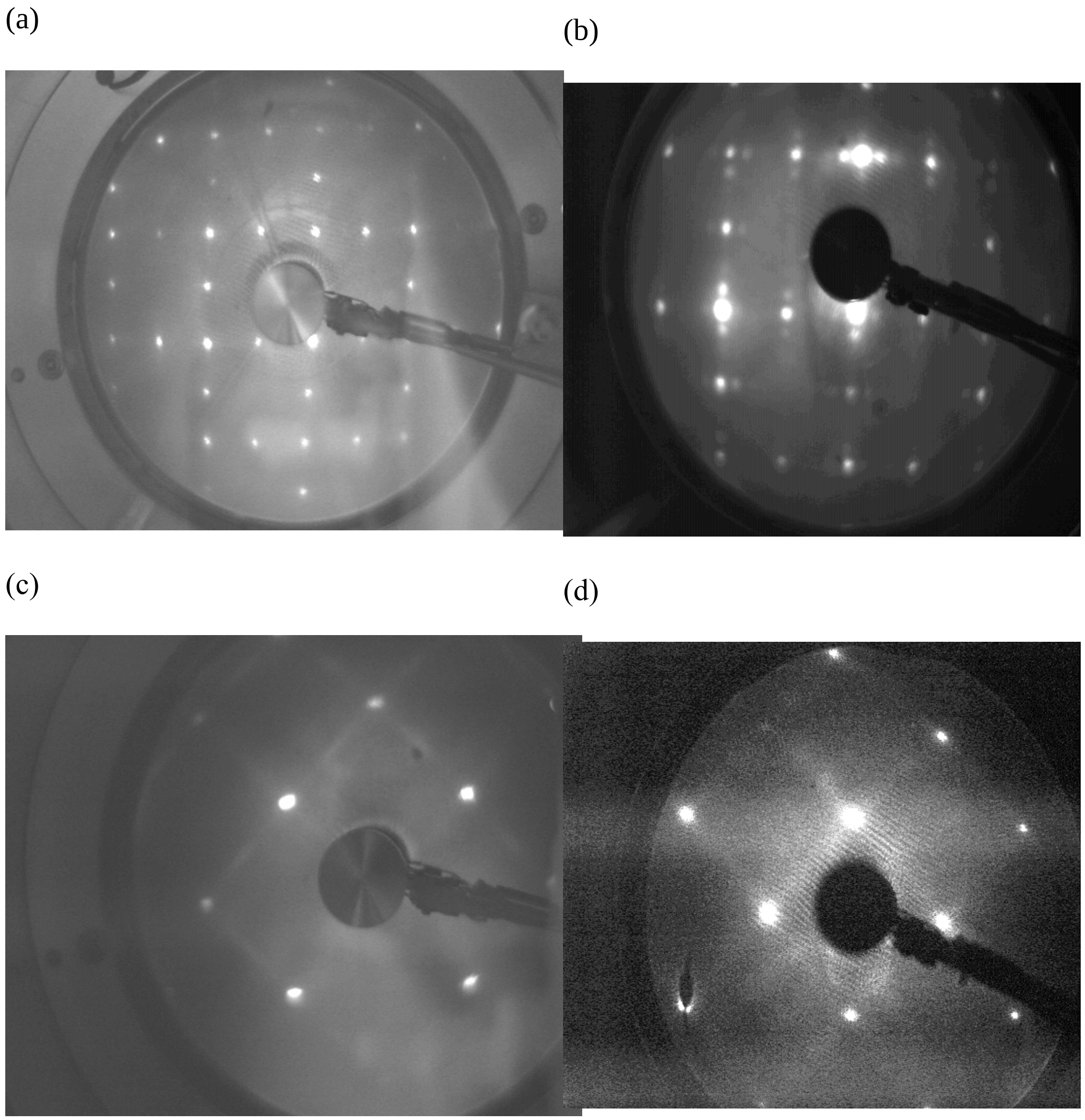

Figure 5.2 LEED patterns of growth surface. (a) Si (2x1), (b) 1ML Ge/Si(001) (2 x n) (c) 1ML Te/ 7.4 ML Ge/Si(001) “streaky” (1x1) (d) 1 ML Te/150 Å Si/7.4 ML Ge/Si(001) (1x1) with high background.

5.3 X-ray measurements

The structural characteristics of buried interfaces are important to understand for optimizing growth parameters for heteroepitaxy, as well as predicting device performance in technological applications. Quantitative characterization of buried ultra-thin heterostructures with monolayer thicknesses is a difficult task. Most standard characterization tools are excluded either due to screening effects of a capping layer or lack of resolution. Other techniques have the drawback of requiring the destruction of the sample for measurement. X-ray techniques using x-rays generated from high intensity sources offer the unique chance of non-destructive, high-resolution measurements. Our studies have focused on the initial growth (< 20 Å) of Ge on Si(001) grown with a Si capping layer. The samples were studied using a variety of techniques, namely, grazing incidence X-ray reflectivity (GIXR) crystal truncation rods (CTR), grazing incidence diffraction (GIXD) and x-ray standing waves (XSW). The combination of these techniques allows one to comprehensively characterize the epitaxial quality of very thin buried layers. The GIXR and CTR measurements are very sensitive to film thickness and interface quality. The GIXD measurements are able to probe the in-plane structure of our samples with a large degree of depth control. X-ray standing waves are able to determine the registry of Ge adatoms with respect to the Si(001) bulk substrate lattice as well as determine the degree of order of the epitaxial layers both in and out-of-plane.

5.3.1 Specular reflectivity measurements

Specular reflectivity performed at low angles provides a very simple but exceedingly effective way to obtain a large amount of information. One can determine information such as layer thickness, thickness fluctuations, and interface roughness. At low angles, scattering can be understood as electromagnetic radiation reflecting from the surface of a homogeneous dielectric medium. Because of the small momentum transfer, $q_z=(4\pi/\lambda)/\sin(\theta)$, long length scales are probed and the scattering is insensitive to crystallinity of thin films.

From Chapter 3 it was shown that the polarizability of matter for x-rays can be expressed as the following:

$$\chi_n(\mathbf{r}) = \frac{-\rho(r) r_e \lambda^2}{\pi}, \tag{5.1}$$

where r_e is the classical electron radius and ρ (r) is the electron density. Despite the fact that χ_a is very small, (Chapter 3) refraction effects become significant at low angles since,

$$\sin^2(\theta) = \sin^2(\theta') - \chi, \tag{5.2}$$

where θ’ is the internal angle due to refraction . Furthermore, total external reflection will occur below the critical angle, $\theta_c = \sqrt{-\chi_n}$. From Maxwell’s equations, one can obtain the Fresnel coefficients [97] which describe the transmission and reflection at a single dielectric interface. The Fresnel reflectivity is given as,

$$R_F = \left| \frac{Q_z - Q_z'}{Q_z + Q_z'} \right|^2 , \tag{5.3}$$

where Q_z' is the momentum transfer inside the dielectric medium. As shown by the solid curve in figure 5.3 when $Q < Q_c = \frac{4\pi}{\lambda}\theta_c$ total reflection, (R_F=1), occurs and far from Q_c, $R_F \sim \left(\frac{Q_c}{2Q} \right)^4$. The reflectivity calculated according to Maxwell's equations (often called "dynamical scattering") is rigorously correct. However, when more complex density profiles are desired, this method may be tedious. In the limit of weak scattering, a kinematical calculation can be used which is derived from the Born approximation (single scattering) and gives the specular reflectivity [98]:

$$R(Q_z) = \frac{P(\theta)\left(\frac{Q_c}{2} \right)^4}{{Q_z}^2 \rho_o^2} \left| \int \rho(z) e^{iQ_z z} dz \right|^2 , \tag{5.4}$$

where $P(\theta)$ is the polarization factor ρ_o is the average electron density. For an ideally sharp interface, the integral gives ρ_o/Q_Z and the kinematic calculation, shown by the dashed curve in Figure 5.3 approaches R_F at large Q. As can this figure demonstrates, the validity of this approximation is good as long as Q is sufficiently far from Q_c, or equivalently, the reflectivity is not too large.

We performed x-ray reflectivity measurements on our samples using our "in-house" x-ray reflectometer setup. The setup consists an 18kW Rotating anode x-ray generator with a copper target emitting x-rays in a line source geometry. More details about this set-up can be found in Appendix I. Our 10mm x 10mm x 3 mm thick sample was mounted on a two circle Huber diffractometer and the incident beam was set at 10mm high and 0.10 mm wide in order to minimize the over-subtending of sample by the x-ray beam. Two slits were used in front of the detector to decrease the background level. They were placed 50 mm apart and were each 0.2 mm wide and 10 mm high. The straight through beam was measured to be 6x10^6 counts per second.

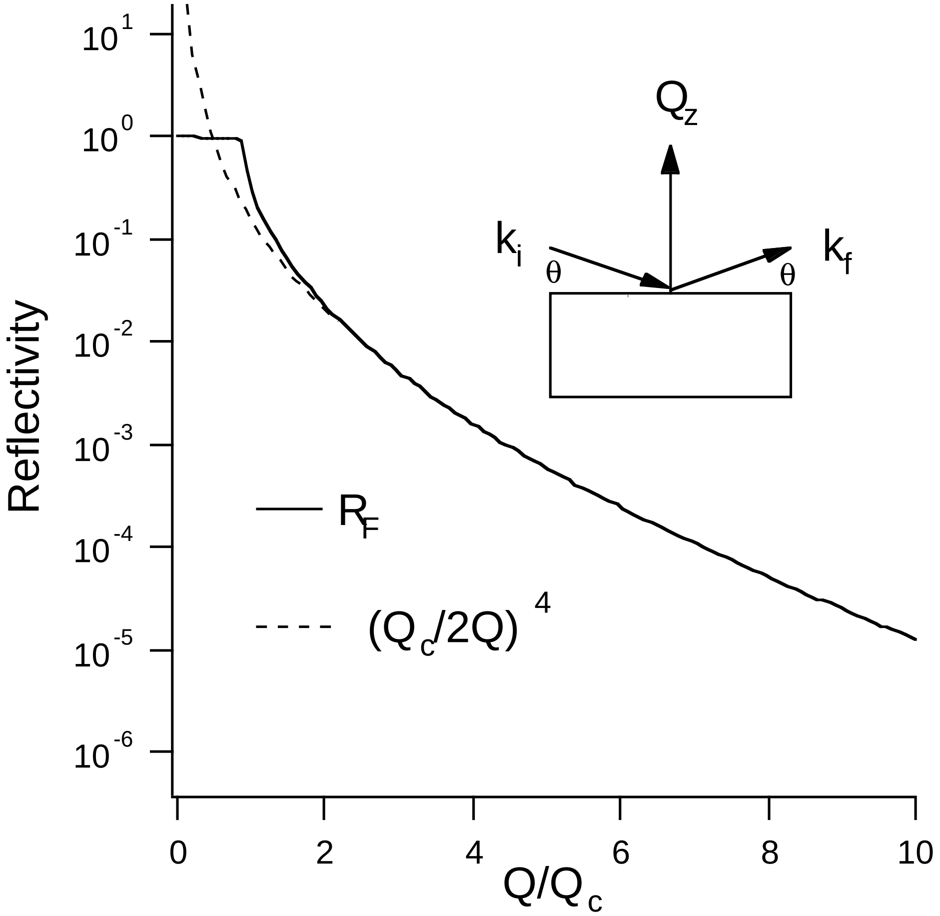

Figure 5.3 X-ray reflectivity simulation using dynamical theory (solid line) and the kinematical approximation (dashed line).

Data were taken along the specular rod and background scans were taken on both the low angle and high angle side of the specular truncation rod. The background was averaged and subtracted from the specular data. Figure 5.4 displays data taken on three samples and the corresponding fits to the data using a form of Equation 5.4. Two samples were grown with Te as a surfactant (3.7 ML Ge and 7.4 ML Ge) and one sample (3.7 ML Ge) without Te. The reflectivities were analyzed using a four layer model (Si substrate/Ge/Si cap/Oxide). Rms roughness (σ) was incorporated for each interface as a Gaussian smearing of the interfaces. The dispersion correction ($\Delta f'$ and $\Delta f''$) of the elements in the samples were determined according to Ref. [99]. The data and the corresponding fits using Equation 5.4 are shown in Figure 5.4. It is clear qualitatively that the samples grown with surfactant display oscillations that are greater in amplitude. This is evidence that the Si/Ge interfaces are sharper for the samples with surfactant. The damping of the oscillation with increasing $|q|$ and the decrease of the average intensity of the specular reflectivity are determined by the roughness of the interfaces and the surface. Figure 5.5 displays a visual model of the electron density profile corresponding for the three samples measured. The roughnesses of the different interfaces have been incorporated to scale as error functions which correspond to the integral of a Gaussian having standard deviation equal to the roughness, σ. For the sample with no surfactant, the fitting routine resulted in a $\rho_{Ge}/\rho_{Si} = 1.8$ but the Ge/Si cap roughness of 10.88 Å and Ge/Si substrate roughness of 9.18 Å have a smearing effect, therefore, lowering the effective electron density profile. AES measurements of this sample following Si cap deposition revealed that the Ge had segregated to the surface. It is also possible that some Ge could have also diffused into the Si substrate[100]. These points will be revisited later in this chapter. Table 5.1 outlines the main characterization parameters for the three samples measured. The calculated roughness values for samples grown with Te are quite reasonable and are comparable to similar studies of buried Ge layers using Bi as a surfactant. [47] It should be mentioned that since there are four layers in the model, there are four roughnesses as well. The roughness quoted in Table 5.1 is for the interface between the Ge layer and the Si capping layer. The high roughness of the 3.7 ML sample without Te can be attributed to Ge islanding as well as intermixing with the adjacent Si layers.

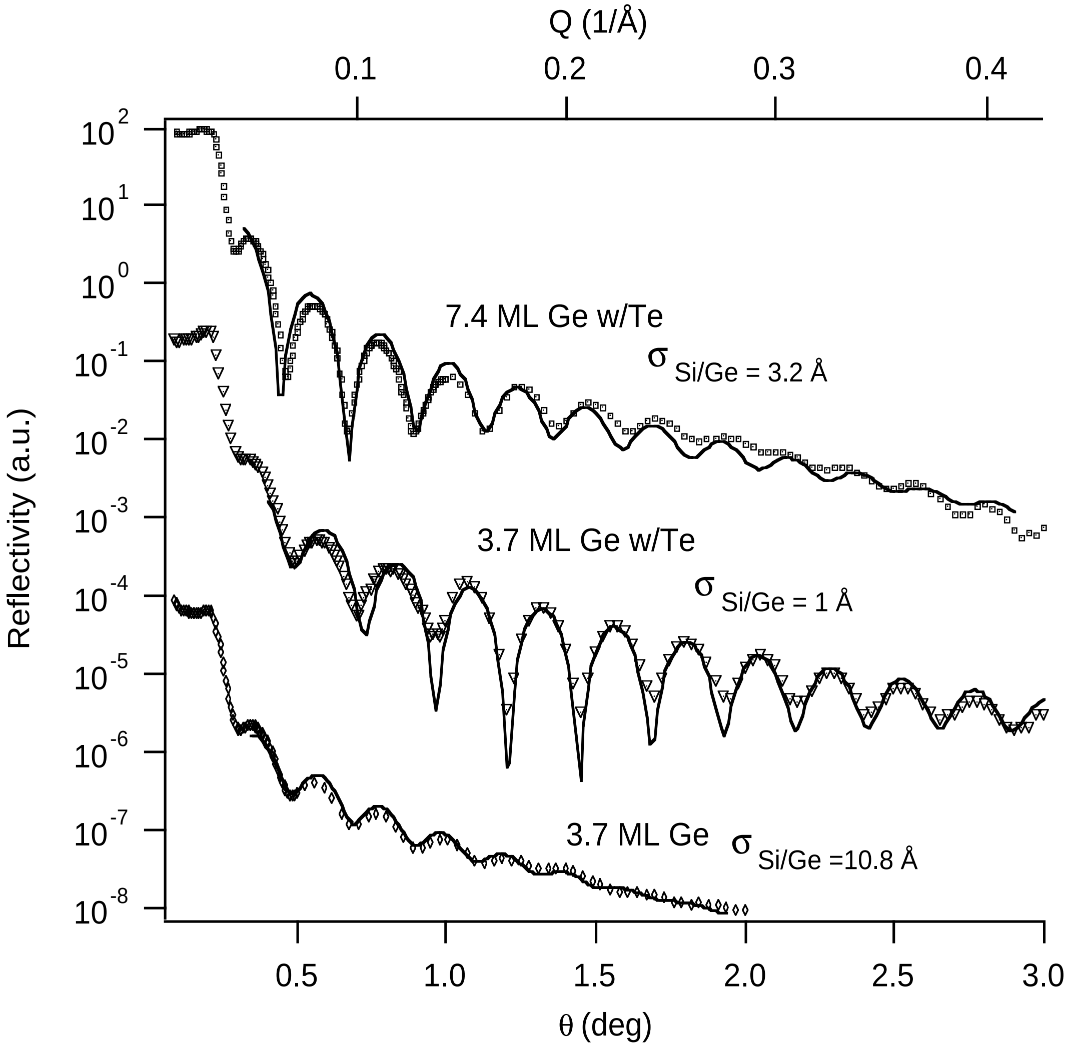

Figure 5.4 Specular reflectivity data (dashed line) and fit to kinematical theory (solid line) for Si/Ge/Si(001) heterostructures with (a) 7.4 ML Ge with Te (b) 3.4 ML Ge with Te and (c) 3.7 ML Ge without Te.

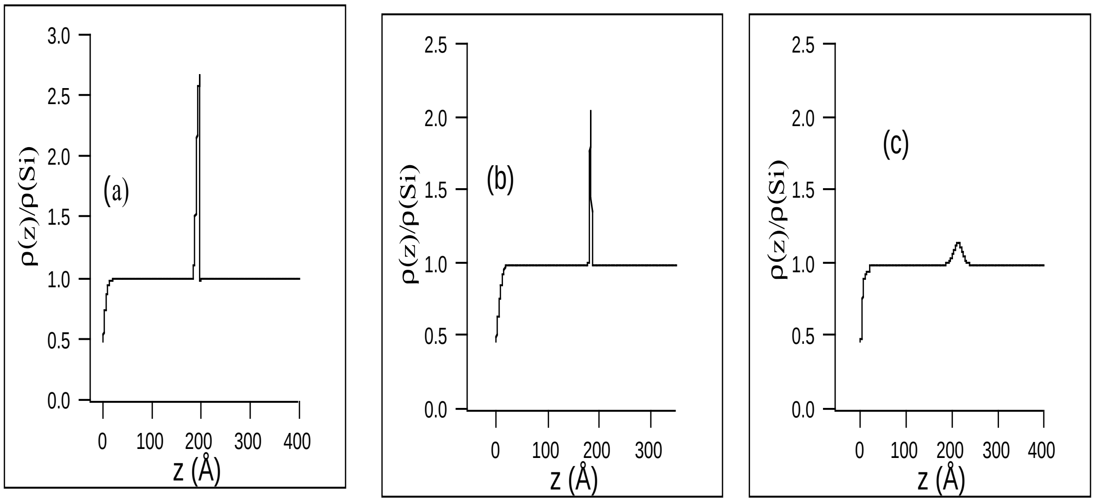

Figure 5.5 Electron Density Models for samples from figure 5.4 (a) 7.4 ML Ge with Te (b) 3.4 ML Ge with Te and (c) 3.7 ML Ge without Te.

Ge Coverage (ML)	Si cap thickness (Å)	Ge/Si cap roughness (Å)
3.7 with no Te	193 ± 1	10.88 ± 1.1
3.7 with Te	170 ± 0.5	1.1 ± 0.3
7.4 with Te	180 ± 1.2	3.32 ± 0.2

Table 5.1 Si cap thickness and Ge/Si cap interface roughness parameters for the fit to the GIXR data.

5.3.2 Crystal truncation rod measurements

Using crystal truncation rods, we have performed a study of the impact of intra-layer strain on structural properties of our ultra-thin Ge layers. The concept of the crystal truncation rod was introduced in Chapter 3 as part of the discussion on surface x-ray diffraction. The same general principles can be applied to the analysis of our thin film heterostructures. The existence of a surface or an internal interface can be understood as a disruption of the periodicity of a perfect crystal. [60] This disruption leads to a broadening of the Bragg points of the three-dimensional reciprocal lattice to Bragg rods or crystal truncation rods. For a perfect crystal with a flat surface, the intensity decays with $1/q^2$, where $q = Q - Q_{Bragg}$ denoting the reciprocal distance to the Bragg condition. For a rough surface, the intensity drops with higher powers in q. For a thin film of different scattering factor, intensity oscillations become visible along the CTR and the period of the oscillation is proportional to the reciprocal thickness of the film. The presence of interface roughness leads to a reduction of the CTR intensity and a damping of the amplitude of the oscillation with increasing $|q|$.

Bahr *et al.* have successfully used this technique on buried Ge films by scanning in the vicinity of the(004) Bragg peak of Si.[101] Their study was performed on Ge films grown between 1 and 6 ML on Si(001) with a Si capping layer They obtained decent fits using kinematical theory for Ge thickness of 1.2 ML and 2 ML where the interfacial roughnesses for the Ge and Silicon layers were between 2-3 angstroms. The samples were determined to be strained, i.e. out-of-plane lattice constant greater than that of Si, however, they were found to be strained by an amount less than predicted by elasticity theory for a pure Ge layer. This point is a bit ambiguous since they determined the Ge concentration in the epitaxial layer to be less than 65% due to intermixing between Ge epilayer and Si epitaxial layer during growth. Interdiffusion between buried Ge layers and epitaxial Si capping layers has been well documented [102, 103]. In another study, Falta *et. al.* performed the same CTR measurement on a 1 ML Ge layer, however, using Sb as a surfactant during growth. [104] On this sample the Ge layer roughness reduced from 2.7 Å to 1.6 Å and the Ge concentration in the buried layer increased from 40% to 73%. This measurement demonstrated the effectiveness of Sb as a surfactant.

In distinction to the case of a uniform film of different scattering factor, the CTR is asymmetric with respect the Bragg condition. For the case of an epilayer with a d-spacing larger than the bulk, the oscillation is much more pronounced at smaller Q values and vice versa for smaller d-spacings. However, the exact shape strongly depends on the lattice constant and scattering factor of the buried layer. The CTR intensity has been calculated following an algorithm derived within the kinematical theory following the formalism of Robinson et. al. [105]:

$$I(Q) = c\left| \begin{array}{l} e^{-q^2\sigma_{cap}^2} f_{Si}(Q)\dfrac{1-e^{iQa_{cap}N_{cap}}}{1-e^{iQa_{cap}}} + f_{Ge}(Q)e^{-q^2\sigma_{Ge}^2} e^{iQa_{cap}N_{cap}}\dfrac{1-e^{iQa_{Ge}N_{Ge}}}{1-e^{iQa_{Ge}}} + \\ e^{-q^2\sigma_{Si}^2} f_{Si}(Q)\dfrac{e^{iQ(a_{cap}N_{cap}+a_{Ge}N_{Ge}+a_{Ge}-a_{Si})}}{1-e^{iQa_{Si}}} \end{array} \right|^2 \tag{5.5}$$

Here $f_{si}(Q)$ and $f_{Ge}(Q)$ denote the Si and Ge form factors, respectively, calculated using the routines of Brennan and Cowan. [99] The form factors include the temperature dependent Debye-Waller factor. $Q = \frac{4\pi\sin(\theta)}{\lambda}$ is the wave vector transfer normal to the surface and $q = Q - G_H$ describes the reciprocal distance from the Bragg reflection. The number of lattice planes of the top Si layer and the Ge layer are denoted N_{cap} and N_{Ge}, respectively. a_{top}, a_{Ge} and a_{Si} are the lattice spacings for the top layer, the Ge layer, and the Si bulk, respectively. The roughness, σ, of the layers is indexed correspondingly to σ_{cap}, σ_{Ge} and σ_{Si}. The three terms in the equation pertain to the structure factor of each layer in the samples. The origin is set at the Si capping layer (top layer) and the bottom to layers are phase shifted by $e^{iQa_xN_x}$ which includes information regarding the strain in the Ge layer and Si capping layer. It should be noted that the information obtained in the CTR measurement has important similarities and differences from the GIXR measurement. Both techniques are very sensitive to interface quality, however, the GIXR measurement is insensitive to crystallinity whereas the CTR measurement is directly related to the interference effect between the structure factor of the different layers.

The CTR measurements were taken using an “in-house” four-circle diffractometer with x-rays generated from a 12 kW rotating anode with copper target. The x-ray source was point focused at the sample and a curved graphite monochromator was used to select copper kα x-rays. The sample was far enough from the source that the Kα_1 line could be separated from Kα_2, therefore improving the resolution. Thus, the ultimate resolution was determined by the mosaic spread of the graphite monochromator and the source divergence. The angular divergence of this setup was measured to be 0.05^0. The incident beam was defined to be 10 mm x 10 mm the guard slit and detector slit were approximately 1.5 mm. The data were taken by performing rocking scans at each Q value. Each rocking scan spectrum was fit to a Gaussian with parabolic background. The integrated intensity at each point was corrected for the Lorentz factor. Geometrical corrections were not necessary since the entire x-ray beam was hitting the sample for all Q values. The data and corresponding fits to the data are included in figure 5.6 The two samples grown without surfactant show distinct oscillations from Q = - 0.5 to Q = + 0.1 (relative to the 004 Bragg Peak). The oscillation is determined by the scattering factor of the Ge layer and the Ge concentration in the buried layer. The damping of the oscillation with increasing |q| and the decrease of the average intensity of the CTR are determined by the roughness of the interfaces and the surface. Figure 5.6 shows the crystal truncation rods for the same three MBE grown Ge layers mentioned in the previous section. The period of the oscillation is given by the thickness of the Si top layer and the amplitude of the oscillations is determined by the jump of the average lattice constant at the Si/Ge interface. The sample grown without Te was not fit since the CTR does not contain enough features to uniquely determine any relevant parameters. For the samples with Te, the intensity on the high Q side of the Bragg peak dropped off significantly and the corresponding statistics became poor. In order to be able to collect meaningful data in this region, x-ray sources such as synchrotron radiation would be necessary. This asymmetry around the Bragg peak is due to the fact that Ge layer spacing is greater than that of Si. If Ge layer spacing was less than that of Si, the intensity on low Q side of the Bragg peak would be lowered as compared to the high Q side. The relevant fitting parameters for the three samples are contained in Table 5.2. The thicknesses measured from CTR are slightly different than obtained from the GIXR measurement. We expected that the thickness of the Si capping layer, as measured by CTR, could be slightly different than measured by GIXR due to the fact that the Si capping might contain some defects, thus lowering the effective thickness measured by CTR. This is the case for the 3.7 ML samples where GIXR measured t_{cap} = 170 Å and CTR measured 157 Å. This is not the case for the 7.4 ML sample where the measured CTR thickness was ~ 10 Å greater than measured by GIXR. This point is not yet completely understood.

An advantage of the CTR measurement over GIXR is the enhanced sensitivity to the structure of the buried Ge layer. The CTR profiles are largely affected by both the Ge layer thickness and lattice spacing. Elasticity theory predicts the difference in lattice spacing normal to the growth surface for Ge grown epitaxially on Si to be ~7%. For the 3.7 ML and 7.4 ML sample we measured this value to be 6.8% and 6.5%, respectively.

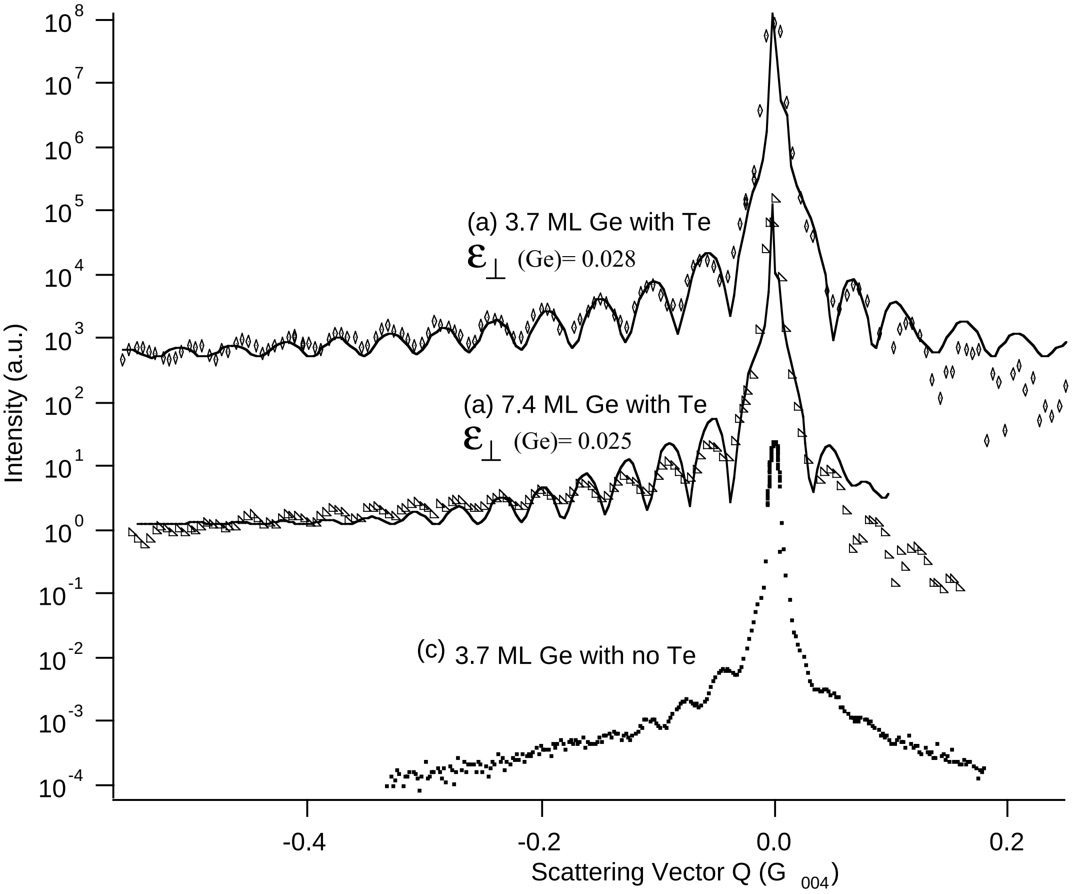

Figure 5.6 Crystal truncation rods for Si/Ge/Si(001) samples (a) 3.7 ML with Te (b) 7.4 ML with Te and (c) 3.7 ML Ge with no Te.

	3.7 ML Ge with Te	7.4 ML Ge with Te
Si cap thickness (Å)	154.3 ± 0.1	191 ± 0.1
Ge thickness (Å)	2.87 ± 0.05	11.1 ± 0.2
d_{004} mismatch $(a_{Ge}-a_{Si})/(a_{Si})$	.068 ± 0.005	.065 ± 0.005
Roughness (Ge) Å	2.9 ± 0.5	3.34 ± 0.4

Table 5.2 Relevant CTR fitting parameters for the two SME samples grown with surfactant.

5.3.3 Grazing incidence x-ray diffraction measurements

Grazing incidence x-ray diffraction (GIXD) is a complementary technique that can be used to map the strain distribution in thin films. By controlling the incidence angle of the x-ray beam upon the surface of our samples, we were able to control the depth at which the x-rays penetrated our samples and probe the in-plane strain in our samples as a function of depth. When the angle, $\alpha_{I,}$, between the incident wave vector and the interface is less than the critical angle $\alpha_c = \lambda\left(\frac{r_e\overline{\rho_e}}{\pi}\right)^{1/2}$ (λ is the wavelength, $\overline{\rho}_e$ is the mean electron density, and r_e the electron radius), a specularly reflected beam appears and the evanescent wave within the less-dense medium decays exponentially with typical depths of less than 50 Å.

The incident wave vector k_i is modified upon crossing the boundary. Its parallel components are unchanged, but its perpendicular component k becomes complex due to refraction and absorption:

$$k_{iz} = \frac{2\pi}{\lambda}\sqrt{n^2 - \cos^2\alpha_i} \quad . \tag{5.6}$$

In the case of no absorption, $\beta = 0$, k_{iz} switches from purely real to purely imaginary at the critical angle, defined by $\cos\alpha_c = n$. When the wave vector is imaginary it is called 'evanescent' because this causes the wave amplitude to decay exponentially with depth. Finite values of β $\left(0 < \beta << \left|\frac{\chi_o}{2}\right|\right)$ have the effect of softening the switching: the propagating wave at $\alpha_i > \alpha_c$ has a small imaginary component describing the normal absorption process, while for $\alpha_i < \alpha_c$ there is always a real component as well. In either situation the penetration depth Λ_I is simply related to the imaginary part of k_{iz} by:

$$\Lambda_i = \frac{1}{\mathrm{Im}(k_{iz})} \quad . \tag{5.7}$$

For small incidence angles, this characteristic depth is small and increases with angle according to Figure 5.7.

Using this technique, Williams *et al.* [106] verified that that the critical thickness for strain relaxation is between 3 and 4 ML for Ge growth on Si at 500°C. For 10 ML thick films they found that the strain in the Ge epilayer consisted of both a fully relaxed component as well as a Si-Ge alloy component. Thornton *et al.* [107] performed a similar study using Sb as a surfactant and measured the critical thickness for the onset of Ge relaxation to be ~ 11 ML and claim that even up to 55 ML the films grown with Sb are at least partially strained. Grazing incidence x-ray diffraction (GIXD) measurements were made on our samples to measure the in-plane lattice parameters for the specific purpose of identifying between the strained and relaxed Ge films. The experiment was carried out at the 5 BM-D beamline at the Advanced Photon Source on a four-circle diffractometer. Figure 5.8(a) shows in-plane H - K scans at L = 0.03 for three different samples. Each sample had a 70 Å thick Si cap. At this grazing incidence condition the scattering depth is Λ ~ 900 Å and thus the in-plane scattering is sensitive to the structure of the Si cap and Ge buried layer. For the 9 ML sample grown without a surfactant, a peak is present at H = K = 1.93. This is close to the expected H = 1.92

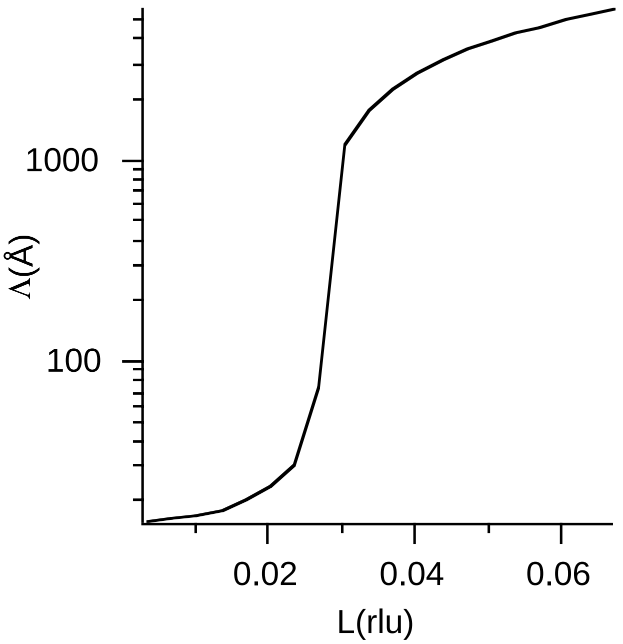

Figure 5.7 X-ray penetration depth versus reciprocal lattice vector for 10.5 KeV x-rays incident upon a Si mirror surface.

position for a pure Ge bulk lattice constant, implying that there exists relaxed Ge in the heterostructure. The 9 ML sample that was grown with Te as a surfactant shows no feature at this H = K value. This indicates that the Ge epilayer is strained with an in plane lattice constant constrained to that of Si(001). Figure 5.8 (b) contains data for the same samples in a more grazing incidence condition. For this condition the scattering depth is reduced to $\Lambda \approx 20\text{Å}$ where only the Si capping layer is being probed. The peak at H = K = 1.93 for the 9 ML sample without surfactant is again apparent in this scan ,implying that growth front roughening has created 3D structure at the Ge/Si cap interface. Equation. 5.7 is only valid for planar interfaces so the penetration depth for this sample is likely to be larger than the calculation from this equation.

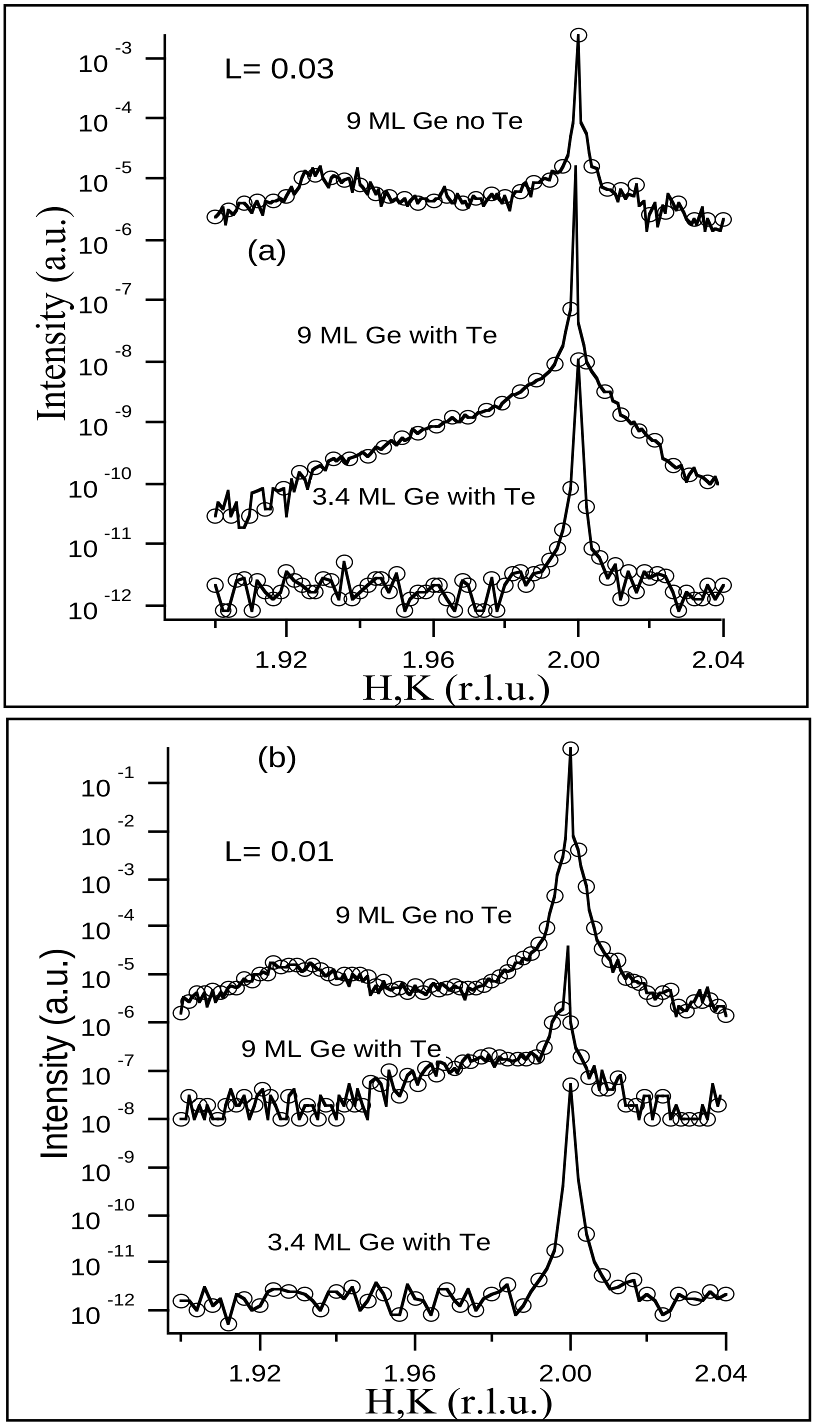

Figure 5.8 *H,K* scans through the (a) Si (2 2 L = 0.03) and (b) Si(2 2 L = 0.01) peak for samples with 9 ML Ge with Te as a surfactant, 9 ML Ge with no Te, and 3.4 ML Ge with Te as a surfactant. Lines are a guide to the eye.

5.3.4 X-ray standing wave measurements

X-ray standing waves have successfully been applied to studying buried Ge layers on Si (001). Falta *et al.* measured a coherent position of P_{004}= 1.03 and coherent fraction of F_{004} = 0.87 for 1 ML Ge buried under 100 Å of Si grown at 350°C [108]. For a 1 ML SME sample with Sb as a surfactant they reported a coherent position of P_{004} = 1.06 and coherent fraction of F_{004} = 0.97 [104]. For 1 ML of Ge buried under an 800 Å cap layer grown at 500^0C Takahasi measured P_{004} = 1.06 and F_{004} = 0.79 [109]. Rodrigues *et al.* [110] performed a detailed study of Ge buried in Si using Bi as a surfactant. His findings were that the positions of the Ge epilayer were consistent with positions predicted by elasticity theory. However, the measured coherent fractions for his samples were significantly lower than predictions from elasticity theory. To accommodate for this he incorporated a static Debye Waller factor to account for distribution of Ge positions for each successive atomic layer of Ge.

The (004) and (022) XSW scans for our study were performed at the NSLS X15A beamline. The measurements were made by monitoring the Ge Kα florescence signal while scanning in energy through the Si(004) and Si(022) rocking curves. The standing wave field is generated by dynamical Bragg diffraction from the Si single crystal substrate. As the incidence angle (or energy) is scanned through the range of the Bragg reflection, the standing-wave nodal planes move inward one-half a d_{hkl} spacing. The coherent fraction and coherent position of the Ge atoms in the film is determined by applying dynamical diffraction theory analysis to the data. A more detailed review of the XSW technique is available elsewhere. [111] The (008) XSW measurements were made at the 5-ID-C beamline of the Advanced Photon Source.

The structural parameters determined in our XSW measurement are coherent fraction (f_H) and coherent position (P_H). These were previously defined in Chapter 3 as, respectively, the amplitude and phase of the H = *hkl* Fourier component ($\mathcal{F}_H$) of the atomic distribution function, ρ(r), of all the atoms contributing to the fluorescence signal.

$$\mathcal{F}_{\mathrm{H}} = \int \rho(r) e^{2\pi i \mathbf{H}\cdot\mathbf{r}} = \mathrm{f}_{\mathrm{H}} \mathrm{e}^{2\pi i \mathrm{P}_{\mathrm{H}}} \tag{5.8}$$

The (004) XSW measurement probes the registry of the Ge atoms with respect to the Si substrate lattice along the growth direction while the (022) measurement probes a component that is sensitive to the registry both in and out-of-plane. Figure 5.9 shows a schematic of the Ge adatom position relative to the underlying (a) Si (004) and (b) Si (022) substrate diffracting planes. Figures 5.10 compares (004) XSW fluorescence fits for two of the samples with and without surfactant. Figure 5.11 is an (022) XSW measurement made with the same samples. The stronger modulation (higher coherent fraction) in Ge florescence for the sample grown with Te is characteristic of a higher degree of ordering in the epitaxy.

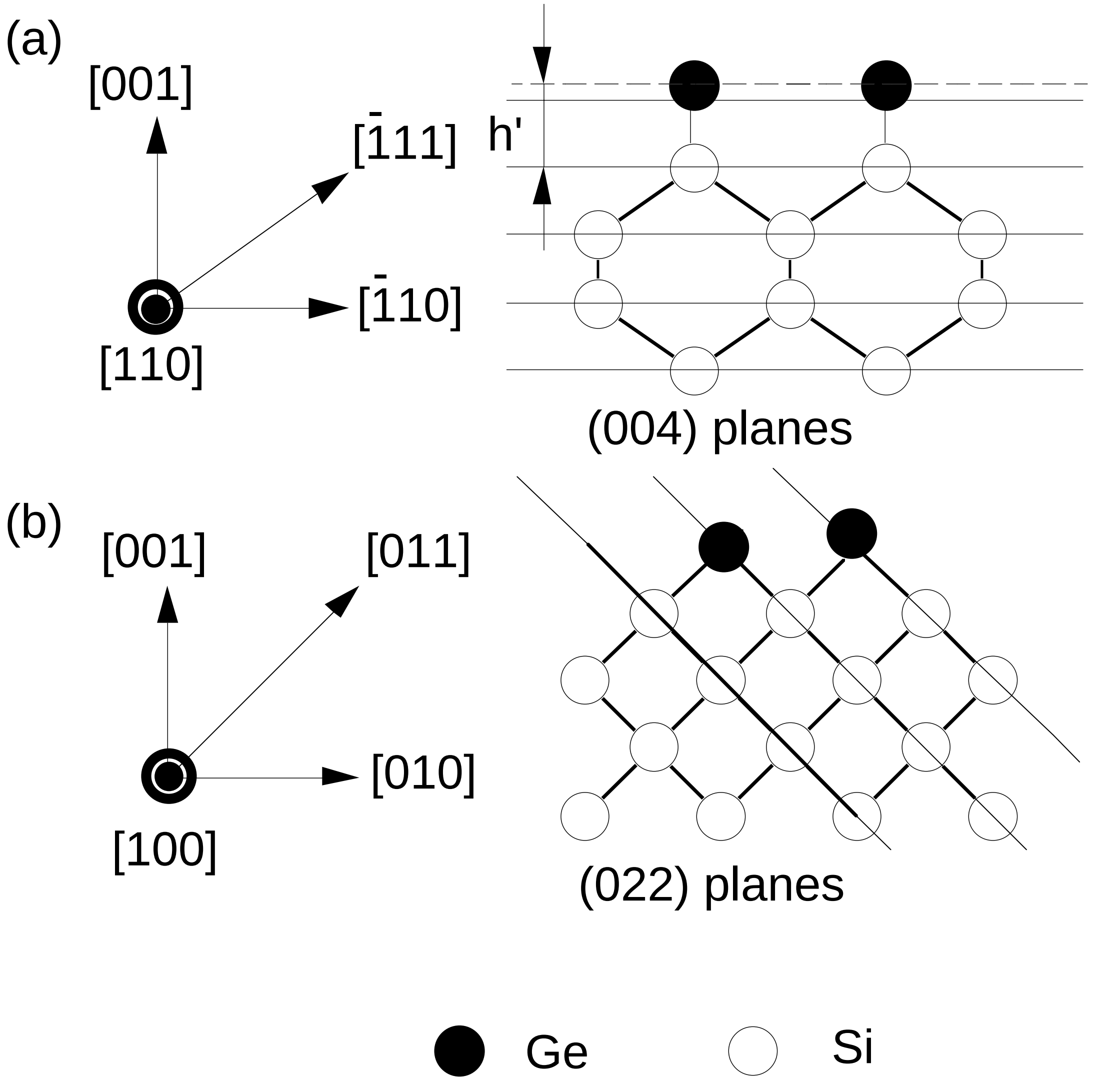

Figure 5.9 Display of the (a) (004) and (b) (022) diffracting planes for bulk Si. and the relative Ge position measured by XSW.

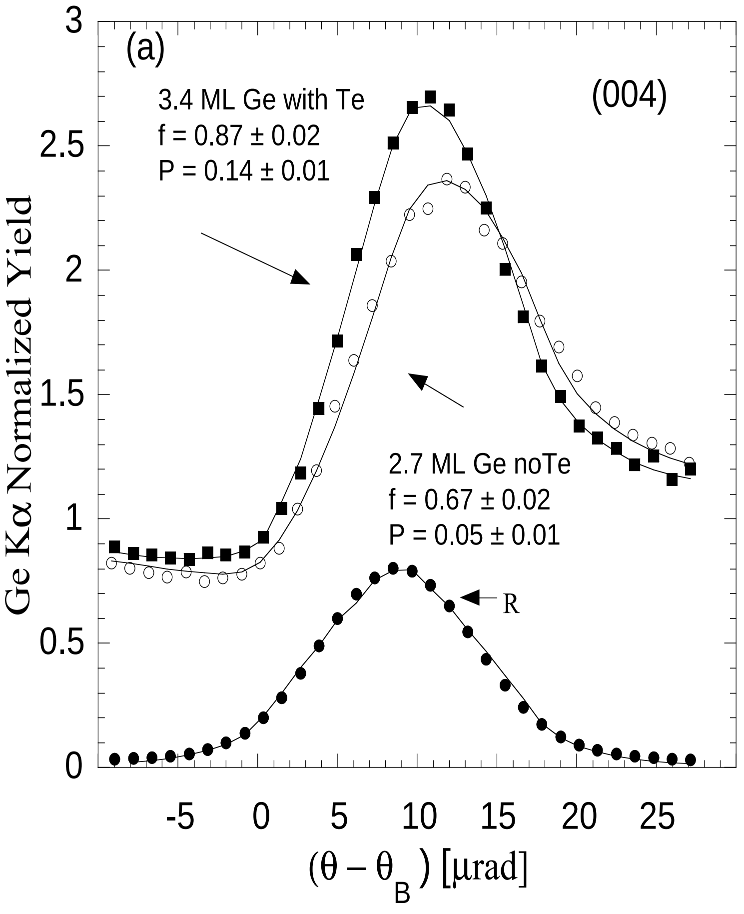

Figure 5.10 The experimental and theoretical angular dependency of the Ge Kα fluorescence yield and reflectivity collected while scanning in energy through the (004) Bragg reflection. The samples are a 3.4 Ge ML film grown with Te as a surfactant compared with a sample that is a 2.7 ML Ge film grown with no surfactant.

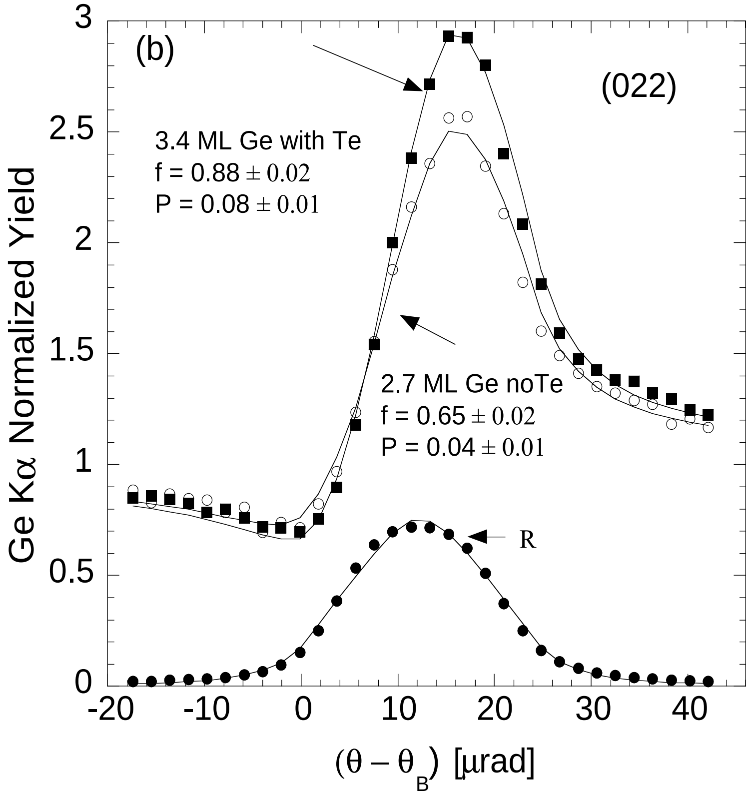

Figure 5.11 The experimental and theoretical angular dependency of the Ge Kα fluorescence yield and reflectivity collected while scanning in energy through the (022) Bragg reflection. The samples are a 3.4 Ge ML film grown with Te as a surfactant compared with a sample that is a 2.7 ML Ge film grown with no surfactant.

The bulk lattice constant of Ge is 4.2% larger than Si at room temperature. If the epitaxial layer is compressively strained in-plane to lattice match the substrate, the film will be tetragonally distorted out-of-plane. Based on elasticity theory, the strain in the [001] direction is given by:

$$\varepsilon_{\perp} = -2\frac{c_{12}}{c_{11}}\varepsilon_{\parallel} \quad , \tag{5.9}$$

where the elastic constants for Ge are $c_{11} = 12.4\times10^{10}$ N/m^2 and $c_{12} = 4.13\times10^{10}$ N/m^2. [112] Therefore, $\varepsilon_{\parallel} = -0.040$ results in a $\varepsilon_{\perp} = 0.027$. This results in an out-of-plane Ge atomic layer spacing that is 7.0% larger than the bulk Si(004) atomic layer spacing. For such an ideal coherently strained Ge film, the Hth Fourier component of the atomic distribution function would be:

$$\mathcal{F} = \frac{1}{N}\sum_{n=0}^{N-1}\exp(2\pi i(n\delta_H^F + \delta_H^I)) \quad , \tag{5.10}$$

where N is the total number of fully occupied Ge layers and δ_H^F is the fractional increase of the d-spacing of the film (d_H^F) relative to the d-spacing of the substrate (d_H^S). δ_H^I is the offset for the first epitaxial layer. We will assume that $\delta_H^I = \frac{1}{2}\delta_H^F$ based on the difference in length between Si-Ge bonds and Ge-Ge bonds. From this equation one can solve for the theoretical values for f_H and P_H:

$$f_H = C|\mathcal{F}_H|D_H = C\frac{\sin(\pi N\delta_H^F)}{N\sin(\pi\delta_H^F)}D_H \tag{5.11}$$

$$P_H = \frac{1}{2\pi}\arg(\mathcal{F}_H) = \frac{N-1}{2}\delta_H^F + \delta_H^I \quad . \tag{5.12}$$

In equation (5.11), D_H is the Debye-Waller factor and C is the fraction of atoms in expected lattice positions (ordered fraction). By combining fundamental and higher-order-Bragg reflection XSW results, it is possible to further decompose f_H into its constituent parts. [113, 114] In our case, we are able to separate out the ordered fraction (C) and the Debye-Waller factor (D_H) in Equation 5.11 by performing (004) and (008) XSW measurements on the same samples. The Debye-Waller factor can be described as follows:

$$D_H = \exp\left(-2\pi^2 \frac{\left\langle u_H^2 \right\rangle}{d_H^2}\right). \tag{5.13}$$

$\left\langle u_H^2 \right\rangle^{1/2}$ is the rms thermal vibrational amplitude of the Ge atoms. Figure 5.12 shows the (a) (004) and (b) (008) XSW measurement on the same sample. Using the XSW measured values for coherent fractions from the two measurements, we directly determine the Ge vibrational amplitude to be $<u_{hkl}^2>^{1/2} = 0.08 \pm 0.015$ Å, which is close to values for bulk Ge (0.068) and bulk Si (0.063). The measured vibrational amplitude corresponds to a D_{004} of 0.94. Assuming an isotropic Ge vibrational amplitude, this measured value of $<u_{hkl}^2>^{1/2} = 0.08$ is used to eliminate D_H as an unknown in equation 5.11.

Figure 5.13 shows the measured and predicted (004) and (022) coherent fraction and coherent position values for the samples grown with Te (the predicted values come from equations 5.11 and 5.12 with C = 1). For Ge thicknesses below 9

ML our XSW coherent fractions and coherent positions agree well with values predicted from elasticity theory for pseudomorphic growth (solid line). This is in contrast to samples grown without surfactant and for samples above 9ML in Ge coverage grown with Te. In the latter case we believe that the film begins to relax and that the introduction of defects is likely. This would lead to a reduction in coherent fraction and therefore a large error bar for the coherent position. To interpret these results for samples without surfactant, we must consider the factor for ordered fraction (C) in equation 5.11. For the case of $C = 1$, all Ge atoms would be occupying "ideal" ordered tetragonal lattice positions. "Ideal" in this interpretation would pertain to positions predicted by the simple elasticity model. The tendency for Ge to segregate and form islands as a means of stress relaxation has the effect of creating a larger distribution of Ge positions, lowering the ordered fraction. In addition, the introduction of defects such as vacancies, dislocations, or twin boundaries would lower this value as well.

Table 5.3 lists measured f and P values for samples with and without surfactant as well as the calculated values for ordered fraction (C) for the samples grown with surfactant. For the samples grown with surfactant, C is calculated from equation 5.11. In this equation, F_H is calculated assuming that the epitaxial growth follows elasticity theory and D_H and f are measured quantities. For the samples grown without surfactant the simple elasticity theory model is insufficient. For example, for the 3.7 ML sample grown without surfactant, it is expected that 3D growth will have initiated. This explains the relatively low coherent fraction for this sample ($f_{004} = 0.37$). Notice that the two non-SME samples below the critical thickness have f and P values that are significantly lower than those predicted by the ideal model in Figure 5.13. This does not imply that the films are not pseudomorphic, but rather this indicates that there is significant diffusion of Ge into the Si cap layer. This phenomenon has been well documented for Si/Ge [102, 103] as it has been observed that a certain fraction of the Ge layer diffuses into and even on top of the Si capping layer at growth temperatures between 350°C and 650°C. In fact, our AES measurements performed after deposition of the Si cap indicate significant amounts (~ 0.25 ML - 0.5 ML) of Ge on the surface. It has also been reported that Ge can diffuse into subsurface Si layers. [115] It is therefore reasonable to assume that in addition to positions in the Ge epitaxial layer, Ge is occupying substitutional positions both below the Si surface and in the Si capping layer. The Ge that segregates to the surface of the Si cap will have oxidized into an amorphous phase. It is evident that there will be a wide range of Ge positions for the samples without Te, therefore, rendering the calculation of $\mathcal{F}_H$ quite complicated.

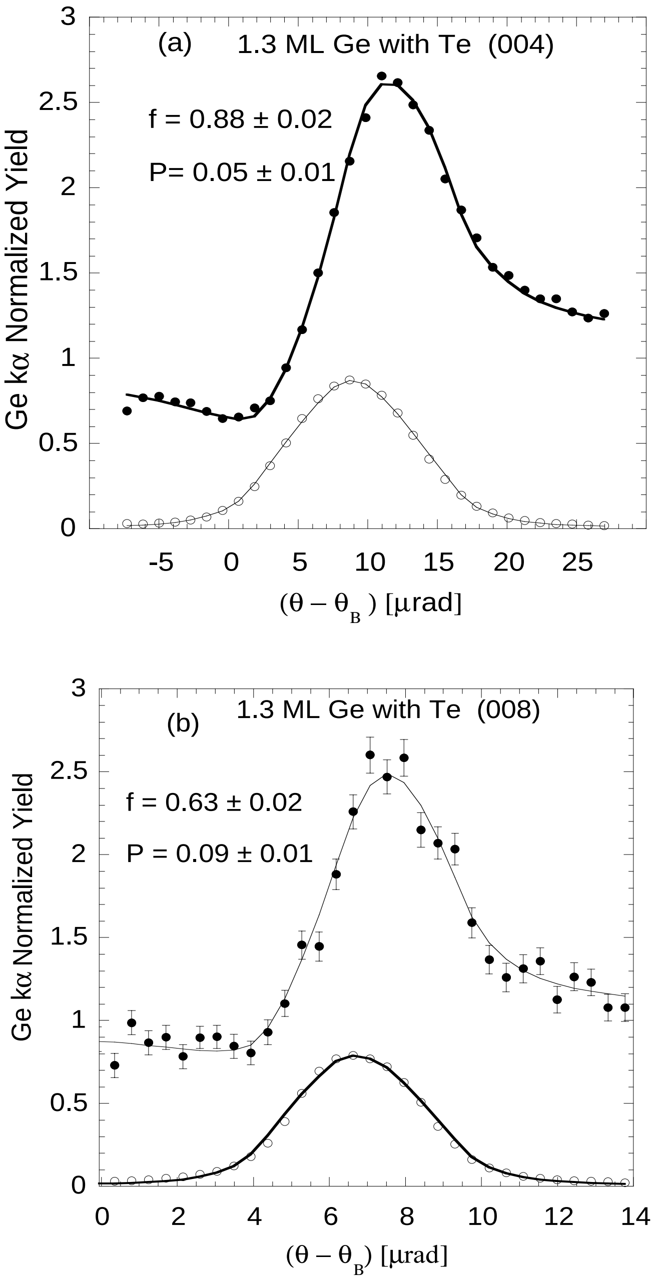

Figure 5.12 The experimental and theoretical angular dependency of the Ge Kα fluorescence yield and reflectivity collected while scanning in angle through **(a)** the Si(004) and **(b)** the Si (008) reflection. The sample is 1.3 ML Ge/Si(001) with Te as a surfactant.

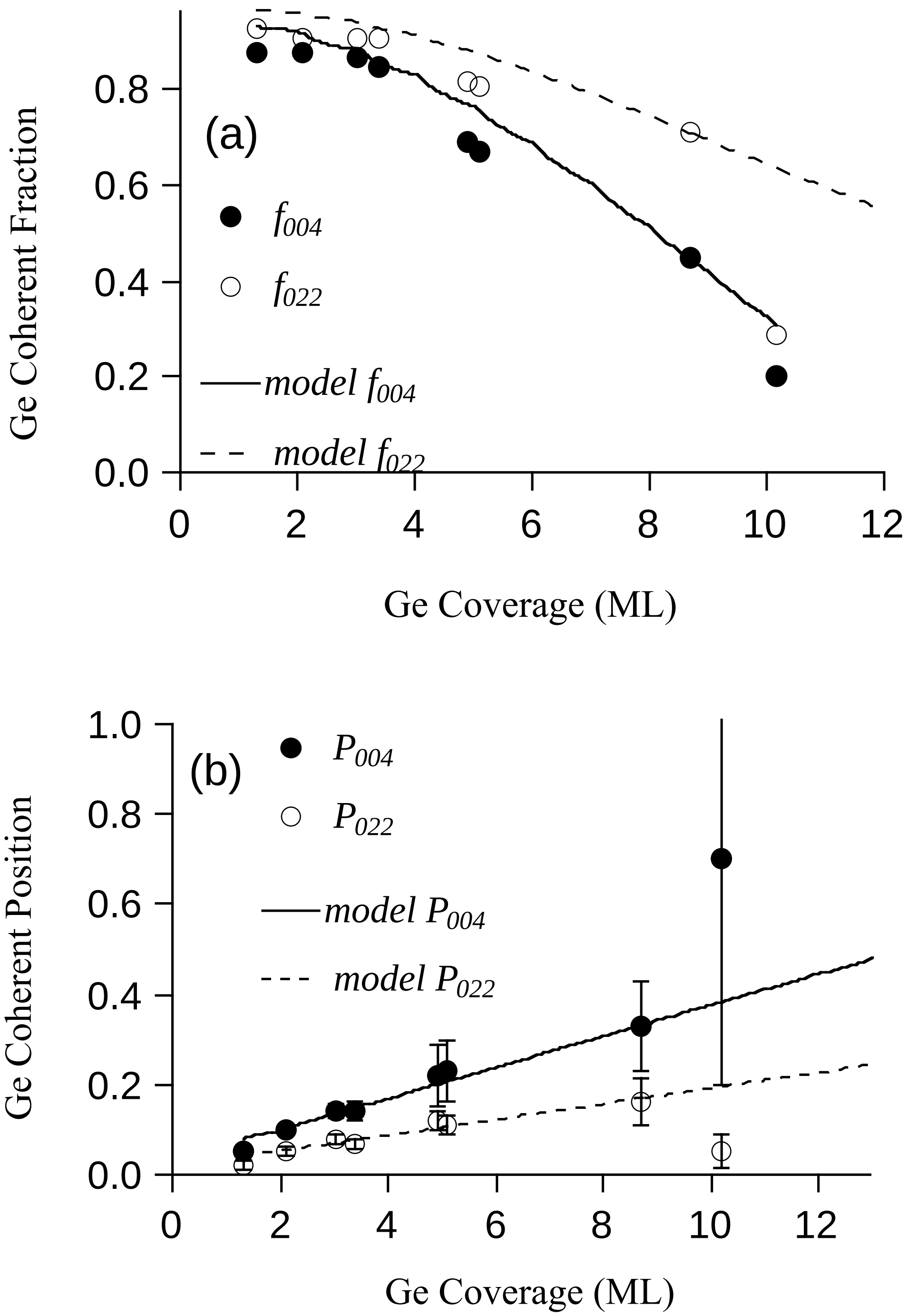

Figure 5.13 Measured and calculated values for **(a)** coherent fraction and **(b)** coherent position vs. Ge coverage for samples with Te. The calculations are based on the elasticity theory.

We have also recently performed a similar study using Bi as the surfactant. [110] In that study, the Ge coherent positions for the samples grown with Bi agreed well with elasticity theory though the coherent fractions for samples above the critical thickness were markedly lower. This implies that like Te, Bi has the effect of preventing inter-diffusion between Si and Ge layers during growth, yet Te is much more effective in preventing the formation of defects for Ge thin films above the critical thickness. The precise reason that Te is more effective is not yet fully understood. It is likely that Te is more effective in reducing Ge adatom diffusion which prevents islanding in the Ge epitaxial film.

Θ (ML)	SME	f_c(004)	P(004)	C	f_c(022)	P(022)
1.3ML	√	0.88	0.05	0.95	0.93	0.02
3.4ML	√	0.87	0.14	1.00	0.91	0.07
5.1ML	√	0.67	0.23	0.90	0.81	0.11
1.1ML		0.72	0.03		0.74	0.01
2.7 ML		0.67	0.05		0.65	0.04
3.7ML		0.37	0.23		0.55	0.12

Table 5.3 Measured values for coherent fraction and coherent position for selected samples with and without surfactant.

Chapter 6 Structure of Si/Ge/Si(111)

6.1 Introduction

In Ge/Si heteroepitaxy the growth of a pseudomorphically strained Ge film forces the relaxation of the Ge film at a very low film thickness. The use of Si(111) substrates is advantageous since a special dislocation geometry and kinetics allow the growth of Ge layers of superior structural and electronic quality, which are far better than on Si(001). The dislocations in a Ge film on Si(111) can move and annihilate [116]. This results in the formation of a defect free relaxed Ge film with dislocations localized at the Ge/Si interface. The use of surfactants in Si/Ge/Si(111) epitaxial growth has proven effective promoting 2D growth and allowed the creation of sharper heterointerfaces. [117]

There exists considerable debate as to whether or not the structures of epitaxial thin films follow a simple linear elastic model at the1-2 ML limit. Using HRTEM Brandt *et al.* [118] indicated that the elastic model breaks down in the limit of 1 ML for InAs laterally strained on GaAs(001). Instead, the distortion of the epitaxial layer is accommodated by the rotation of bond angles and the bond lengths are conserved. This is in contrast to results from XSW and HRXRD measurements conducted on an identical GaAs/InAs/GaAs(001) system[119] where they report the InAs monolayer to be strained between 15% - 19%. This result was also confirmed by Woicik *et al.* and Lee *et al.* using a combination of XSW and EXAFS.[120, 121]

The structure of ultra-thin buried semiconductor thin films grown on the (111) surface is expected to be different than that of the same films grown on (001). This is due to the fact that in the (111) case, the four different directions that the tetrahedral bonds point to in a [111]-orientated film are not all equivalent with respect to the lateral stress. The bond along the [111] direction (growth direction) is expected to be less strained than the bonds parallel to the $[\bar{1}11]$,$[1\bar{1}1]$ and $[1\bar{1}1]$ directions. [122] Therefore, the contraction or expansion of the lattice may not be uniform in the [111] direction. In order to investigate this phenomenon we have studied the structure of the initial stage of Ge grown epitaxially Si(111) with XSW.

Most XSW studies of the initial growth of Ge on Si(111) has been performed in a UHV environment and without Si capping layer. [123-125] In these studies, Bi was used as a surfactant for films from one-half bilayer to 35 bilayers in thickness. It is understood that the critical thickness for Ge/Si(111) is approximately two bilayers. [21] It was found that smooth thick layers of Ge can be grown up to and beyond 30 bilayers [123], however it was determined that these films were relaxed. Therefore, it is still not clear how thick one can grow strained Ge on Si using Bi as a surfactant. Previous XSW studies performed on Ge films less than two BL grown on a Bi-terminated surface measured Ge coherent positions that agree well with elasticity theory. [125] However, the coherent fractions were lower than expected. It was suggested that the surfactant (Bi in this case) induced a distortion of the Ge layer thus lowering both the (111) and (022) expected coherent fraction. The same group performed an XSW study on Ge buried in Si(111) using the (111) reflection for Ge coverages of 0.5 BL and 1 BL grown with and without Sb as a surfactant. For this study, the (111) coherent fractions were slightly higher than for the case without Si cap, though the coherent positions dropped. [126] It was suggested that this the results for the two studies was due to intermixing between the Ge and the Si capping layer.

6.2 Sample preparation

Two Si/Ge/Si(111) heterolayer samples were grown by molecular beam epitaxy using a procedure similar to that described in Chapter 5. One samples (1.1 BL Ge) was grown without surfactant and a slightly thicker film (1.4 BL Ge) was grown with Bi as a surfactant. After Shriaki etching and twelve hours of outgassing at 650°C, the samples were flash annealed several times via indirect heating to 850°C until a sharp 7x7 LEED pattern was observed. Sample cleanliness was confirmed by Auger electron spectroscopy (AES). For the sample with Bi, Bi was deposited first onto a substrate held at 400°C and then annealed to 490°C for ten minutes until a bright ($\sqrt{3}$x$\sqrt{3}$)-R30° LEED pattern formed. Additionally, a Bi overpressure of 10^{-6} Torr was maintained during both Ge and Si growth in order to compensate for possible Bi desorption. Ge was evaporated from a Knudsen cell at a rate of 0.1 ML/min with the substrate held at 400 °C. Continuing at 400 °C, the Si cap was deposited from an e-beam evaporator operating at 110 W with a corresponding growth rate of 1 ML/min. The Ge coverage of each sample, which ranged from 1 to 10 ML was verified by comparing its fluorescence signal to that of an ion-implanted standard.

6.3 XSW experiment

In order to investigate the layer distribution and strain of the buried Ge thin films, we performed (111) and (022) XSW experiments on each sample. Figure 6.1 displays a Ge buried bilayer and the corresponding bulk Si diffraction planes used in the experiment. The measurements were made at the NSLS X15A beamline as well as the 5ID-C beamline at the APS. For all measurements, a non-dispersive setup was used and the monochromator was tuned to produce 12.2 keV x-rays. Ge $K\alpha$ fluorescence was collected by a solid state detector as the sample was scanned through the Bragg angle. For the case of all atoms occupying identical sites, the coherent position gives the relative position for the fluorescing atoms with in the set of substrate lattice planes employed for Bragg diffraction. For the cases with atoms on different sites, the coherent position is determined by a weighted average of these sites. [127] The coherent fraction is a measure for the spread of the distribution of fluorescing atoms around the coherent position. In the case of diamond (111), a perfect crystal shows a coherent fraction of 0.707 due to the buckling of the (111) bilayer. The XSW results are plotted in Figure 6.2 (1.4 BL Ge with Bi) and Figure 6.3 (1.1 BL Ge without surfactant).

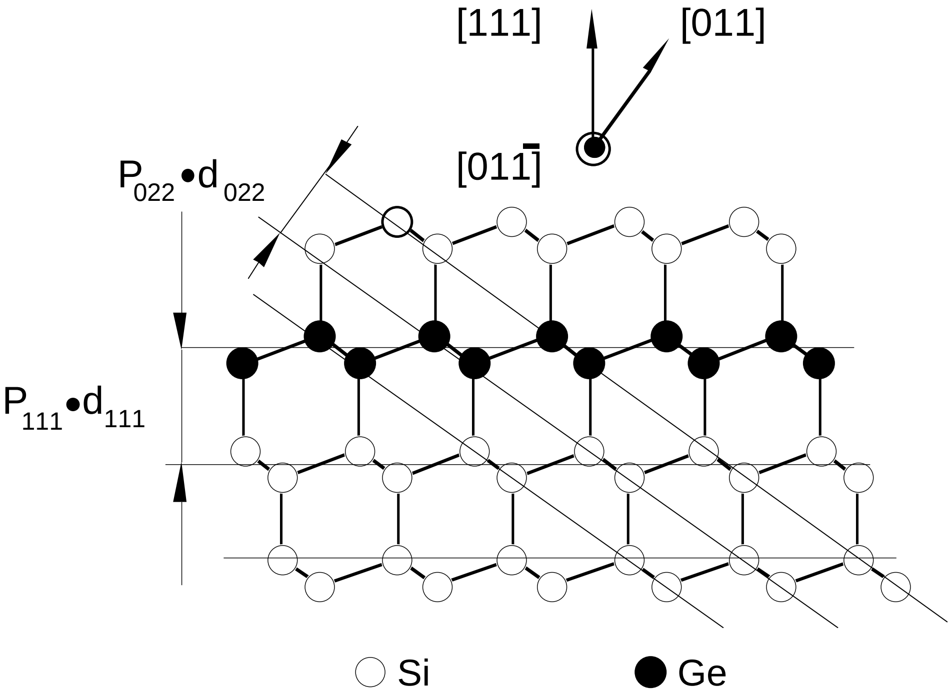

Figure 6.1 Schematic of 1 BL Ge buried in Si(111) and relevant Si substrate diffracting planes used in XSW measurement.

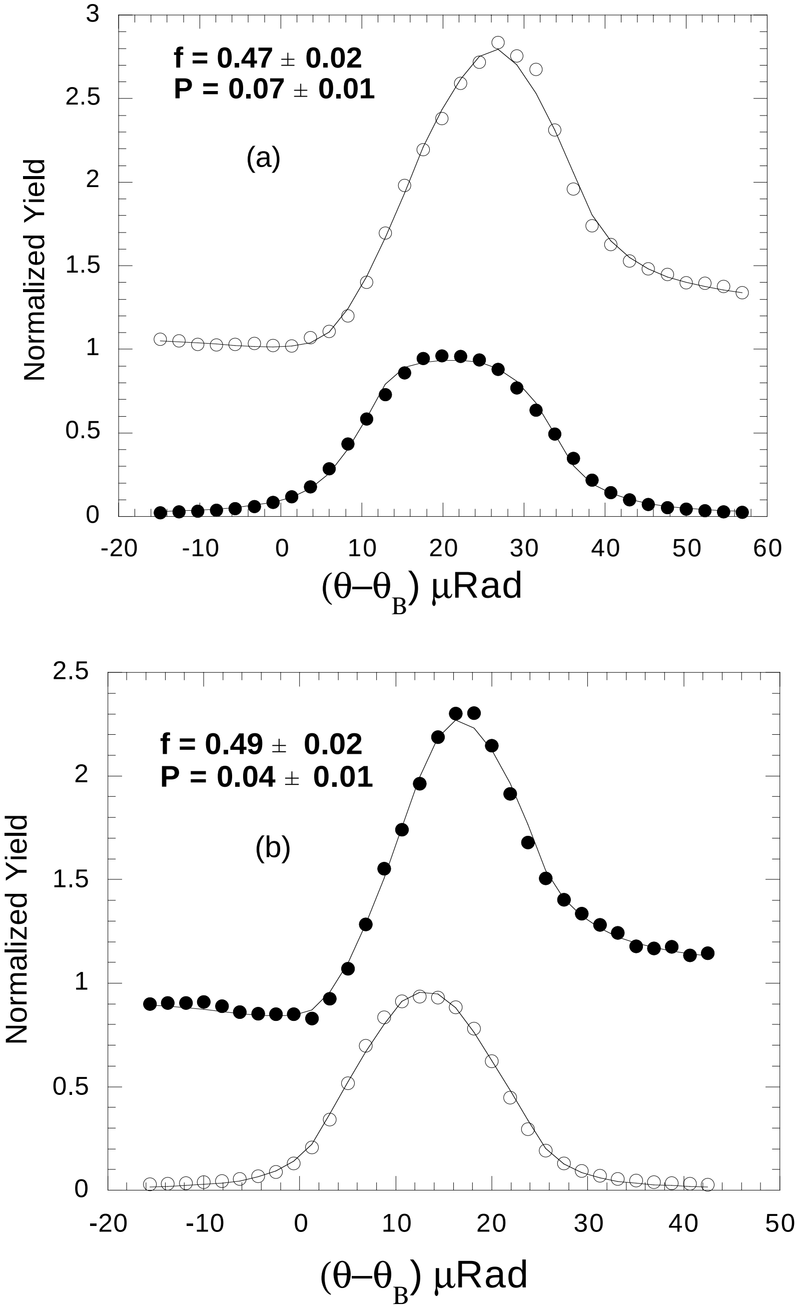

Figure 6.2 The experimental and theoretical angular dependency of the Ge Kα fluorescence yield and reflectivity collected while scanning in angle through (a) the Si(111) and (b) Si(022) reflection. The sample is 1.4 BL Ge/Si(111) with Bi as surfactant.

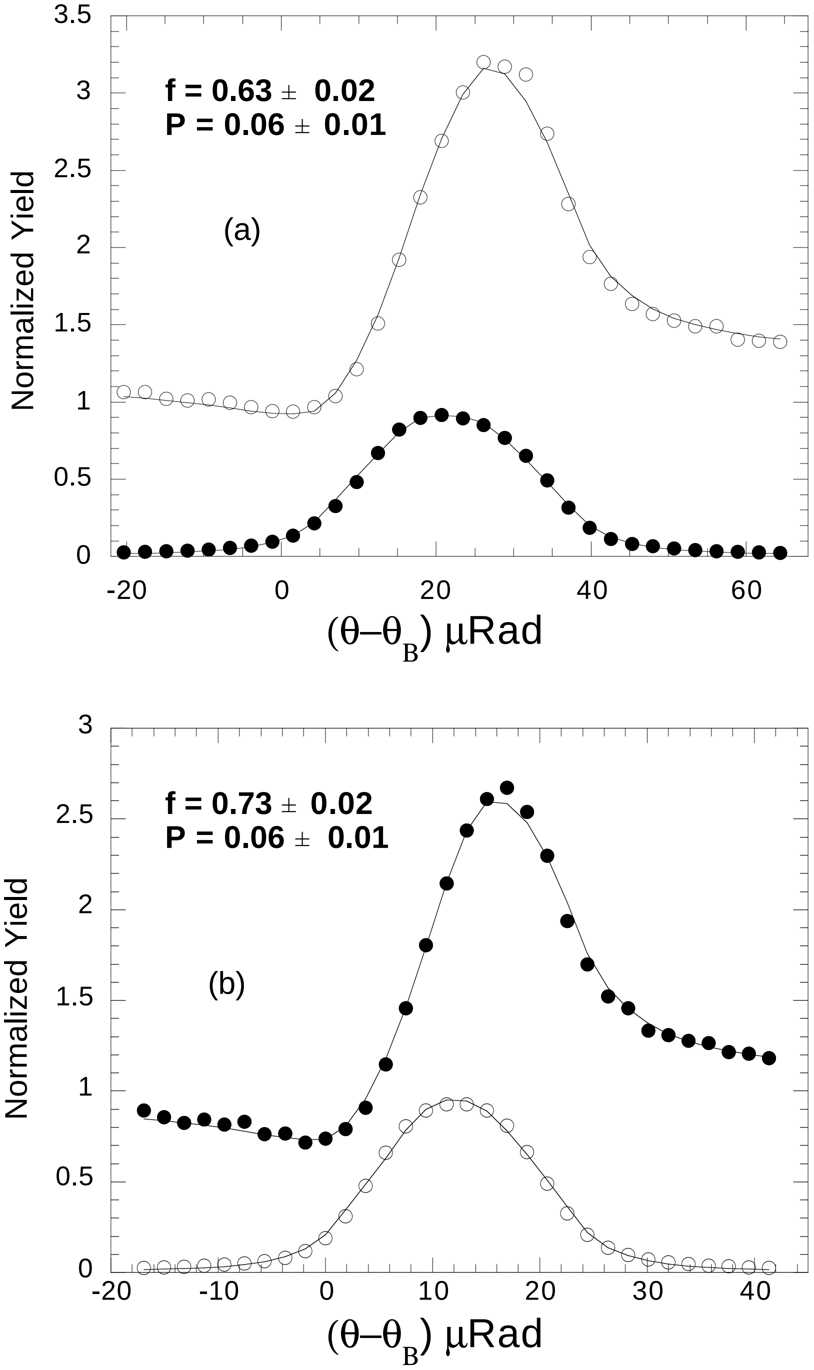

Figure 6.3 The experimental and theoretical angular dependency of the Ge Kα fluorescence yield and reflectivity collected while scanning in angle through (a) the Si(111) and (b) Si(022) reflection. The sample is 1.1 BL Ge/Si(111) with no surfactant.

6.4 Discussion

In order to construct a model for our results we must consider each sample individually since different growth modes are expected for samples with and without surfactant. Herein I will refer to sample 1 as 1.4 BL Ge with Bi as surfactant and sample 2 as 1.1 BL Ge grown with no surfactant. An important assumption to be made for both samples is that the Ge atoms are equally distributed in the upper and lower half of the bilayer level. This is a fairly good assumption for growth on (111) surfaces as verified by STM. [128] Sample 1 was grown with a surfactant so we will also assume in this case that the growth proceeded layer by layer. This implies that occupation of the second bilayer starts upon the completion of the initial bilayer and that only the first and second bilayer are occupied by Ge. Since multiple sites are occupied, the resulting coherent position, P, and coherent fraction, f_c, are obtained, related to the position P_i and the probability, x_i, of the individual sites in the following way [127]:

$$\tan(2\pi P) = \frac{\sum_i x_i \sin(2\pi P_i)}{\sum_i x_i \cos(2\pi P_i)} \quad , \qquad (6.1)$$

$$f_c = C\left[\left[\sum_i x_i \sin(2\pi P_i)\right]^2 + \left[\sum_i x_i \cos(2\pi P_i)\right]^2\right]^{1/2} D_H \qquad (6.2)$$

with $\sum_i x_i = 1$. It should be noted that the fitting parameters f_c and P for this study are identical to the discussion in Chapter 5 and in Equations 3.43 - 3.44. The above expressions are better suited for this study where growth proceeds as bilayers, as opposed to individual monolayers for the (001) orientation. For the case of Ge on Si(111) there exists a lattice mismatch of 4.2%. We can calculate the expansion of the Ge film according to elasticity theory for (111)-oriented heterolayers as follows:

$$\varepsilon_\perp = -\left(\frac{2C_{11} + 4C_{12} - 4C_{44}}{C_{11} + 2C_{12} - 4C_{44}}\right)\varepsilon_{\|} \quad . \tag{6.3}$$

Thus for $\varepsilon_{\|}$ = - 0.042 we calculate $\varepsilon_\perp$= 0.01 using published values of C_{xy} for Ge. [112] Following this model, elasticity theory predicts P_{111} = 0.03 for a perfect 1.4 BL of Ge on Si(111). Also incorporated into this model is a vertical shift of 0.02 in coherent position which takes into account the interface offset due to the Si-Ge bond. This is the same as δ' from discussion in Chapter 5. Our measured value of P = 0.07 for this sample implies that this simple elasticity theory model is insufficient to describe our system. This implies a much larger expansion in our bilayer than predicted by elasticity theory. If the atoms in the bottom half of each bilayer are held stationary while the upper half expands 5% of a layer spacing then one would generate the observed coherent position of 0.07. For this model a coherent fraction of 0.56 is expected. Our measured value of 0.47 is slightly lower than this value. The presence of disordered Ge (~15%) could, in principle, account for this difference. Voigtlander *et al.* [128] performed STM measurements of Ge SME at different growth temperatures and found that growth below 530^0C results in the formation of stacking fault defects on the surface. At our growth temperature of 400^0C, it is likely these defects are present to some degree and contribute to a reduced Ge coherent fraction. Intermixing of Ge and Si at the interface, which has been found significant in Ga-SME of Ge/Si [43], cannot be completely ruled out. Nevertheless, site exchanges for Ge and Si would lead to a shift of the coherent position and to an increase of f_{Ge} instead of the decrease observed. The (022) coherent position of $P = 0.04$ is also consistent with this model for the expanded Ge layer. The measured (022) coherent fraction for this sample is remarkably low ($f = 0.49$) as it would be expected to be ~0.75 for the model presented. It is likely that the stacking faults mentioned previously have a strong effect in lowering the coherent fraction in-plane more so than out-of-plane.

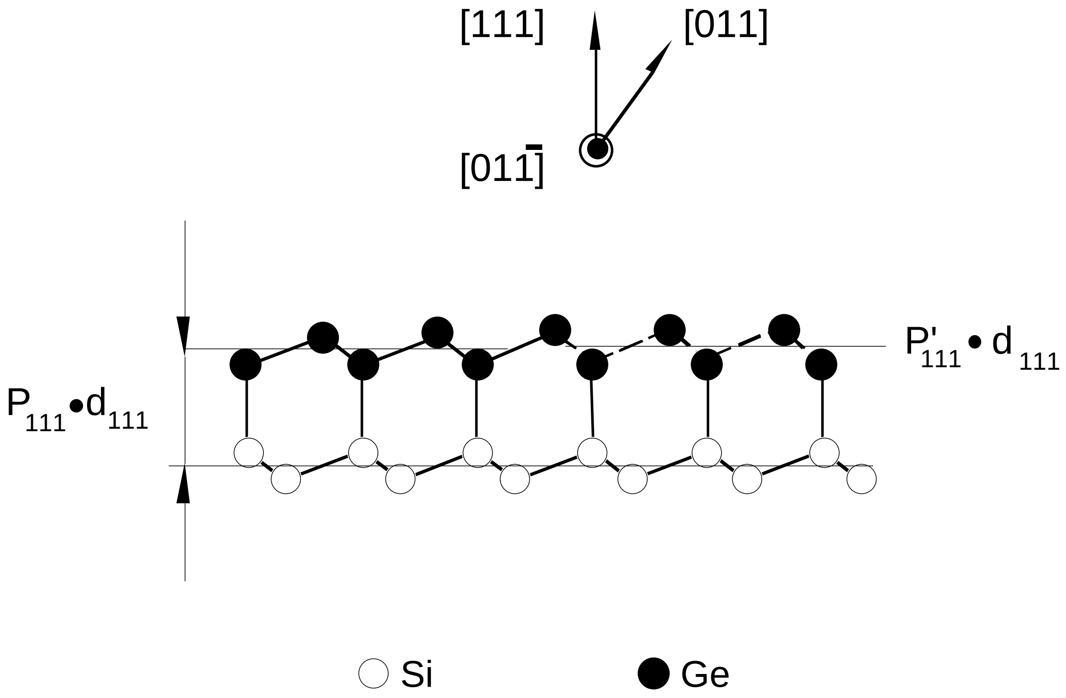

Figure 6.4 Schematic of expanded Ge bilayer as measured by XSW. Left side (solid lines) pertain to elasticity theory model. Right side (dashed lines) pertain to our expanded bilayer model.

For sample 2 (1.1 BL without Bi) we expect a different growth mode. In Chapter 2 it was shown that Ge growth on a bare Si(111) surface initiates as islands and doesn't become layered until slightly beyond 1 BL. Since no surfactant was used in this sample, it is expected that layer-by-layer growth has not yet initiated and that there most likely exists Ge occupying three different bilayers, thus leaving some Si uncovered. Referring back to Figure 2.4 for 1 BL of Ge on Si(111), the STM image estimates ~80% Ge in the first bilayer, 20% in the second bilayer and a few % in the third bilayer. To simulate the structure for the 1.1 BL sample, I have distributed the Ge atoms 80% in the first layer and 20% in the second layer assuming the same 5%

expansion of the Ge bilayers used in the analysis of sample 1. This leads to a coherent position of 0.06 and a coherent fraction of 0.56. The simulation agrees with our measure of coherent position, however, our coherent fraction of 0.63 is too high for this simple model. Since a surfactant was not used in this sample, it is possible that Ge could have diffused into the Si capping layer. After Si growth, AES did not detect Ge on the surface, however, Ge could still be distributed in the capping layer. Ge atoms occupying substitutional sites in the Si capping layer would lead to an increase in the coherent fraction. A previous XSW study of a 1 BL Ge film grown without surfactant buried in Si(111) measured $f_c = 0.62$ and $P = 0$ for Ge. [126] They pointed to significant intermixing in their samples to explain these results. Their sample was grown at 490^0 C where it has been documented that the interdiffusion coefficient between Ge and Si (for Ge on Si(111)) is ten times greater than for our growth temperature of 400^0C. [103] The measured 022 coherent fraction of 0.73 in our study is consistent with the model for this structure if one neglects intermixing.

6.5 Preliminary SEXAFS

In order to more completely support our XSW measurements we carried out EXAFS measurements to directly determine the Ge-Ge and Ge-Si bondlengths. We anticipate a bondlength split between bonds along the [111] direction and the bonds parallel to the $[\bar{1}11]$,$[1\bar{1}1]$, and $[1\bar{1}1]$ directions. This is due to the epitaxial Ge film that is lattice matched to the Si substrate in-plane and expanded out-of-plane.

In EXAFS we measure the energy dependence of the absorption coefficient $\mu(E)$ is related to the transmitted (I) and incident (I_o) fluxes by:

$$\frac{I}{I_o} = \exp^{(-\mu E(x))} \tag{6.4}$$

The absorption coefficient is related to the cross section σ (cm^2/g) and the density ρ (g/cm^3) by:

$$\mu = \rho\sigma \approx \sum_i \rho_i \sigma_i = \rho \sum_i (m_i / M)\sigma_i \tag{6.5}$$

where the sum is over the elements (i) , in the sample of mass fraction m_i/M. This expression is approximate due to the fact that the total absorption is not simply the sum of the atomic absorption coefficients. The proximity of the neighboring atoms strongly modulates the absorption coefficient as a function of energy, thus making EXAFS a useful tool for structural analysis. In an EXAFS experiment the incident energy is scanned around an absorption edge (typically K-edge) of the element of interest. The x-ray absorption coefficient above an absorption edge displays an oscillatory behavior resulting from the phase difference between a photoelectron wave directly emitted from an absorbing atom and a partial wave that is backscattered from a near neighbor. In simplified form, the normalized k^2-weighted EXAFS arising from a single scatterer at a distance, r, from the absorber may be written:

$$k^2\chi(k) = |f(k)| \sin[2kr + \psi(k)]. \tag{6.6}$$

Here k is the electron-wave vector, $|f(k)|$ is the backscattering amplitude of the scatterer, and $\psi(k)$ is the total electronic contribution to the phase difference between the directly emitted and backscattered electrons.

The Si/Ge/Si(111) samples were measured in two different geometries; the sample surface parallel (in-plane) and perpendicular (out-of-plane) to the polarization of the incident x-rays (Figure 6.5).

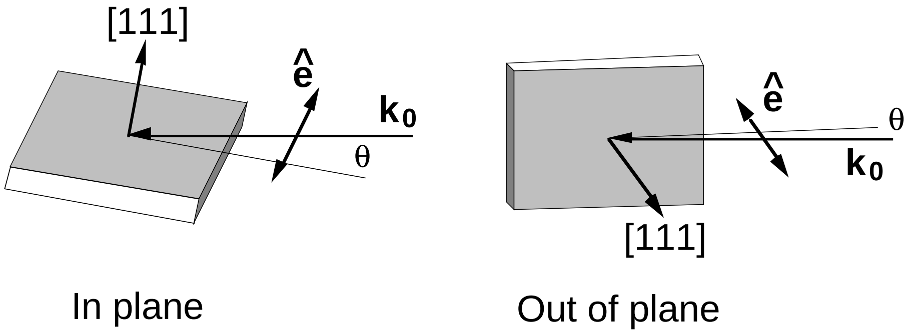

Figure 6.5 The in-plane and out-of-plane geometries for the polarization-dependent EXAFS measurements.

Since the cross section of the photoelectric effect has an angular dependence and is proportional to, $\left(\hat{e}\cdot\hat{r}_j\right)^2$, where $\hat{e}$ is the polarization vector of the incident x-rays and $\hat{r}_j$ in this case is the unit vector pointing from the emitting atom to its j^{th} first-shell atom. The in-plane geometry has made the Ge bonds parallel to the [111] direction completely invisible to the EXAFS measurement, while for the out-of-plane geometry, 75% of the EXAFS signal was contributed by the Ge-Ge and Si-Ge bonds parallel to the [111] direction and 25% by those parallel to the [$\bar{1}$11],[1$\bar{1}$1] and [1$\bar{1}$1] directions.

The energy scans for were performed both at the X15A beamline at the NSLS and the 5ID-C beamline at the APS. Ge K fluorescence x-rays from the samples were recorded by a solid state detector. The samples were spun at a few hundred RPM to smear out the glitches and spikes in the EXAFS spectra due to Bragg reflections. The incident angle was about 0.5 degrees for both the in-plane geometry and the out-of-plane geometry. A Ge standard (~250 μm foil) was also measured in transmission. The purpose of the standard is to determine experimentally the phase shift of the backscattered electrons from the Ge-Ge neighbors. The data from sample 2 in the in-plane and out-of-plane orientation are plotted in Figure 6.6 along with the data for the Ge standard. Figure 6.7 shows the magnitude of the Fourier Transform of the k-weighted EXAFS, ($k\chi(k)$), for the three scans from Figure 6.6. The peaks around R = 2 correspond to the first-nearest neighbor distances for the Ge atoms. It can be inferred from this figure that the EXAFS spectra obtained from the sample has additional features as compared with the Ge standard. This is due to both Si and Ge backscattering in the first shell. We are in the process of fitting the first shell data for these scans.

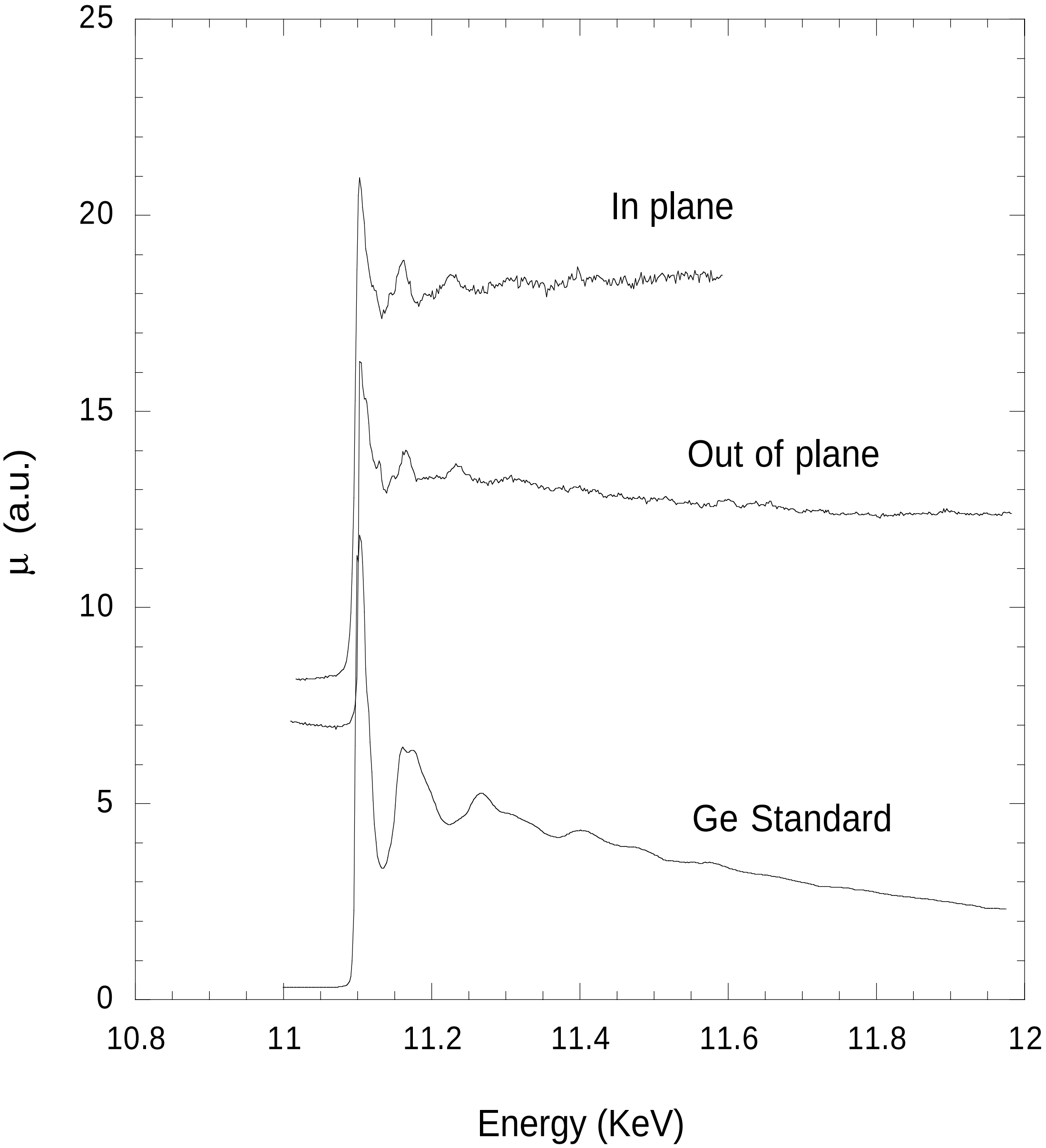

Figure 6.6 Raw EXAFS spectra for sample 2 and Ge standard.

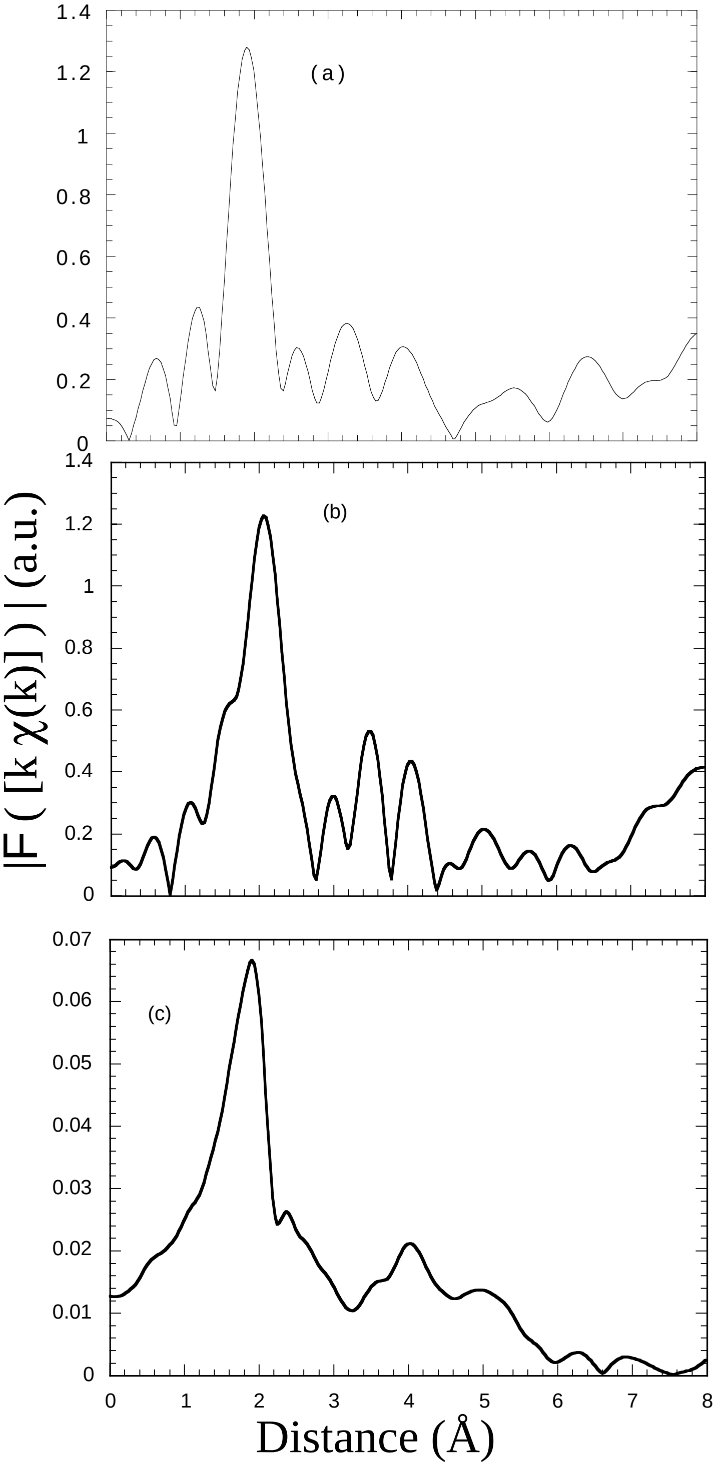

Figure 6.7 Magnitudes of the Fourier transform of the k-weighted EXAFS, $k\chi(k)$, for sample 2 (a) in-plane, (b) out-of-plane, and (c) the Ge standard.

6.6 Conclusions

We have investigated the initial stage of growth for Ge grown on Si(111) with and without Bi as a surfactant. It is suggested from our model that continuum elasticity theory is insufficient to model our results. We find for the case where Bi was used as a surfactant (Sample 1) that the Ge layer is expanded in the growth direction by a greater amount than the 1% predicted by elasticity theory. For the 1.1 BL sample grown without surfactant, the high value for (111) coherent fraction suggests that some degree of intermixing between the Ge and Si capping layer has occurred. The high coherent position for this sample suggests that the Ge is not growing layer by layer, but rather it is occupying three different Ge bilayer levels despite a total coverage of only 1.1 BL. We are in the process of analyzing EXAFS data to supplement our XSW investigation.

Chapter 7 Summary

This thesis has demonstrated the effectiveness of x-ray techniques in determining relevant structural quantities for adsorbate induced semiconductor surface reconstructions as well as buried epitaxial structures. Our x-ray studies were able to clearly identify differences in the structure of Si/Ge/Si heterostructures grown with and without surfactants.

Using surface x-ray scattering we investigated the Te/Ge(001) saturated surface (~0.8 ML). Using roughness and scale factor as variables for our fit, we determined that bridge site adsorption resulted in the lowest value for χ^2 and therefore the best agreement to our data. Upon the determination of the adsorption site, we refined our fit by allowing for surface relaxations in the Te layer and the near surface Ge layers. This reduced the χ^2 value even further.

Building on this study, we employed Te as a surfactant in the growth of Si/Ge/Si(001) heterostructures. Using a variety of x-ray techniques, we compared the structure of these films to others grown without Te. Specular reflectivity revealed that the interface quality of the films grown with Te was superior to those grown without Te. 00L crystal truncation rods through the (004) Bragg peak were use to determined that films grown with Te were strained out-of-plane less than 0.5% of the amount predicted by elasticity theory. Grazing incidence diffraction verified that the in-plane structure of 9 ML of Ge buried in Si was coherent with the Si(001) substrate, while the same film grown without surfactant was not. A comprehensive XSW study of samples between 1 and 10 ML in Ge coverage grown with and without Te was performed to determine the registry of the Ge atoms with the Si(001) substrate. From this experiment we found that samples grown with Te up to 9 ML in coverage had coherent fractions and coherent positions that agreed well with continuum elasticity theory, where similar samples grown without Te deviated significantly from this model.

Finally, we investigated the local structure of Ge buried in Si(111) grown with and without Bi as a surfactant. Continuum elasticity theory predicts that if the Ge epitaxial layer is lattice-matched in-plane that the (111) layer spacing will be distorted by 1% out-of-plane. Our XSW study measured an out-of-plane layer spacing that suggests the Ge bilayer is instead expanded by 5%. Our measurements also suggest a different growth mode for Ge on Si(111) grown with Bi (2D) compared with the initial growth of Ge on Si(111) without Bi (3D).

References

[1] W. Shockley, Bell System Tech **28**, 436 (1949).

[2] J. C. Bean, L. C. Feldman, A. T. Fiory, S. Nakahara, and I. K. Robinson, Journal of Vacuum Science & Technology a-Vacuum Surfaces and Films **2**, 436 (1984).

[3] J. C. Bean, T. T. Sheng, L. C. Feldman, A. T. Fiory, and R. T. Lynch, Applied Physics Letters **44**, 102 (1984).

[4] G. Abstreiter, H. Brugger, T. Wolf, H. Jorke, and H. J. Herzog, Physical Review Letters **54**, 2441 (1985).

[5] H. Daembkes, H. J. Herzog, H. Jorke, H. Kibbel, and E. Kaspar, IEEE Transactions on Electron Devices **33**, 633 (1986).

[6] T. P. Pearsall and J. C. Bean, IEEE Electron Device Letters **7**, 308 (1986).

[7] S. Luryi, T. P. Pearsall, H. Temkin, and J. C. Bean, Ieee Electron Device Letters **7**, 104 (1986).

[8] C. G. van de Walle and R. M. Martin, Physical Review B **34**, 5621 (1986).

[9] S. Fukatsu, H. Akiyama, Y. Shiraki, and H. Sakaki, Journal of Crystal Growth **157**, 1 (1995).

[10] D. C. Houghton, Journal of Applied Physics **70**, 2136 (1991).

[11] R. Hull, J. C. Bean, D. J. Werder, and R. E. Leibenguth, Applied Physics Letters **52**, 1605 (1988).

[12] E. Murakami, K. Nakagawa, A. Nishida, and M. Miyao, IEEE Electron Device Letters **12**, 71 (1991).

[13] U. Konig and F. Schaffler, IEEE Electron Device Letters **14**, 205 (1993).

[14] M. Arafa, K. Ismail, P. Fay, J. O. Chu, B. S. Meyerson, and I. Adesida, Electronics Letters **31**, 680 (1995).

[15] I. Adesida, M. Arafa, K. Ismail, J. O. Chu, and B. S. Meyerson, Microelectronic Engineering **35**, 257 (1997).

[16] E. Bauer, Z. Kristallogr. **110**, 372 (1958).

[17] F. C. Frank and J. H. van der Merwe, Proc. Roy. Soc. **198**, 205 (1949).

[18] M. Volmer and A. Weber, Z. Phys. Chem. **119**, 227 (1926).

[19] I. N. Stranski and L. Krastanow, Sitzungsberichte der Akademie der Wissenschaften Wien, Mathematisch Naturwissenschaftliche Klasse, Abteilung IIB, Chemie, Band 146, 1938, p. 797. **146**, 3570 (1938).

[20] J. Tersoff and F. K. Legoues, Physical Review Letters **72**, 3570 (1994).

[21] U. Kohler, O. Jusko, G. Pietsch, B. Muller, and M. Henzler, Surface Science **248**, 321 (1991).

[22] P. M. J. Maree, K. Nakagawa, F. M. Mulders, J. F. van der Veen, and K. L. Kavanagh, Surface Science **191**, 305 (1987).

[23] F. K. LeGoues, M. Hammar, M. C. Reuter, and R. M. Tromp, Surface Science **349**, 249 (1996).

[24] R. S. Becker, J. A. Golovchenko, and B. S. Swartzentruber, Physical Review B **32**, 8455 (1985).

[25] S. K. Theiss, D. M. Chen, and J. A. Golovchenko, Applied Physics Letters **66**, 448 (1995).

[26] B. Voigtlander, A. Zinner, and T. Weber, Review of Scientific Instruments **67**, 2568 (1996).

[27] A. W. D. van der Gon, R. M. Tromp, and M. C. Reuter, Thin Solid Films **236**, 140 (1993).

[28] U. Kohler, O. Jusko, B. Muller, M. Hornvonhoegen, and M. Pook, Ultramicroscopy **42**, 832 (1992).

[29] F. Iwawaki, M. Tomitori, and O. Nishikawa, Ultramicroscopy **42**, 902 (1992).

[30] F. Wu and M. G. Lagally, Physical Review Letters **75**, 2534 (1995).

[31] B. Voigtlander and M. Kastner, Physical Review B **60**, R5121 (1999).

[32] R. M. Tromp, Physical Review B **47**, 7125 (1993).

[33] F. Liu, F. Wu, and M. G. Lagally, Chemical Reviews **97**, 1045 (1997).

[34] S. M. Pintus, S. I. Stenin, A. I. Toropov, E. M. Trukhanov, and V. Y. Karasyov, Thin Solid Films **151**, 275 (1987).

[35] Y. W. Mo, D. E. Savage, B. S. Swartzentruber, and M. G. Lagally, Physical Review Letters **65**, 1020 (1990).

[36] J. A. Floro, E. Chason, L. B. Freund, R. D. Twesten, R. Q. Hwang, and G. A. Lucadamo, Physical Review B **59**, 1990 (1999).

[37] D. J. Eaglesham and M. Cerullo, Physical Review Letters **64**, 1943 (1990).

[38] T. I. Kamins, E. C. Carr, R. S. Williams, and S. J. Rosner, Journal of Applied Physics **81**, 211 (1997).

[39] M. Copel, M. C. Reuter, E. Kaxiras, and R. M. Tromp, Physical Review Letters **63**, 632 (1989).

[40] M. Horn von Hoegen, F. K. Legoues, M. Copel, M. C. Reuter, and R. M. Tromp, Physical Review Letters **67**, 1130 (1991).

[41] H. Presting, U. Menczigar, and H. Kibbel, Journal of Vacuum Science & Technology B **11**, 1110 (1993).

[42] U. Menczigar, G. Abstreiter, J. Olajos, H. Grimmeiss, H. Kibbel, H. Presting, and E. Kasper, Physical Review B **47**, 4099 (1993).

[43] J. Falta, M. Copel, F. K. Legoues, and R. M. Tromp, Applied Physics Letters **62**, 2962 (1993).

[44] X. W. Lin, Z. Liliental-Weber, J. Washburn, E. R. Weber, A. Sasaki, A. Wakahara, and T. Hasegawa, Journal of Vacuum Science & Technology B **13**, 1805 (1995).

[45] M. Copel, M. C. Reuter, M. H. von Hoegen, and R. M. Tromp, Physical Review B **42**, 11682 (1990).

[46] A. Kawano, I. Konomi, H. Azuma, T. Hioki, and S. Noda, Journal of Applied Physics **74**, 4265 (1993).

[47] W. Rodrigues, O. Sakata, T. L. Lee, D. A. Walko, D. L. Marasco, and M. J. Bedzyk, Journal of Applied Physics **88**, 2391 (2000).

[48] S. Higuchi and Y. Nakanishi, Surface Science **254**, L465 (1991).

[49] S. Higuchi and Y. Nakanishi, Journal of Applied Physics **71**, 4277 (1992).

[50] B. Voigtlander, A. Zinner, T. Weber, and H. P. Bonzel, Physical Review B **51**, 7583 (1995).

[51] Y. J. Ko, K. J. Chang, and J. Y. Yi, Physical Review B **60**, 1777 (1999).

[52] F. K. Legoues, M. Copel, and R. M. Tromp, Physical Review B **42**, 11690 (1990).

[53] F. K. Legoues, M. Horn von Hoegen, M. Copel, and R. M. Tromp, Physical Review B **44**, 12894 (1991).

[54] B. E. Warren, *X-ray Diffraction* (Addison-Wesler, Massachusetts, 1969).

[55] J. J. Sakurai, *Advanced Quantum Mechanics* (Addison-Wesley, New York, 1967).

[56] C. H. MacGillavry and G. D. Rieck, *International Tables for X-ray Crystallography* (Reidel,Dordrecht, 1983).

[57] N. W. Ashcroft and N. D. Mermin, *Solid State Physics* (Saunders College, Philadelphia, 1976).

[58] R. Feidenhansl, Surface Science Reports **10**, 105 (1989).

[59] I. K. Robinson and D. J. Tweet, Reports on Progress in Physics **55**, 599 (1992).

[60] I. K. Robinson, Physical Review B **33**, 3830 (1986).

[61] B. W. Batterman and H. Cole, Rev. Mod. Phys., **36**, 681 (1964).

[62] P. P. Ewald, Physik. Z. **14**, 465 (1913).

[63] N. Hertel, G. Materlik, and J. Zegenhagen, Zeitschrift Fur Physik B-Condensed Matter **58**, 199 (1985).

[64] M. J. Bedzyk and G. Materlik, Physical Review B **32**, 6456 (1985).

[65] R. E. Schlier and H. E. Farnsworth, J. Chem Phys. **30**, 917 (1959).

[66] R. M. Tromp, R. J. Hamers, and J. E. Demuth, Physical Review Letters **55**, 1303 (1985).

[67] R. Felici, I. K. Robinson, C. Ottaviani, P. Imperatori, P. Eng, and P. Perfetti, Surface Science **375**, 55 (1997).

[68] C. B. Duke, Chemical Reviews **96**, 1237 (1996).

[69] D. Haneman, Reports on Progress in Physics **50**, 1045 (1987).

[70] H. Kroemer, Journal of Vacuum Science & Technology B **5**, 1150 (1987).

[71] R. S. Becker, T. Klitsner, and J. S. Vickers, Journal of Microscopy-Oxford **152**, 157 (1988).

[72] J. Nogami, A. A. Baski, and C. F. Quate, Applied Physics Letters **58**, 475 (1991).

[73] H. P. Noh, C. Park, D. Jeon, K. Cho, T. Hashizume, Y. Kuk, and T. Sakurai, Journal of Vacuum Science & Technology B **12**, 2097 (1994).

[74] W. Monch, *Semiconductor Surfaces and Interfaces* (Springer, 1995).

[75] Y. Qian, M. J. Bedzyk, S. Tang, A. J. Freeman, and G. E. Franklin, Physical Review Letters **73**, 1521 (1994).

[76] R. D. Bringans, D. K. Biegelsen, J. E. Northrup, and L. E. Swartz, Japanese Journal of Applied Physics Part 1-Regular Papers Short Notes & Review Papers **32**, 1484 (1993).

[77] T. Weser, A. Bogen, B. Konrad, R. D. Schnell, C. A. Schug, W. Moritz, and W. Steinmann, Surface Science **201**, 245 (1988).

[78] N. Takeuchi, Surface Science **426**, L433 (1999).

[79] P. F. Lyman, D. L. Marasco, D. A. Walko, and M. J. Bedzyk, Physical Review B **60**, 8704 (1999).

[80] Y. J. Zhao, M. Jiang, G. M. Lai, and P. L. Cao, Physics Letters A **255**, 361 (1999).

[81] H. J. Osten, J. Klatt, G. Lippert, E. Bugiel, and S. Higuchi, Journal of Applied Physics **74**, 2507 (1993).

[82] K. Tamiya, T. Ohtani, Y. Takeda, T. Urano, and S. Hongo, Surface Science **408**, 268 (1998).

[83] T. Ohtani, K. Tamiya, Y. Takeda, T. Urano, and S. Hongo, Applied Surface Science **132**, 112 (1998).

[84] S. R. Burgess, B. C. C. Cowie, S. P. Wilks, P. R. Dunstan, C. J. Dunscombe, and R. H. Williams, Applied Surface Science **104**, 152 (1996).

[85] M. R. Bennett, C. J. Dunscombe, A. A. Cafolla, J. W. Cairns, J. E. Macdonald, and R. H. Williams, Surface Science **380**, 178 (1997).

[86] N. Takeuchi, Physical Review B **60**, 4796 (1999).

[87] S. A. Yoshikawa, J. Nogami, C. F. Quate, and P. Pianetta, Surface Science **321**, L183 (1994).

[88] O. Sakata, P. F. Lyman, B. P. Tinkham, D. A. Walko, D. L. Marasco, T. L. Lee, and M. J. Bedzyk, Physical Review B **61**, 16692 (2000).

[89] P. F. Lyman, M. J. Bedzyk, and D. T. Keane, in *Synchrotron Radiation Instrumentation*, edited by E. Fontes (AIP, Woodbury, NY, 1997), p. 10

[90] I. K. Robinson, Physical Review B **33**, 3830 (1986).

[91] Y. H. Xie, Materials Science & Engineering R-Reports **25**, 89 (1999).

[92] M. Horn von Hoegen, B. H. Muller, A. Alfalou, and M. Henzler, Physical Review Letters **71**, 3170 (1993).

[93] J. M. C. Thornton, A. A. Williams, J. E. Macdonald, R. G. van Silfhout, J. F. van der Veen, M. Finney, and C. Norris, Journal of Vacuum Science & Technology B **9**, 2146 (1991).

[94] X. W. Lin, Z. Liliental-Weber, J. Washburn, E. R. Weber, A. Sasaki, A. Wakahara, and T. Hasegawa, Physical Review B **52**, 16581 (1995).

[95] M. H. a. K. Anderko, *Constitution of Binary Alloys* (McGraw-Hill, New York, 1985).

[96] A. Ishizaka and Y. Shiraki, Journal of the Electrochemical Society **133**, 666 (1986).

[97] J. D. Jackson, *Classical Electrodynamics* (Wiley, John & Sons, Incorporated, 1998).

[98] P. S. Pershan and J. Alsnielsen, Physical Review Letters **52**, 759 (1984).

[99] S. Brennan and P. L. Cowan, Review of Scientific Instruments **63**, 850 (1992).

[100] B. P. Uberuaga, M. Leskovar, A. P. Smith, H. Jonsson, and M. Olmstead, Physical Review Letters **84**, 2441 (2000).

[101] D. Bahr, J. Falta, G. Materlik, B. H. Muller, and M. Horn von Hoegen, Physica B **221**, 96 (1996).

[102] P. C. Zalm, G. F. A. van de Walle, D. J. Gravesteijn, and A. A. Vangorkum, Applied Physics Letters **55**, 2520 (1989).

[103] K. Nakagawa and M. Miyao, Journal of Applied Physics **69**, 3058 (1991).

[104] J. Falta, D. Bahr, G. Materlik, B. H. Muller, and M. Horn von Hoegen, Applied Physics Letters **68**, 1394 (1996).

[105] I. K. Robinson, R. T. Tung, and R. Feidenhansl, Physical Review B **38**, 3632 (1988).

[106] A. A. Williams, J. M. C. Thornton, J. E. Macdonald, R. G. van Silfhout, J. F. van der Veen, M. S. Finney, A. D. Johnson, and C. Norris, Physical Review B **43**, 5001 (1991).

[107] J. M. C. Thornton, A. A. Williams, J. E. Macdonald, R. G. van Silfhout, M. S. Finney, and C. Norris, Surface Science **273**, 1 (1992).

[108] J. Falta, D. Bahr, G. Materlik, B. H. Muller, and M. Horn-von Hoegen, Surface Review and Letters **5**, 145 (1998).

[109] M. Takahasi, S. Nakatani, T. Takahashi, X. W. Zhang, N. Ando, S. Fukatsu, and Y. Shiraki, Japanese Journal of Applied Physics Part 1-Regular Papers Short Notes & Review Papers **34**, 2278 (1995).

[110] W. P. Rodrigues, in *Physics and Astronomy* (Northwestern University, Evasnston, 2000), p. 120.

[111] J. Zegenhagen, Surface Science Reports **18**, 199 (1993).

[112] H. B. Huntington, Solid State Phys. **7**, 214 (1958).

[113] M. J. Bedzyk and G. Materlik, Physical Review B **31**, 4110 (1985).

[114] K. G. Huang, W. M. Gibson, and J. Zegenhagen, Physical Review B **40**, 4216 (1989).

[115] B. P. Uberuaga, M. Leskovar, A. P. Smith, H. Jonsson, and M. Olmstead, Physical Review Letters **84**, 2441 (2000).

[116] M. Horn von Hoegen, A. Alfalou, H. Pietsch, B. H. Muller, and M. Henzler, Surface Science **298**, 29 (1993).

[117] M. Horn von Hoegen, M. Copel, J. C. Tsang, M. C. Reuter, and R. M. Tromp, Physical Review B **50**, 10811 (1994).

[118] O. Brandt, K. Ploog, R. Bierwolf, and M. Hohenstein, Physical Review Letters **68**, 1339 (1992).

[119] C. Giannini, L. Tapfer, S. Lagomarsino, J. C. Boulliard, A. Taccoen, B. Capelle, M. Ilg, O. Brandt, and K. H. Ploog, Physical Review B **48**, 11496 (1993).

[120] J. C. Woicik, J. G. Pellegrino, S. H. Southworth, P. S. Shaw, B. A. Karlin, C. E. Bouldin, and K. E. Miyano, Physical Review B **52**, R2281 (1995).

[121] T. L. Lee, Y. Qian, P. F. Lyman, J. C. Woicik, J. G. Pellegrino, and M. J. Bedzyk, Physica B **221**, 437 (1996).

[122] J. C. Woicik, Physical Review B **57**, 6266 (1998).

[123] T. Schmidt, J. Falta, G. Materlik, J. Zeysing, G. Falkenberg, and R. L. Johnson, Applied Physics Letters **74**, 1391 (1999).

[124] J. Falta, T. Schmidt, G. Materlik, J. Zeysing, G. Falkenberg, and R. L. Johnson, Applied Surface Science **162**, 256 (2000).

[125] T. Schmidt, J. Falta, and G. Materlik, Applied Surface Science **166**, 399 (2000).

[126] J. Falta, Gog, T.,Materlik, G., Muller, B.H., Horn-von Hoegen, M., Physical Review B **51**, 7598 (1995).

[127] S. Lagomarsino, F. Scarinci, P. Castrucci, P. Giannini, E. Fontes, and J. R. Patel, Physical Review B **B46**, 13631 (1992).

[128] B. Voigtlander, Zinner, A., Journal of Vacuum Science & Technology a-Vacuum Surfaces and Films **12**, 1932 (1994).

Appendix A X-ray Reflectometer

The X-ray reflectivity experiments in this thesis were performed using the setup shown in Figure A.1. The x-rays are generated from an 18 KW Rigaku rotating anode source with a copper target having a 10-mm by 0.5-mm line source with a 6° take-off angle. The 8.04 keV x-rays, are selected using the newly installed Osmic Model 15NP-002 Max-Flux™ optic x-ray monochromator designed for Cu Kα radiation. The beam is incident from the left side of Figure A.1 and reflects from the multilayer optic to produce a monochromatic beam (which will be discussed in more detail below). The sample resides ~ 180 mm from the incident slit and is mounted onto a Huber two-circle diffractometer. On the two-theta arm there is a guard slit to reduce background, a 1° Soller slit to cut out vertical divergence of scattered x-rays, and a detector slit. The multilayer mirror Bragg diffracts x-rays in a fashion analogous to a single crystal. Alternating layers of high-Z (Ni) and low-Z (C) create a periodic electron density pattern. (Figure A.2). Compared with of a single crystal monochromator, such as Si(111), the d-spacing and angular reflection width are each an order-of-magnitude larger and the bandpass is two orders-of-magnitude larger.

Besides having a relatively large bandpass, the optic is designed to output in the horizontal direction a highly collimated beam with an enlarged horizontal capture angle from the x-ray source. This collimation is achieved by the optic having a parabolic shape with the line source from the x-ray anode at the focal point. X-rays from the source incident upon the mirror surface are reflected along a direction parallel to

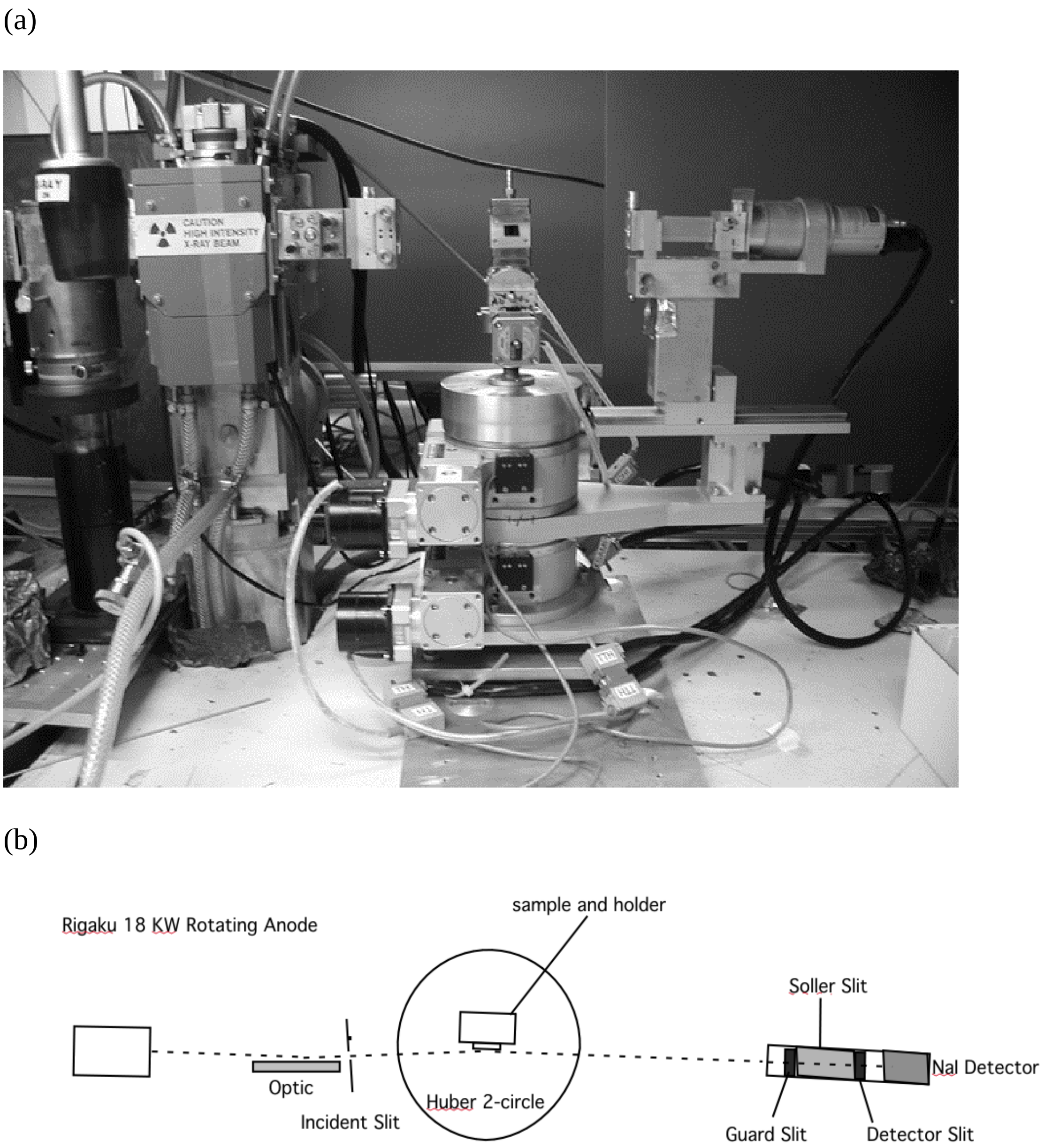

Figure A.1 X-ray reflectivity setup (a) digital image (b) overhead schematic

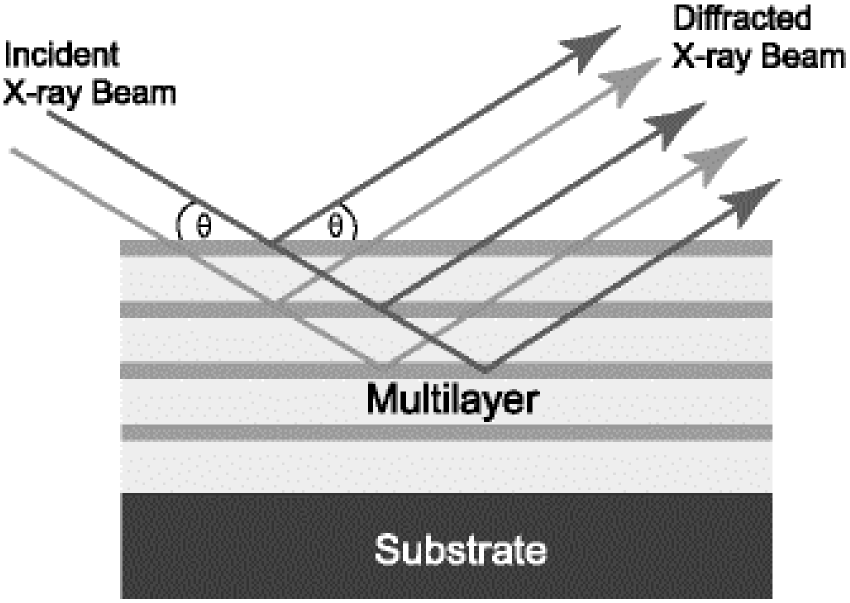

Figure A.2 A side-view depiction illustrating Bragg diffraction from a multilayer.

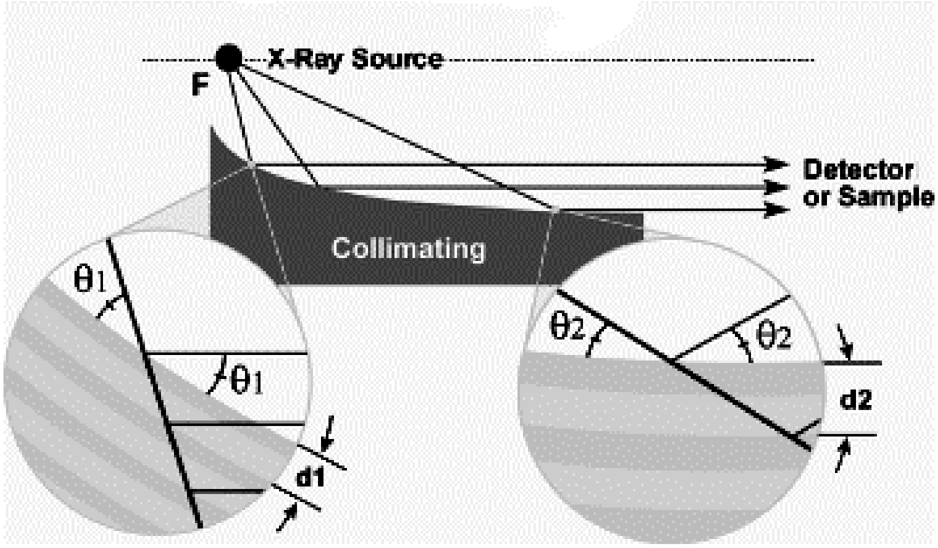

Figure A.3 Demonstration of the collimating principle for the parabolically shaped multilayer optic. Note that $d_2 > d_1$ since $\theta_2 < \theta_1$.

Optic Coating		Ni/C
Wavelength	Å	1.54
Horizontal Source Size	mm	0.04
Length of the Mirror	mm	60
Source to Mirror center distance	mm	106.7
Central d-spacing	Å	33.04
Bragg Angle at center	deg	1.34
Reflectivity (Kα1)	%	0.75
Capture Angle	mrad	13.79
Rocking Curve width (Ave)	mrad	0.49
Divergence of reflected beam	mrad	0.52

Table A.1 Manufacturer specified properties for Osmic Max Flux 0ptic calculated for a 0.04 mm source size. (Our source size is 0.05 mm.)

the axis of the parabola. (see Fig A.3) The d-spacing of the monochromator is graded along the length of the curved mirror surface to compensate for a divergent x-ray source's multiple angles of incidence, thereby satisfying Bragg's law for every point along the optic. The specifications from Osmic for this multilayer mirror are listed in Table A.1

To determine the angle and wavelength resolution of a monochromator, one must consider the relationship between the angle of reflection and wavelength of radiation given by Bragg's law:

$$\lambda = 2d_{hkl}\sin\theta_B \quad . \tag{A.1}$$

By differentiation one can relate properties of the diffracted beam such as the angular divergence of the beam ($\Delta\theta$), and the wavelength spread ($\Delta\lambda$):

$$\Delta\lambda = 2d_{hkl}\cos\theta_B\Delta\theta$$
$$\frac{\Delta\lambda}{\lambda} = \cot\theta_B\Delta\theta \tag{A.2}$$

Figure A.4 is a Dumond diagram illustrating the bandwidth selection determined by the convolution of the multilayer monochromator and our Si(004) analyzer crystal that was used to study the incident x-ray beam from the multilayer. The slopes of the multilayer and the Si(004) analyzer are given by $\cot\theta_B$ (normalized to λ). The cross-hatched regions correspond to the FWHM of the $K\alpha_1$ and $K\alpha_2$ peaks (1.54056 Å and 1.54439 Å) which are separated in wavelength by 0.00383 Å. The Cu $K\alpha$ line width is $\Gamma = 2.0$ eV. Therefore the FWHM of each line is 0.00038 Å. Two angular positions of the Si(004) analyzer are indicated: between the $K\alpha_1$ and $K\alpha_2$ peaks (solid line) and in the middle of $K\alpha_1$ (dashed line).

The optic's design, which is optimized for low-angle reflectivity measurements, sacrifices resolution for intensity and does not separate Cu $K\alpha_1$ and $K\alpha_2$. The settings for the measurement were as follows: Vertical incident beam slit = 10 mm, vertical guard slit = 4 mm, horizontal guard slit = 5.6 mm, horizontal detector slit = 5.5 mm, vertical detector slit = 4 mm. The use of a Soller slit limited the axial divergence to no more than 1^0. In reality the axial divergence was much less (as will be addressed later). The operating power for this measurement was 40 kV and 100 mA. The maximum power settings for this x-ray generator are 50 kV and 240 mA. An Al foil was placed in front of the detector to attenuate the intensity of the beam received by the detector (x-ray transmission = 6.3%).

Figure A.5 shows the $\theta - 2\theta$ data taken at a series of different incident beam horizontal slit settings using a symmetric Si(004) Bragg reflection as an analyzer crystal. The lowest curve is for a horizontal slit setting of 0.1 mm and we increased the gap systematically until it reached 1.9 mm where the entire beam was incident upon the sample. The Si(004) measured angular width of the Cu $K\alpha_1$ peak (FWHM) depends on a number of different factors including the angular width of the Si (004) analyzer crystal ω_{Si}, the divergence due to the dispersion between the multilayer and the Si (004) analyzer (Ω_{dis}), the effective divergence due to the source size (Ω_s), the axial divergence's coupling to the horizontal divergence (Ω_{ax}), and finally the divergence induced by the manufacturer's error in creating a perfectly parabolic mirror (Ω_M). The overall measured divergence ($\Delta\theta$) can be obtained by combining five terms:

$$\Delta\theta = \sqrt{\omega_{Si}^2 + \Omega_{dis}^2 + \Omega_s^2 + \Omega_{ax}^2 + \Omega_M^2}\ . \qquad \text{(A.3)}$$

Assuming a perfect crystal, the first term (ω_{Si}), is the Darwin width of Si(004) at 8.04 keV which is 0.017 mrad. Using $\frac{\Delta\lambda}{\lambda} = \frac{2eV}{8000eV}$ and the Si(004) Bragg angle of

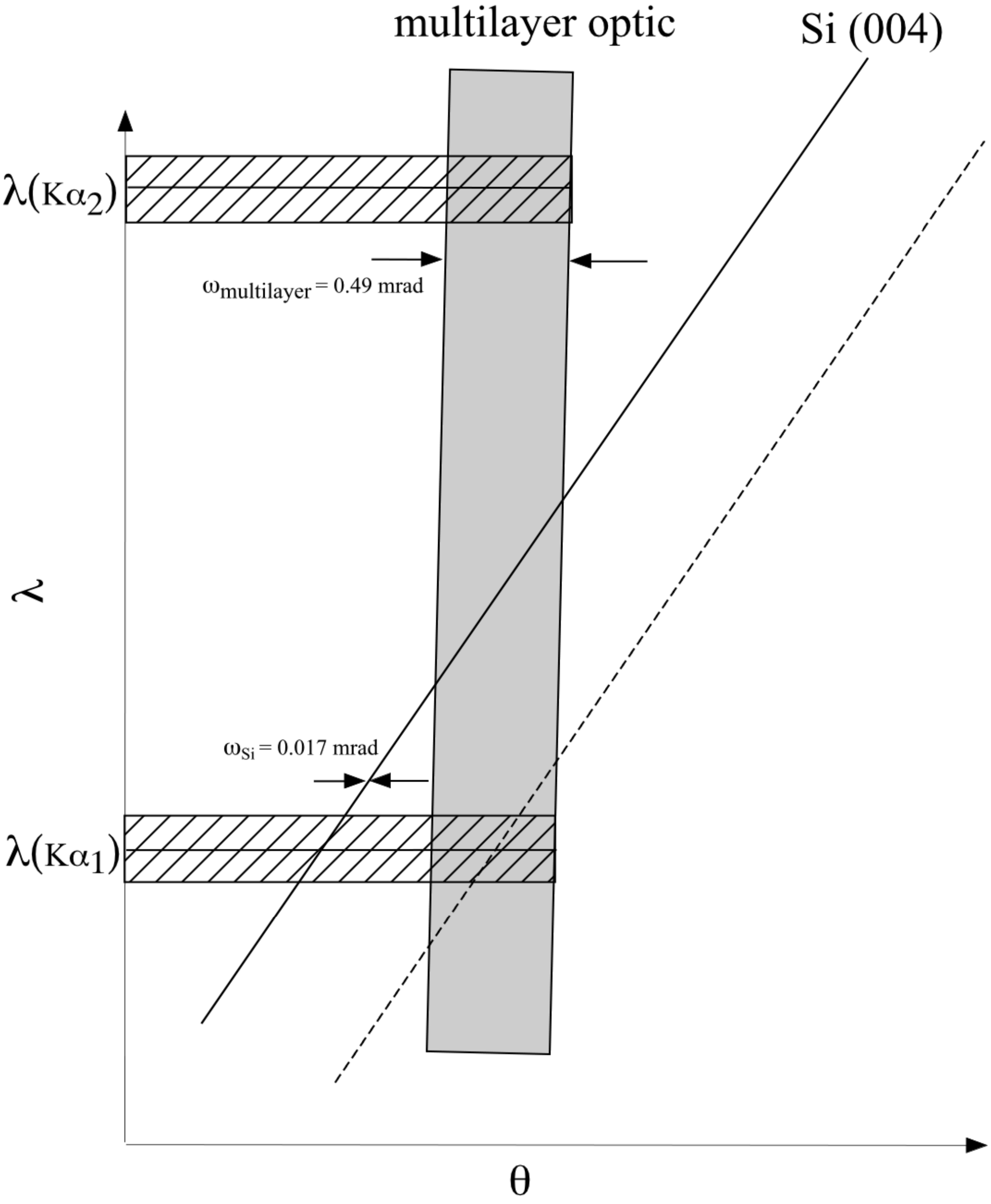

Figure A.4 Dumond diagram for our reflectometer setup. Solid and dashed lines pertain to different positions of the Si (004) crystal passing through the $K\alpha_1$ and $K\alpha_2$ peaks.

34.565° , the second term in equation A.3 is calculated (using equation A.2) Ω_{dis}= 0.17 mrad. The optic was specially designed to accommodate our setup. The acceptance angle of the optic (0.49 mrad) matches very closely to our source divergence. The source divergence is related to the source size (0.05 mm) and the distance from the source to the monochromator (106 mm) and is calculated to be 0.47 mrad. The axial divergence's contribution to the horizontal divergence can be calculated by using the following:

$$\Omega_{ax} = \frac{\phi^2}{8}\cos\theta_B \ , \tag{A.4}$$

where ϕ is the axial divergence. The axial divergence of our setup is defined as the height of the source (10 mm) plus the height of the detector slit (4 mm) all divided by the distance between the two (626 mm). The axial divergence (ϕ) is 22.4 mrad and thus, Ω_{ax} = 0.05 mrad. The manufacturer quoted us a value of 0.007 mrad for Ω_M which is fairly insignificant. Using equation A.3 the total measured divergence of our system ($\Delta\theta$) is calculated to be 0.51 mrad. Note that this is just slightly larger than Ω_S since all the other terms in equation A.3 are insignificant when added in quadrature. Only Ω_{dis} gives a slight broadening. Our measured FWHM of the reflected beam for a slit setting of 1.9 mm (entire beam incident upon sample) is 0.80 mrad, which is higher than our predicted value. If one examines our data in Figure A.5 closely, the peak intensity ratio of $K\alpha_1$ to $K\alpha_2$ is 1.5. Ideally, if the optic was perfectly aligned, this value should be 2. This misalignment has the effect of increasing the divergence of the multilayer optic and likely explains our higher measured divergence. Other parameters such as estimation of source sizes, etc. will also have a small effect. The reduction of the incident beam horizontal slit has the effect of reducing the divergence of the beam incident upon the Si (004) analyzer. This is illustrated by decrease in measured FWHM of the Kα_1 and Kα_2 peaks as the slit size is reduced.

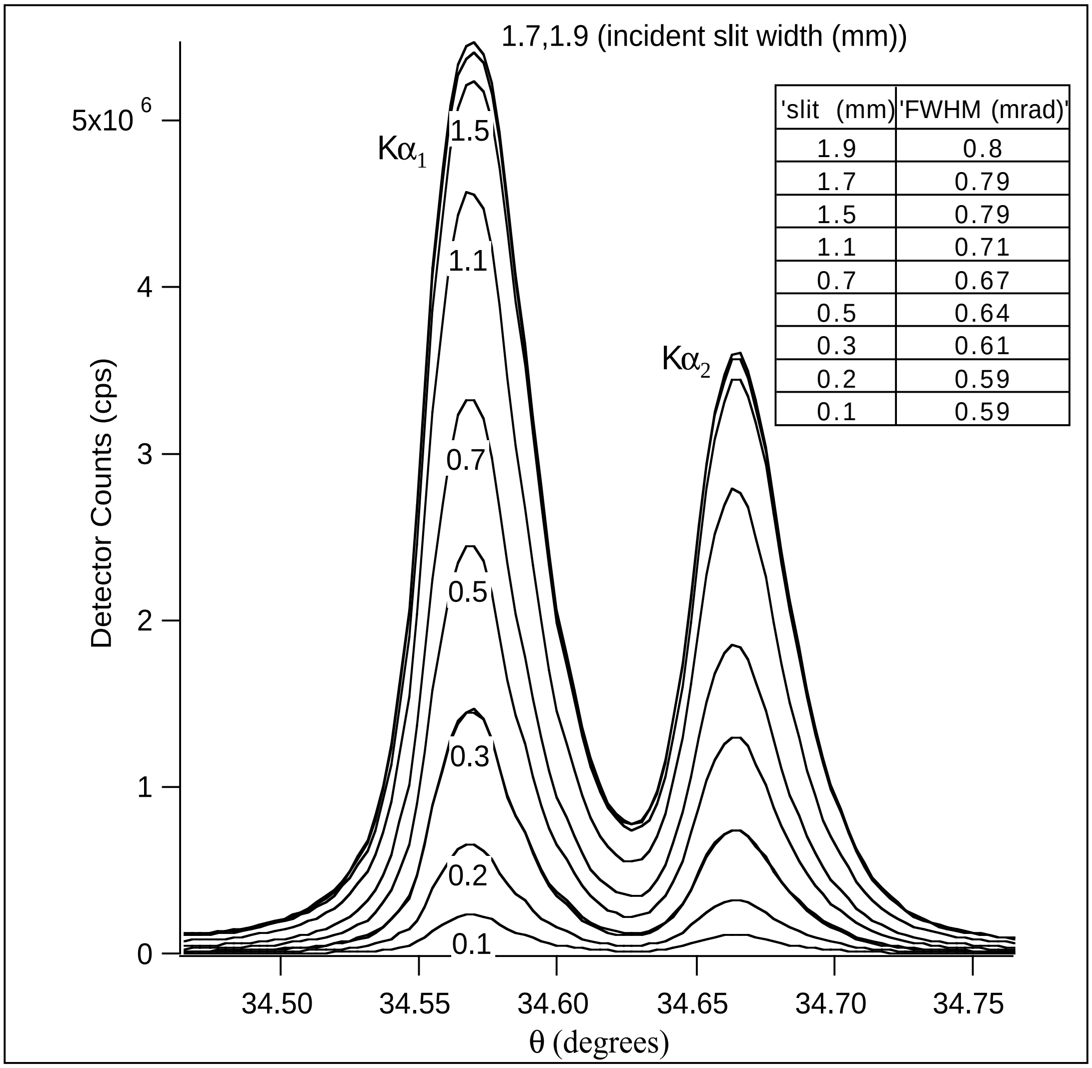

'slit (mm)'	'FWHM (mrad)'
1.9	0.8
1.7	0.79
1.5	0.79
1.1	0.71
0.7	0.67
0.5	0.64
0.3	0.61
0.2	0.59
0.1	0.59

Figure A.5 A series of θ−2θ scans of the Si(004) analyzer crystal . The radiation is emitted from multilayer optic monochromator. The curves are for different horizontal slit gaps for the incident beam. The detector counts have been corrected with transmission factor for the Al attenuator.